The Henryk Niewodniczański
Institute of Nuclear Physics
Polish Academy of Sciences

Ab initio studies of structural, electronic, and dynamical properties of transition metal pyrophosphates

Svitlana Pastukh

A thesis submitted for the degree of
Doctor of Philosophy in Physics

Supervisor: dr. hab. Przemysław Piekarz
Co-Supervisor: dr. Magdalena Laskowska

Cracow, 2023

Dedication and thanks

"As we express our gratitude, we must never forget that the highest appreciation is not to utter words, but to live by them."

- John F. Kennedy

At the beginning of my thesis, I want to express my deep gratitude to the people without whom this long and at the same time very fast, with ups and downs, challenging but exciting, path to the Ph.D. would not have been possible.

First and foremost, I want to thank my husband, dr. Oleksandr Pastukh, for sharing both the good and the bad times with me and for his encouragement and support during those times. I am grateful to my parents, and I also extend my thanks to my siblings. My presence in this place is a result of their support. Their unwavering belief in me and constant encouragement in all aspects of my life are deeply appreciated.

I want to express my sincere gratitude to dr. hab. Przemysław Piekarz, who is my Ph.D. supervisor. This trip has been made possible by his direction, steadfast support, and aid. His unrelenting quest for achievement has inspired me to go beyond boundaries and explore new possibilities. It's important to note that my supervisor has consistently been a source of encouragement who inspires me to realize my best potential. I am incredibly grateful for his openness to listen to me anytime I needed advice. I sincerely appreciate your ongoing support and presence.

My co-supervisor, dr. Magdalena Laskowska, who has not only mentored me but also helped me delve further into the field, has my thanks. Her influence has inspired me to foster my curiosity and to accept challenges in a variety of fields. Her help with material synthesis and support during the experimental part of my research has also been invaluable.

Last, but not least, I would like to thank the following people for their insightful remarks and illuminating conversations: dr. hab. Paweł Jochym, dr. Dominik Legut, dr. Dominika Kuźma, dr. hab. Jan Łażewski, dr. hab. Łukasz Laskowski, dr. Andrii Fedorchuk, dr. Svetoslav Stankov, dr. hab. Mariana Derzsi.

Abstract

This doctoral thesis represents a thorough investigation into the physical properties of transition metal pyrophosphates. For such a purpose, the *ab initio* calculations were applied, which gave the possibility to analyze the intricate interplay of crystal structure, electronic properties, and lattice dynamics in these materials. The main focus of the study was on copper pyrophosphate ($Cu_2P_2O_7$) in its α and β phases and iron pyrophosphate [$Fe_4(P_2O_7)_3$].

For the α phase of copper pyrophosphate, the density functional theory was used for the analysis of the material. A good agreement between calculated lattice parameters and atomic positions with experimental data, which include measurements for copper pyrophosphate nanocrystals synthesized in silica mesopores, was achieved during the study. It was shown that incorporating local Coulomb interactions and van der Waals corrections plays a significant role in such calculations. The antiferromagnetic order of magnetic moments on copper atoms emerged as the lowest energy configuration, mirroring experimental findings. The analysis of phonon dispersion curves and density of states confirmed the dynamical stability of α-$Cu_2P_2O_7$. The investigation of the thermodynamic properties has elucidated pronounced anisotropy in oxygen thermal displacements, providing a theoretical framework for understanding the negative thermal expansion (NTE) observed in the compound. The NTE phenomenon was examined by considering both the quasiharmonic approximation and anharmonic correction, and the theoretical results were compared with experimental values.

The electronic and lattice properties of the β phase of copper pyrophosphate were also analyzed within the *ab initio* calculations, showing good agreement of structural parameters with the experimental data accounting for Coulomb interactions and van der Waals corrections. The detailed study of dynamical properties of the β-$Cu_2P_2O_7$ crystal revealed the existence of the soft mode at the A point of the Brillouin zone and its key role in the structural phase transition. Performed self-consistent phonon calculations based on the temperature-dependent effective potential show the crucial role of anharmonic effects in such a process and their connection to negative thermal expansion.

For iron pyrophosphate, a comprehensive analysis of electronic, structural, and dynamical properties were carried out taking into account three distinct antiferromagnetic configurations. Electronic density of state calculations discerned a significant exchange splitting within the Fe($3d$) states, elucidating magnetic properties. The calculated magnetic moments and the obtained antiferromagnetic order correspond

remarkably well with the experimental observations, validating the performed calculations. The examination of phonon dispersion relations revealed the presence of the soft modes, suggesting the possibility of a structural phase transition at lower temperatures. Unfortunately, this prediction remains unconfirmed due to the absence of detailed experimental analysis of the crystal symmetry at low temperatures.

The performed theoretical studies based on the first-principles methods gave a deep understanding of the physical properties of metal ion pyrophosphates, shedding light on their unique characteristics. Obtained results highlight the complex interplay between their structural, electronic, and phonon properties, opening up the materials' potential applications and paving the way for future investigations.

Streszczenie

Niniejsza praca doktorska przedstawia wszechstronne badania właściwości fizycznych pirofosforanów metali przejściowych. W tym celu zastosowano obliczenia *ab initio*, które umożliwiły analizę złożonych zależności między strukturą krystaliczną, własnościami elektronowymi i dynamiką sieci w tych materiałach. Główny nacisk badań skupił się na pirofosforanie miedzi ($Cu_2P_2O_7$) w fazach α i β oraz na pirofosforanie żelaza [$Fe_4(P_2O_7)_3$].

Dla fazy α pirofosforanu miedzi wykorzystano teorię funkcjonału gęstości do dokładnej analizy własności materiału. W trakcie badań osiągnięto dobrą zgodność między obliczonymi parametrami sieci i pozycjami atomów, a danymi eksperymentalnymi, które obejmują pomiary dla nanokryształów pirofosforanu miedzi otrzymane w mezoporach krzemionki. Wykazano, że w takich obliczeniach istotną rolę odgrywa uwzględnienie lokalnych oddziaływań kulombowskich i poprawek van der Waalsa. Uporządkowanie antyferromagnetyczne atomów miedzi odpowiada konfiguracji o najniższej energii, co bardzo dobrze odzwierciedla wyniki eksperymentalne. Analiza krzywych dyspersji fononów i gęstości stanów fononowych potwierdziła dynamiczną stabilność α-$Cu_2P_2O_7$. Zbadanie właściwości termodynamicznych wykazało silną anizotropię przemieszczeń termicznych atomów tlenu i dostarczyło teoretycznej interpretacji silnej ujemnej rozszerzalności termicznej występującej w tym związku. Zjawisko ujemnej rozszerzalności termicznej zbadano w ramach przybliżenia quasiharmonicznego, jak również uwzględniając poprawki anharmoniczne, a wyniki teoretyczne porównano z wartościami eksperymentalnymi.

Właściwości elektronowe i sieciowe fazy β pirofosforanu miedzi również zostały przeanalizowane w ramach obliczeń *ab initio*, wykazując dobrą zgodność parametrów strukturalnych z danymi eksperymentalnymi przy uwzględnieniu oddziaływań kulombowskich i poprawek van der Waalsa. Szczegółowe zbadanie właściwości dynamicznych kryształu β-$Cu_2P_2O_7$ ujawniło występowanie miękkiego modu w punkcie A strefy Brillouina oraz jego kluczową rolę dla strukturalnego przejścia fazowego. Przeprowadzone obliczenia samouzgodnionych fononów w oparciu o zależny od temperatury potencjał efektywny pokazały kluczową rolę efektów anharmonicznych w takim procesie i ich związek z ujemną rozszerzalnością termiczną.

Dla pirofosforanu żelaza przeprowadzono wszechstronną analizę właściwości elektronowych, strukturalnych i dynamicznych uwzględniając trzy różne konfiguracje oddziaływań antyferromagnetycznych. Obliczenia gęstości stanów elektronowych wykazały znaczące rozszczepienie wymienne w stanach Fe($3d$), co pozwoliło na wyjaśnienie zachowania magnetycznego. Wyliczone momenty magnetyczne i uzyskany

porządek antyferromagnetyczny zgadzają się z wynikami eksperymentalnymi, potwierdzając przeprowadzone obliczenia. Badanie relacji dyspersji fononów ujawniło obecność miękkich modów, co sugeruje możliwość strukturalnego przejścia fazowego w niższych temperaturach. Niestety, przewidywanie to pozostaje niepotwierdzone ze względu na brak szczegółowej analizy eksperymentalnej symetrii kryształu w niskich temperaturach.

Przeprowadzone badania teoretyczne oparte na metodach obliczeniowych z pierwszych zasad dostarczyły głębokiego zrozumienia właściwości fizycznych pirofosforanów na bazie metali przejściowych, rzucając światło na ich unikalne cechy. Uzyskane wyniki podkreślają złożoną zależność między ich własnościami strukturalnymi, elektronowymi i fononowymi, otwierając drzwi do potencjalnych zastosowań tych materiałów i torując drogę dla przyszłych badań.

Contents

List of abbreviations used

AFM	antiferromagnetic
ALM	anharmonic lattice model
APT	anharmonic perturbation theory
CLT	central limit theorem
DFPT	density functional perturbation theory
DFT	density functional theory
DOS	density of states
ECP	effective core potential
FFT	fast Fourier transformation
FM	ferromagnetic
GGA	general gradient approximation
HA	harmonic approximation
HECSS	high efficiency configuration space sampling
HF	Hellmann-Feynman
HGH	Hartwigsen-Goedecker-Hutter
IBZ	irreducible Brillouin zone
IFC	interatomic force constant
KS	Kohn-Sham
LA	longitudinal acoustic
LDA	local density approximation
LO	longitudinal optic
LSDA	local spin density approximation
MD	Molecular Dynamics
MP	Monkhorst-Pack
MSD	mean-square displacements
NMR	nuclear magnetic resonans
NTE	negative thermal expansion
PAW	projector augmented-wave
PBC	periodic boundary conditions
PBE	Perdew-Burke-Ernzerhof
PDOS	phonon density of states
PTE	positive thermal expantion
QHA	quasiharmonic approximation
RPA	random-phase approximation
SCPH	self-consistent phonon
SEM	scanning electron microscopy

TA	transverse acoustic
TDEP	temperature dependent effective potential
TEM	transmission electron microscopy
TO	transverse optic
TS	Tkatchenko-Sheffler
VASP	Vienna Ab initio Simulation Package
vdW	van der Waals

Introduction

Phosphate materials encompass a wide range of compounds that contain the phosphate ion $[PO_4]^{3-}$ as their central component. These materials are renowned for their exceptional properties and versatility, leading to their extensive utilization in various fields including medicine, biology, geology, agriculture, and industry. Phosphate as the simplest form of a phosphorus compound found in nature is an essential element that constitutes the building blocks of all living cells. It plays a pivotal role in numerous biochemical pathways, as well as in the structure and regulation of biological systems [1, 2, 3]. In the realm of genetics, phosphate assumes vital importance as a constituent of the structure and functionality of deoxyribonucleic acid (DNA) and ribonucleic acid (RNA), which are the fundamental types of nucleic acids responsible for storing and expressing genetic information in living organisms. Within both DNA and RNA, phosphate serves as the backbone of the nucleic acid molecule, whose acidic nature is due to the presence of phosphoric acid. The phosphate backbone not only imparts stability to the nucleic acid molecule but also plays a crucial role in the storage, transmission, and expression of genetic information [4]. Moreover, phosphate plays an equally significant role in molecules such as adenosine triphosphate (ATP), which serves as a primary energy source for cells [5]. In ATP, phosphate participates in high-energy bonds between phosphate groups, known as phosphoanhydride bonds. These bonds possess the ability to store substantial amounts of energy.

Phosphate-based compounds exhibit a wide array of physico-chemical properties due to their ability to interact with various elements and substances. These compounds display versatile behavior, acting as both acids and bases depending on the surrounding pH conditions, and their solubility can vary accordingly. Phosphates are abundant on Earth, environmentally benign and possess high stability. Furthermore, phosphates can actively participate in reduction-oxidation reactions, serving as either oxidizing agents or reducing agents, depending on the specific reaction conditions [6]. One noteworthy characteristic of phosphates is their ability to form

coordination bonds and complexes with metal ions. This property enables them to be utilized in a diverse range of applications across multiple industries. By forming stable complexes with metal ions, phosphates can enhance the functionality and performance of various materials. For instance, they can be employed as catalysts in chemical reactions, due to their ability to facilitate and promote specific transformations [7]. Additionally, their complexation with metal ions enables them to act as chelating agents, playing a crucial role in metal extraction and purification processes. Moreover, the unique coordination properties of phosphates make them valuable in the field of medicine and pharmaceuticals [8]. They can be utilized for drug delivery systems, where the phosphate-based compounds serve as carriers or imaging and contrast agents for medical imaging techniques.

A special interest among phosphate materials is held by pyrophosphate complexes. These structures, composed of pyrophosphate ions $[P_2O_7]^{4-}$ as a significant component, exhibit unique properties that distinguish them within the broader class of phosphate materials. Pyrophosphates are multifunctional compounds with a wide range of properties favorable in materials science and chemical applications. Crystalline and amorphous pyrophosphates, containing different di- or trivalent metal ions, exhibit unique physical, chemical, and mechanical properties, which make them valuable in different industries, enabling advancements in technology and material science, healthcare and nutraceutics industry, food processing and environmental sustainability [9]. Due to its versatile coordination modes, aqueous solubility, low toxicity, and biocompatibility one of the key applications of pyrophosphates is the field of nanotechnology.

Pyrophosphates containing transition metals ions offer unique properties that make them well-suited for use in a variety of applications in nanomaterials production. Nanostructures, that have at least one dimension on the nanoscale, can show new distinctive physical and chemical properties compared to their bulk counterparts. In this case, the exceptional characteristics of pyrophosphate materials available at the nanoscale make them ideal candidates for the above applications. The ability to undergo solid-state phase transitions, which change the structure and affect physical properties of material, is another of their most notable characteristics. Pyrophosphates can be used as precursor materials to synthesize a variety of nanomaterials, such as nanotubes, nanoparticles, and nanofibers. Combining the properties of initial components, these materials have a range of potential applications, including catalysts, nanobiomaterials, proton conductors, laser materials, ferroelectrics, sensors, optoelectronic devices, drug delivery systems, and energy storage devices.

The scientific studies that report on the physicochemical properties of transition

metal pyrophosphates and their potential applications do not always provide insight into the origin of materials' unique behavior and physical phenomena, which are interesting from the perspective of fundamental science. Due to the strong Coulomb interactions in transition metal ions that are responsible for the insulating phase, these materials can be classified as Mott insulators. They also show magnetic properties with the antiferromagnetic long-range order observed at low temperatures. Numerous interesting phenomena connected with the crystal lattice, such as the strong negative thermal expansion (NTE) and structural phase transitions, were discovered too. In this context, the investigation of transition metal pyrophosphates using first-principles methods, which are based on fundamental physical principles and quantum mechanics, is important for several reasons. Theoretical methods offer atomistic-level resolution, allowing researchers to investigate the behavior of individual atoms and their interactions within a whole structure. This level of detail is crucial for understanding the underlying mechanisms governing the properties and behavior of materials. Using of *ab initio* methods allows for an accurate and detailed understanding of electronic structure and lattice dynamics, and for revealing their magnetic, optical, or thermodynamic properties. They are also very effective in predicting new properties or phenomena not yet experimentally detected.

Aims of the thesis

The general aim of this research is *to gain a comprehensive understanding of the physical properties of metal ion pyrophosphates through ab initio calculations in order to reveal their unique characteristics favorable for specific applications.* To achieve this aim, the thesis focuses on studying the structural, electronic, and dynamical properties of metal ion pyrophosphates, with specific emphasis on Cu and Fe pyrophosphates. These materials exhibit intriguing properties, making them ideal candidates for investigation.

For copper pyrophosphate, the specific aims include the studies on (1) the effect of local Coulomb interactions on the electronic, magnetic, and structural properties, (2) lattice dynamics and thermodynamic properties, (3) the influence of temperature on the crystal structure and the mechanism responsible for the observed NTE behavior. The calculations were performed for two crystallographic phases of copper pyrophosphate: low-temperature α phase and high-temperature β phase.

In the case of iron pyrophosphate, the specific aims revolve around understanding its electronic and magnetic properties. The thesis explores the impact of electron interactions on the electronic structure, magnetic moments, and exchange interactions

in iron pyrophosphate. The calculations of phonon dispersions were performed in order to investigate the lattice dynamical properties and the stability of the crystal structure.

The central hypothesis formulated in this doctoral dissertation is that *the dynamics of the P_2O_7 group play a crucial role in shaping the thermodynamic characteristics and structural stability of pyrophosphate materials*.

Contents of the thesis

A description of pyrophosphate materials is given in **Chapter 1**, with an emphasis on their characteristics and applications. It discusses the pyrophosphates' general properties as well as their relevance to diverse industries. Additionally, it emphasizes transition metal pyrophosphates and has separate sections on copper pyrophosphate and iron pyrophosphate.

Chapter 2 delves into the theoretical background and computational methods employed in the thesis. It begins by introducing density functional theory (DFT) and its underlying principles, such as the Hohenberg-Kohn theorems and the Kohn-Sham equations. The chapter also covers exchange-correlation energy, electron wave functions, and pseudopotentials. Additionally, it explores the equation of state and analyzes strongly correlated systems studied by the DFT+U method. Lastly, the chapter addresses the treatment of van der Waals interactions using D2, D3, and Tkatchenko-Scheffler methods.

In the following **Chapter 3**, the focus shifts to phonon calculations, which play a crucial role in understanding lattice dynamics. It introduces the general theory of lattice dynamics and discusses the direct method for determining phonon dispersion curves and phonon density of states. The chapter also describes the calculation method of Raman scattering implemented within the direct method and the phonon thermodynamic functions within the harmonic approximation. It further covers the approaches for studying the anharmonic effects: quasiharmonic approximation, temperature-dependent effective potential, anharmonic perturbation theory, self-consistent phonon theory, and high-efficiency configuration space sampling.

Chapters 4 and **5** are dedicated to the investigation of copper and iron pyrophosphate, respectively. They provide details regarding the calculation methods used in the study. **Chapter 4** examines the alpha phase of copper pyrophosphate, including its crystal structure, electronic properties, phonon dispersion relations, Raman scattering, anharmonic properties, and thermodynamic functions. It also presents the investigation of the NTE phenomena observed in α-$Cu_2P_2O_7$. It then proceeds to

explore the beta phase, discussing its crystal structure, electronic properties, lattice dynamics, and the mechanism of structural phase transition. **Chapter 5** focuses on the examination of iron pyrophosphate. It commences by providing an overview of the calculation specifics employed in the research. Subsequently, the chapter delves into an analysis of the crystal structure of iron pyrophosphate, followed by an exploration of its electronic and magnetic properties. Finally, the calculated phonon dispersions are analyzed and the dynamical stability of the iron pyrophosphate structure is discussed.

The main achievements of the thesis are summarized in **Conclusions**.

Computational resources

All calculations presented in this thesis were performed using the computer cluster (15 nodes with 64 cores) belonging to the Department of Computational Materials Science in the Institute of Nuclear Physics and two supercomputers, Barbora (849 TFlop/s) and Karolina (15.7 PFlop/s), at IT4Innovations National Supercomputing Center at VSB Technical University of Ostrava.

Chapter 1

Pyrophosphate materials

The distinctive crystal structure of pyrophosphates, which is made up of phosphorus and oxygen atoms, has garnered considerable interest in science. Advances in many areas of research, especially in chemistry, materials science, and biology, depend on understanding phosphates and their characteristics. These compounds are necessary for many physiological processes and are used as building blocks of several biological components. Moreover, phosphates are a crucial part of fertilizers used in agriculture and play a significant role in numerous applications.

1.1 A general characterization

In chemistry, the tetrahedral structure of phosphate anions $[PO_4]^{3-}$ is of special importance. This atom arrangement produces a highly symmetrical and stable structure, making it a useful building block for many compounds. Phosphate anions are frequently linked to solid silicates because of their comparable tetrahedral shape.

There are various acids that can be attributed to phosphorus(V). Orthophosphates, condensed phosphates, and polyphosphates are the three main categories of phosphate materials. The most basic phosphates are orthophosphates, which are made from H_3PO_4. These acids can be regarded as partially dehydrated products of a hypothetical compound known as $P(OH)_5$. This means that if $P(OH)_5$ were to lose a molecule of water, it would result in the formation of an acid such as H_3PO_4

$$P(OH)_5 \rightarrow H_3PO_4 + H_2O \tag{1.1}$$

Such material, also known as orthophosphoric acid H_3PO_4, has the following molecular structure

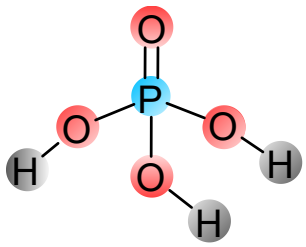

Fig. 1.1. Orthophosphoric acid (H_3PO_4).

Orthophosphate, which is also referred to as monophosphate, has an oxygen to phosphorus ratio of 4:1 and consists of the $[PO_4]^{3-}$ tetrahedron as the anionic unit that is isolated. The reaction (1.1) is an example of how phosphorus(V) forms acids by eliminating water molecules from its hypothetical compound, which further demonstrates the versatility of phosphorus(V) and its ability to form a wide range of compounds. All naturally occurring phosphates are members of the biggest family of phosphates, the monophosphates. Also included in the phosphate family are substituted phosphates, which have had one or more of the oxygen atoms in the PO_4 tetrahedron changed.

The process of eliminating water from H_3PO_4 results in the creation of oxygen bridges between the phosphate groups, which leads to the formation of a class of compounds known as condensed phosphates

$$2H_3PO_4 \rightarrow H_4P_2O_7 + H_2O \tag{1.2}$$

Condensed phosphates, also referred to as pyrophosphates, are a group of phosphates that contain a P-O-P bond within their anionic unit. These compounds are constructed from corner sharing PO_4 tetrahedra.

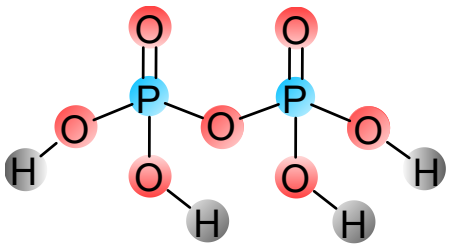

Fig. 1.2. Condensed phosphate ($H_4P_2O_7$).

As the phosphate groups continue to condense, polyphosphoric acids are formed which consist of several phosphate units. Although these acids are not of much use,

some of their salts are widely used in various applications. One of the products resulting from the reaction is triphosphoric acid, also known as tripolyphosphoric acid, with the chemical formula $H_5P_3O_{10}$. This acid can be thought of as a consequence of the further condensation of phosphate groups

$$H_4P_2O_7 + H_3PO_4 \rightarrow H_5P_3O_{10} + H_2O \tag{1.3}$$

Schematic representation of such structure can be shown as follows

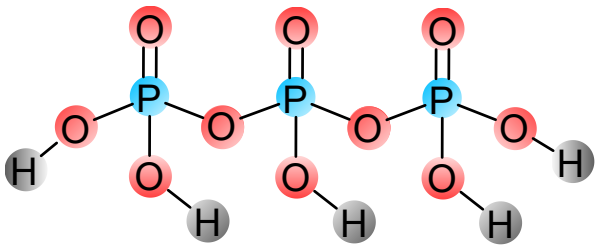

Fig. 1.3. Triphosphoric acid ($H_5P_3O_{10}$).

The strength of an acid refers to its ability to dissociate in water, and as mentioned, the first step of dissociation of the acid is quite extensive. The general formula of the condensed polyphosphoric acids, which are derived from the elimination of water between the $(n-1)$ acid and a molecule of H_3PO_4, is expressed by the formula: $H_{n+2}P_nO_{3n+1}$. This indicates that the acids consist of a chain of phosphoric acid units linked through oxygen atoms, with each chain containing n phosphoric acid units. The elimination of a water molecule from the $(n-1)$ acid and a molecule of H_3PO_4 leads to the formation of a condensed polyphosphoric acid with $n+2$ phosphoric acid units. These condensed polyphosphoric acids are not widely used in their pure form, but are important in the production of various phosphates and phosphonates that have important applications in industries.

Our work is centered around the study of pyrophosphate materials. We are interested in exploring their unique properties and potential applications in various fields, including energy storage, biomaterials, and catalysis. Our research involves the investigation and characterization of pyrophosphate-based materials such as copper pyrophosphate and iron pyrophosphate, with the aim of understanding the structural and dynamical properties of metal ion pyrophosphates.

The geometric configuration assumed by a structural group, such as the $[P_2O_7]^{4-}$ ion, is in part determined by the strengths of the bonds within the ion. If the interatomic distances and/or the angles are varied, the character of the bonds will change.

The actual configuration adopted in a crystalline environment will be a compromise between the maximum stability of the anion and reasonable packing of these anions with the cations to form a translationally symmetric three-dimensional crystal. The bond lengths and angles found for the anion in a given crystal provide a measure of the bond's strengths and character. The strength is generally approximated by the overlap integral of the wave function of the bonding electrons between adjacent atoms forming the bond. Therefore, by imposing small changes in a basic structure —for example by changing the cation or changing the phase— and studying the resultant crystalline geometry, one can gain some understanding of the relative importance of various factors in determining the chemical bonding. Because of the near isomorphism of the various phases and compounds, the transition metal ion phosphates are ideal systems for study in this regard.

The properties and possible uses of these materials are extremely varied. Pyrophosphates are produced using a variety of methods, including hydrothermal synthesis, solid-state reactions, and sol-gel synthesis, and they can have a variety of characteristics, including high-temperature durability, magnetic behavior, and semiconducting qualities.

In **hydrothermal synthesis** [10], the starting materials are heated in a sealed container in the presence of water under high pressure and temperature. This method can result in the formation of high-quality pyrophosphate crystals with a well-defined morphology and size.

Solid-state reactions [11] involve the reaction of two or more solid-state materials to form pyrophosphates. This method is typically carried out at high temperatures and can result in the formation of pure and phase-pure pyrophosphate materials.

Sol-gel synthesis [12] involves the reaction of a metal alkoxide precursor with water to form a sol, which is then dried to form a gel. The gel is then heated to produce the pyrophosphate material. Sol-gel synthesis offers a versatile method for synthesizing pyrophosphate materials with controlled morphology, porosity, and composition.

One of the novel methods is a **synthesis of pyrophosphate nanocrystals inside SBA-15 mesopourous silica** [13, 14, 15] (see an Appendix section). Such an idea is based on the using of silica pores initially functionalized with specific functional groups, which acts as precursor for nanocrystals formation. Then in the process of thermal decomposition of initial material the desired nanocrystals are obtained inside silica pores, which acts as nanoreactors. Such a method allows to obtain nanometric sized pyrophosphate structures, because of spatial confinement created by the silica mesochannels. The above method was applied for the fabrication of copper pyrophosphate nanocrystals, which will be used as the reference material for the comparison

with performed theoretical calculations.

Overall, the specific method used to synthesize pyrophosphates depends on the desired properties and application of the material.

1.2 Properties of pyrophosphate materials and their applications

The properties and behavior of transition metal pyrophosphates have been extensively studied in both academic and industrial settings. Such materials exhibit numerous remarkable physicochemical properties that make them suitable for a diverse range of applications in various fields including chemistry, biology, and industry. In general, pyrophosphate complexes possess significant chemical stability due to the robust nature of the pyrophosphate ions $[P_2O_7]^{4-}$ and high thermal stability, as a result of the energetically stable pyrophosphate anion at high temperatures. Metal pyrophosphates have great electrochemical properties, including high electron transfer rates and capacitance, and can easily form diverse complexes with metal ions through coordination chemistry, enriching their intrinsic characteristics. Some of the characteristic features of transition metal pyrophosphates are shown in Fig. 1.4.

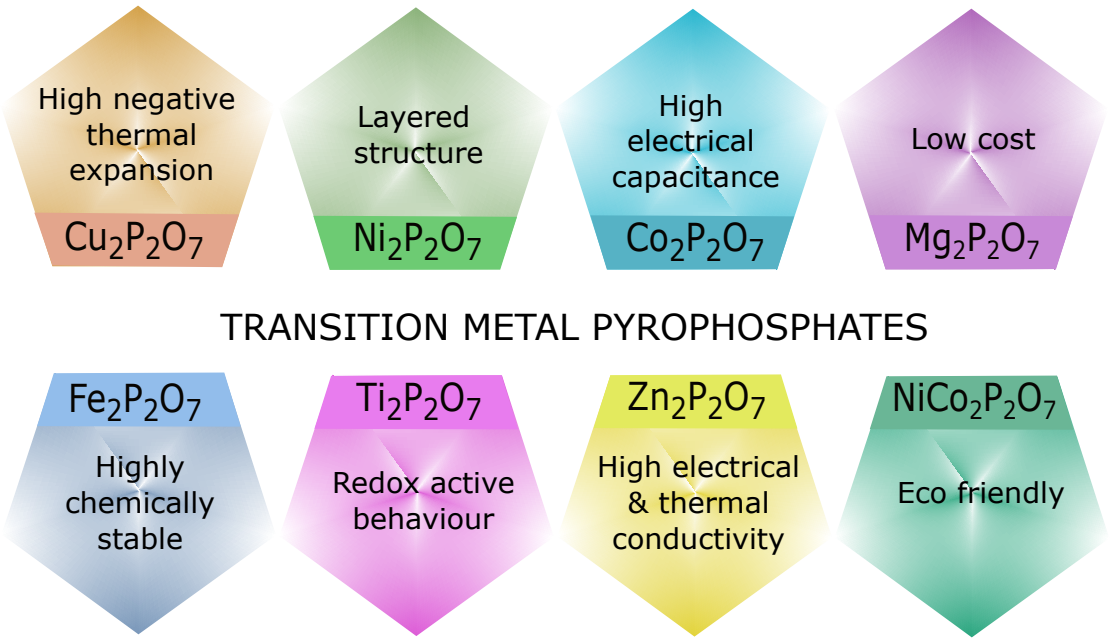

Fig. 1.4. Schematic representation for various properties of transition metal pyrophosphates.

Recent advancements in nanocrystalline materials manufacturing and processing

enable the production of nanoscale materials. The properties of these materials are entirely different from their conventional polycrystalline counterparts, due to their unique structure. Also, the structure property relationship of nanocrystalline materials differs considerably from those observed for thin-film materials. The differences are mainly attributed to microstructural characters including crystallographic texture, porosity, impurities, grain boundary, and triple junctions. Nanocrystalline phosphates are promising materials due to their unique physical, chemical, and mechanical characteristics with a wide range of applications.

The recent overview on the optical properties of rare earth and transition metal doped pyrophosphates [$M_2P_2O_7$ (M = Ca, Sr, Ba, Zn, Mg)] highlights their perspectives in the field of artificial lighting technology [16]. Possessing high flexibility, large band gap, chemical and thermal stability, such structures exhibit good luminescent properties and are potential candidates for applications in solid-state lighting, white light-emitting diodes, fluorescent displays, and others. There are also investigations showing pronounced nonlinear optical response of pyrophosphate complexes. Latest reports show synthesis of nickel pyrophosphate nanocrystals using thermal treatment of nickel phosponate groups in spatially confined environment [15]. Due to the high degree of charge transfer typical for the localized Ni(3*d*) states in $Ni_2P_2O_7$ the resulted compound shows significant nonlinear optical activity (strong second- and third-harmonic generation) and could be a perspective candidate for using in nanophotonics or optoelectronics.

The closely packed P_2O_7 units of pyrophosphate give rise to many proton bonding sites and transport pathways [17]. This feature resulted in the high proton conductivity of some metal pyrophosphates (e.g., Sn, Ti, Ge) at intermediate temperatures, which can be applied to the proton-conducting electrolyte materials for next-generation energy sources. For example, In^{3+}-doped SnP_2O_7 and Y-doped zirconium pyrophosphate were considered as an alternation to the conventional fuel cells due to their chemical stability and possibility to operate at the intermediate temperatures of 200-400 °C [18].

Because of their significant redox-active functionality, great electrical conductivity, low cost, and layered structure, metal pyrophosphates are also considered as a promising electrode for supercapacitors [19]. Such complexes as CoP_2O_7, MnP_2O_7, or TiP_2O_7 acting as a positive electrode in combination with the suitable capacitive electrode can open the route for next-generation energy storage devices [20, 21]. There is also wide use of hybrid supercapacitors in which pyrophosphates are used as positive electrode and carbon-based structures as negative electrode. For example, the use of amorphous nickel pyrophosphate microstructures and graphene nanosheets as

positive and negative electrodes was shown to have a great performance as the energy storage unit for roll-up display panels, power-on-chip systems, or solar energy-driven electronics [22].

In recent years, much attention has been paid to mixed transition metal pyrophosphates, from which special interest is gained by alkali metal pyrophosphates [23]. First studies in this field reported the use of $Li_2FeP_2O_7$ or $Li_2MnP_2O_7$ as the new cathode materials for the next generation of rechargeable lithium-ion batteries due to formation of two-dimensional channel providing efficient Li-diffusion and possibility of two-electron redox reaction [24, 25]. There is also possibility of applying both Fe and Mn for the formation of new lithium mixed transition-metal pyrophosphates with high discharge capacity [26].

Numerous studies also report application of metal pyrophosphate in other fields. For example, vanadium pyrophosphate as the material with high catalytic activity [27], calcium pyrophosphate as perspective nano-bio material, with high biocompatibility and ability to undergo varying degrees of resorbability [28, 29], manganese(III) pyrophosphate complexes acting as a terminal electron acceptor in microbiological systems [30], cobalt and copper pyrophosphate materials having great bio-medical applicative potential [31] and many others.

Due to their fascinating properties and possible applications, pyrophosphate materials research is a busy and engrossing area of study in the field of materials science. As researchers continue to investigate the properties and behaviors of pyrophosphate materials, new opportunities for their use in various fields may emerge. In this work, we concentrate our attention on copper and iron pyrophosphate materials, due to their unique characteristics and wide applications, which are described further.

1.2.1 Copper pyrophosphate

Numerous studies have been conducted to explore the synthesis and experimental properties of copper pyrophosphate complexes [32, 33]. These materials have shown great promise in terms of their electrical [34], chemical [35], and thermal [36] characteristics. They are emerging as potential electrode materials for advanced energy storage devices such as supercapacitors [37]. Ultrathin $Cu_2P_2O_7$ nanoflakes placed on the stainless steel substrate show an excellent specific capacitance [38], while the copper pyrophosphate microflowers grown on multi-walled carbon nanotubes exhibit an exceptionally enhanced electrochemical performance and robust cycle life [39]. Due to unprecedented redox activity, they are also very good catalysts as shown in the studies on fructose dehydration [40], selective CO_2 electroreduction to multicarbon products [41], and partial oxidation of methane into formaldehyde [42]. In addition,

the investigation of the magnetic properties of binuclear Cu(II) pyrophosphate has revealed a diverse electron paramagnetic resonance spectrum, resulting from the intricate interplay among exchange couplings, magnetic dimensions, and spin dynamics within the compound [43].

The crystal structure of $Cu_2P_2O_7$ at room temperature is characterized by a monoclinic $C2/c$ symmetry, with four molecules present within the unit cell (referred to as the α phase) [44]. However, when the temperature reaches 363 K, a phase transition occurs, leading to the formation of the β phase. In this phase, the crystal structure adopts a monoclinic $C2/m$ configuration, with the lattice parameter c and unit cell volume approximately halved compared to the α phase [45]. Notably, the β phase exhibits a disordered arrangement of oxygen atoms that are shared by the two PO_4 tetrahedra in the pyrophosphate group shown in Fig. 1.5 [46]. Moreover, additional investigations utilizing the diffuse scattering measurements have unveiled the presence of an intermediate phase within the temperature range of 347-363 K [46]. This intermediate phase serves as a transition region between the α and β phases, therefore, the α–β structural transformation was classified as the second-order phase transition of an inhomogeneous type [44].

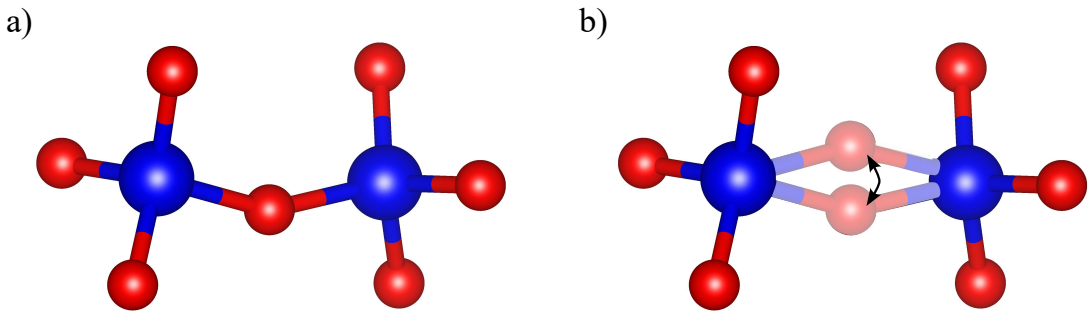

Fig. 1.5. Schematic representation of P_2O_7 group of copper pyrophosphate in the a) α-phase and b) β-phase (by arrow the disordered oxygen is shown), where phosphorous atoms are represented by blue balls and oxygen atoms by red balls.

Furthermore, the neutron diffraction and nuclear magnetic resonance (NMR) studies revealed the emergence of antiferromagnetic (AFM) order below the Néel temperature $T_N = 27$ K [47, 48]. Deviations from the Curie-Weiss behavior were observed below 180 K, indicating the presence of AFM correlations, which ultimately lead to long-range order below T_N. The magnetic interactions were investigated within the two-dimensional model describing strongly coupled magnetic dimers on the basis of the density functional theory calculations [49]. This study demonstrated that the

electronic band structure, as determined by the local density approximation (LDA), displayed an inaccurate metallic state, underscoring the significance of strong electron interactions within the Cu($3d$) states. As shown in this thesis, these electron correlations lead to the Mott insulating state in the copper pyrophosphate [50].

Recent X-ray and neutron diffraction investigations on α-$Cu_2P_2O_7$ have unveiled a fascinating phenomenon of the negative thermal expansion [51]. This particular compound exhibits the most pronounced NTE among all known oxides. The diffraction studies revealed that the lattice parameters a and c decrease with increasing temperature up to the α-β phase transition. It results in the reduction of volume by $\sim$ 1% at 400 K comparing to its value at the lowest temperatures. The NTE phenomenon in α-$Cu_2P_2O_7$ is attributed to the transverse vibrations of oxygen atoms, shedding light on the pivotal role played by atomic dynamics in its unique thermal properties.

While experimental studies have explored the Raman spectra of both the α and β phases of $Cu_2P_2O_7$ [46], a comprehensive understanding of the compound's lattice dynamics has yet to be obtained and investigated thoroughly. The investigations aimed at unraveling the full phonon dispersion relations in copper pyrophosphate would contribute valuable insights into its vibrational and thermal characteristics.

1.2.2 Iron pyrophosphate

Iron pyrophosphate is a compound that exhibits intriguing characteristics and properties. It has garnered significant attention in various research areas, including synthesis, structural characterization, and catalysis. Iron pyrophosphate possesses several notable properties that make it a valuable material with diverse applications. Here, we discuss some of its key properties and highlight its potential applications. Iron pyrophosphate exhibits excellent chemical stability, enabling it to withstand harsh environmental conditions, including high temperatures and corrosive environments [52]. This property makes it suitable for applications where chemical resistance is required. Iron pyrophosphate has shown promising catalytic activity in different reactions, including the activation of peroxymonosulfate (PMS) for water purification applications [53]. Its unique P-O-Fe structure serves as an active site for PMS activation, enabling efficient degradation of organic pollutants. This catalytic property opens up possibilities for using iron pyrophosphate in environmental remediation and wastewater treatment.

The biomedical applications of iron pyrophosphate compounds have been extensively investigated. Several studies have highlighted the significance of ferric pyrophosphate in the treatment of iron deficiency and the regulation of iron transport

within the human body [54, 55, 56]. Moreover, the potential applications of iron pyrophosphate in electrochemical energy storage devices, particularly lithium-ion batteries, have garnered significant attention. Porous nanostructures of iron pyrophosphate have demonstrated enhanced electrocatalytic activity in Li-O_2 batteries [57], and lithium iron pyrophosphate compounds synthesized via conventional solid-state reactions have shown promise as cathodes in large-scale lithium-ion battery systems [24].

There are a few known crystallographic forms of iron pyrophosphate: $Fe_2P_2O_7$ [58, 59], $Fe_3(P_2O_7)_2$ [59], $Fe_4(P_2O_7)_3$ [60, 61, 59], and $Fe_7(P_2O_7)_4$ [59]. The study by Xiao *et al.* [58] successfully produced pure off-white $Fe_2P_2O_7$ using a cost-effective solid-phase reaction method. By combining Fe_2O_3 and $NH_4H_2PO_4$ under an argon atmosphere, they were able to reduce Fe^{3+} to Fe^{2+} and obtain well-crystallized $Fe_2P_2O_7$ at temperatures above 630 °C. The resulting $Fe_2P_2O_7$ possessed a triclinic crystal structure belonging to the β phase, with a narrow size distribution ranging from 0.5 to 2 mm.

Here, we focus on the compound $Fe_4(P_2O_7)_3$, which crystallizes in the monoclinic structure with the space group $P2_1/n$. This material exhibits interesting magnetic properties with the AFM long-range order observed below $T_N = 50$ K [60]. Elbouaanani *et al.* [61] conducted a comprehensive investigation of the crystal structure and magnetic properties using neutron diffraction and Mössbauer techniques. Through neutron scattering, they determined the precise arrangement of atoms within the crystal lattice, providing valuable information about bond lengths, angles, and overall geometry. They revealed four AFM iron sublattices corresponding to the four distinct iron atom positions. The magnetic moments are parallel to the *c* axis and are equal to 4.55 μ_B at 1.7 K.

Overall, research on iron pyrophosphate spans various aspects, including synthesis, structural and magnetic characterization, as well as catalytic applications. However, the *ab initio* studies have not been performed yet and the information about the electronic band structure as well as the role of local Coulomb interactions is missing. Also, besides the Raman spectra measured for different types of iron pyrophosphates [59], the lattice dynamical properties of these compounds have not been studied.

Chapter 2

Ab initio methods

Calculation of electronic stationary states in the electrostatic field of atomic nuclei is the goal of the majority of *ab initio* (or first-principles) techniques based on fundamental quantum theory. A few years after the Schrödinger equation's development, in the late 1920s, the first attempts to create suitable theories were made. However, it took approximately 50 years until sufficiently effective methods for solving this equation for the solids-related many-body problems were developed. In order to incorporate correlation effects without employing the extremely expensive wave function approaches, the density functional theory (DFT) was developed. Today, the DFT is the foundation for the majority of *ab initio* techniques utilized in solid state physics and materials research. The fundamental benefit of first-principles approach is its independence from experimental data. There is no requirement for calibration or fitting parameters, unlike in semi-empirical methods. *Ab initio* approaches can therefore be used to calculate some physical properties of hypothetical systems, or to forecast the features of yet-to-be-created materials.

Interactions in atomic systems

The electromagnetic interactions that take place in nature are the ones that have the biggest impact on the physical and chemical characteristics of atomic systems. Interatomic bonds, which are responsible for the formation of molecules and solids, are the consequence of electrostatic interactions between atomic nuclei and electrons. The Hamiltonian that describes any arrangement of atoms has the form

$$H = -\frac{\hbar^2}{2m}\sum_i \nabla_i^2 - \sum_{i,j}\frac{Z_j e^2}{|\boldsymbol{r}_i - \boldsymbol{R}_j|} + \frac{1}{2}\sum_{i\neq j}\frac{e^2}{|\boldsymbol{r}_i - \boldsymbol{r}_j|} - \sum_j \frac{\hbar^2}{2M_j}\nabla_j^2 - \frac{1}{2}\sum_{i\neq j}\frac{Z_i Z_j e^2}{|\boldsymbol{R}_i - \boldsymbol{R}_j|}, \quad (2.1)$$

where $\boldsymbol{r}_i$ are the positions of electrons, $\boldsymbol{R_j}$ the positions of atomic nuclei, Z_j the charges of nuclei, M_j the masses of nuclei, and m is the mass of the electron. The

first three terms, correspondingly, describe the kinetic energy of electrons, electron-nucleus interactions, and electron-electron interactions. The last two terms are the kinetic energy of atomic nuclei and the interaction between nuclear charges. The full wave function of any system of electrons and atomic nuclei $\Psi(\boldsymbol{r}_i, \boldsymbol{R}_j)$ satisfies the Schrödinger equation

$$H\Psi(\boldsymbol{r}_i, \boldsymbol{R}_j) = E\Psi(\boldsymbol{r}_i, \boldsymbol{R}_j), \tag{2.2}$$

where E is the total energy of the system.

Adiabatic approximation

The adiabatic approximation, also known as Born-Oppenheimer approximation [62], is a method for describing molecular electronic structure that assumes that nuclei move much slower than electrons. The approximation separates the electronic and nuclear degrees of freedom and approximates the electronic wave function as if the nuclei were fixed at a specific geometry. In this instance, the wave function of the whole system can be expressed as a product of the electronic function $\Phi(\boldsymbol{r_i}, \boldsymbol{R_j})$ and the function of nuclei $\chi(\boldsymbol{R}_j)$

$$\Psi(\boldsymbol{r}_i, \boldsymbol{R}_j) = \Phi(\boldsymbol{r}_i, \boldsymbol{R}_j)\chi(\boldsymbol{R}_j). \tag{2.3}$$

In the adiabatic approximation, the total Hamiltonian of a molecule can be separated into two parts: the electronic Hamiltonian and the nuclear Hamiltonian. The Schrödinger equation with the electronic part is given by

$$\left(-\frac{\hbar^2}{2m}\sum_{i=1}^{N}\nabla_i^2 - \sum_{i,j}\frac{Z_j e^2}{|\boldsymbol{r}_i - \boldsymbol{R}_j|} + \frac{1}{2}\sum_{i\neq j}\frac{e^2}{|\boldsymbol{r}_i - \boldsymbol{r}_j|}\right)\Phi(\boldsymbol{r}_i, \boldsymbol{R}_j) = E_n(\boldsymbol{R}_j)\Phi(\boldsymbol{r}_i, \boldsymbol{R}_j), \tag{2.4}$$

where $E_n(\boldsymbol{R}_j)$ are the eigenenergies of an electronic system with fixed locations of atomic nuclei.

The nuclear part is given by

$$\left[-\sum_j \frac{\hbar^2}{2M_j}\nabla_j^2 - \sum_{i,j}\frac{Z_i Z_j e^2}{|\boldsymbol{R}_i - \boldsymbol{R}_j|} + E_n(\boldsymbol{R}_j)\right]\chi_{n\alpha}(\boldsymbol{R}_j) = \varepsilon_{n\alpha}\chi_{n\alpha}(\boldsymbol{R}_j), \tag{2.5}$$

where $\varepsilon_{n\alpha}$ are eigenenergies associated with the motion of atomic nuclei. The interaction between the atomic nuclei and the electron subsystem determines the potential energy in the equation describing the motion of nuclei. The Born-Oppenheimer approximation allows solving the electronic Schrödinger equation (2.4) independently of the motion of the nuclei.

2.1 Density functional theory

2.1.1 Hohenberg-Kohn theorems

Density functional theory (DFT), which was developed by Hohenberg and Kohn [63] and Kohn and Sham [64], is the foundation for the majority of contemporary computer approaches used to explore the characteristics of materials. The electronic structure, crystal structure optimization, elastic characteristics, lattice dynamics, and many other material properties are all now calculated using DFT. For systems with hundreds or even thousands of atoms, it is essentially the only approach that enables quantum-mechanical computations.

Two basic theorems in Hohenberg and Kohn's work [63] provide the connection between the electron density $n(\boldsymbol{r})$, the external potential $V_{ext}(\boldsymbol{r})$, and the total energy $E[n]$, which is the electron density functional. The functional connection implies that the total energy of the system $E[n]$ may be uniquely calculated for every distribution of electrons in the full space $n(\boldsymbol{r})$. Using the adiabatic approximation, we can write the generic form of the electron system's Hamiltonian

$$H = -\frac{\hbar^2}{2m}\sum_i \nabla_i^2 + V_{\text{ext}}(\boldsymbol{r}) + \frac{1}{2}\sum_{i\neq j}\frac{e^2}{|\boldsymbol{r}_i - \boldsymbol{r}_j|}. \tag{2.6}$$

The following is a formulation for the Hohenberg-Kohn theorems:

Theorem I: The electron density in the ground state $n_0(\boldsymbol{r})$ unequivocally determines (accurately to a constant value) the external potential $V_{\text{ext}}(\boldsymbol{r})$ of the system of interacting electrons.

Theorem II: The energy functional $E[n]$ reaches the minimal value E_0 for a ground state electron density $n_0(\boldsymbol{r})$ with a given external potential $V_{\text{ext}}(\boldsymbol{r})$.

These theorems lead to the following conclusions. The wave functions of all electronic states as well as all other aspects of the system are entirely governed by the electron density in the ground state, since the Hamiltonian is uniquely defined (up to a constant) by $n_0(\boldsymbol{r})$. To ascertain the energy and electron density of the ground state, one just has to be aware of the energy functional $E[n]$.

2.1.2 Kohn-Sham equations

The Hohenberg-Kohn theorems allow for a determining the relation between the electron density in the ground state and the Schrödinger equation for the system of interacting electrons described by Hamiltonian (2.6). In practice, solving the

Schrödinger equation and determining the multi-body wave functions is not achievable.

The Hohenberg-Kohn theorems guarantee that the electron density uniquely determines the effective potential V_{eff} and that the total energy functional achieves a minimum for a ground state electron density. Thus, if we know the energy functional and can identify its minimum, we may determine the system's ground state. This functional may be written in general as

$$E[n] = T[n] + E_{\text{ext}}[n] + E_{\text{H}}[n] + E_{\text{xc}}[n], \tag{2.7}$$

where $T[n]$ is the kinetic energy of non-interacting electrons, $E_{\text{ext}}[n]$ is the interaction energy with the external potential, $E_{\text{H}}[n]$ is the Hartree energy, and $E_{\text{xc}}[n]$ includes all other interactions, i.e. exchange interaction and electron correlations, as well as the difference between the kinetic energy of a system of interacting and non-interacting electrons. This is known as the exchange-correlation functional.

Using the II Hohenberg-Kohn theorem, which states that $E[n] = \min$, we can derive Kohn-Sham (KS) equations as

$$\left[-\frac{\hbar^2\nabla_i^2}{2m} + V_{\text{KS}}(\boldsymbol{r})\right]\psi_i^\sigma(\boldsymbol{r}) = \varepsilon_{i\sigma}\psi_i^\sigma(\boldsymbol{r}), \tag{2.8}$$

which have the form of a single-particle Schrödinger equation with an effective KS potential

$$V_{\text{KS}}(\boldsymbol{r}) = V_{\text{ext}}(\boldsymbol{r}) + V_{\text{H}}(\boldsymbol{r}) + V_{\text{xc}}(\boldsymbol{r}) = V_{ext}(\boldsymbol{r}) + \int d\boldsymbol{r'}\frac{n(\boldsymbol{r'})}{|\boldsymbol{r}-\boldsymbol{r'}|} + \frac{\delta E_{xc}[n]}{\delta n}. \tag{2.9}$$

The KS potential is composed of three distinct terms:

- $V_{\text{ext}}(\boldsymbol{r})$ is the external potential, which represents the interactions between the electrons and any external fields or potentials present in the system, such as those arising from the nuclei of the atoms in the system.

- $V_{\text{H}}(\boldsymbol{r})$ is the Hartree potential, which arises from the Coulomb repulsion between electrons and describes the direct density-density type interaction.

- $V_{\text{xc}}(\boldsymbol{r})$ is the exchange-correlation potential. This potential is a non-local function of the electron density and is difficult to calculate exactly, therefore, it is typically approximated using various methods and models.

We can determine the electron density at each point by knowing the one-electron solutions of the KS equation $\psi_i^\sigma(\boldsymbol{r})$, which depend on position and spin

$$n(\boldsymbol{r}) = \sum_{i,\sigma} f_{i\sigma}|\psi_i^\sigma(\boldsymbol{r})|^2, \tag{2.10}$$

where, for simplicity, the index i defines both the state number and the wave vector $\boldsymbol{k}$, and $f_{i\sigma}$ are the numbers of state occupations, which can take fractional values in general, e.g. according to the Fermi-Dirac distribution. Here, we assume that the elementary charge $e = 1$, which indicates that the charge density and electron density are the same.

The iterative solution of the KS equations involves a self-consistent method that allows for the minimization of the total energy functional while considering the positions of atoms and lattice parameters. To begin with, the initial positions of atoms are established, which can be determined based on diffraction experiment data. The potential is determined using equation (2.9) with the atomic positions fixed. An initial electron density distribution $n_0(\boldsymbol{r})$ is assumed, and the KS equations are solved for this potential. The one-electron wave functions are then found, which provide the electron density through Eq. (2.10). This process is continued until the ground state energy and electron density converge within a given accuracy.

2.1.3 Exchange-correlation energy

Local density approximation

The exchange-correlation functional E_{xc} and the accompanying potential V_{xc} are not known exactly, and must be evaluated in an approximate manner within the framework of DFT. The local density approximation (LDA) is the most basic approach. In LDA, we assume that the exchange-correlation energy at any point in space, where the electron density is $n(\boldsymbol{r})$, is equal to the exchange-correlation energy of a homogeneous electron gas of the same density, $n = n(\boldsymbol{r})$. The exchange-correlation functional is therefore written as follows

$$E_{\mathrm{xc}}[n] = \int d\boldsymbol{r} n(\boldsymbol{r}) \varepsilon_{\mathrm{xc}}(n), \tag{2.11}$$

where $\varepsilon_{\mathrm{xc}}(n)$ is the exchange-correlation energy per electron in a homogeneous electron gas of density n. It can be written as the sum of the exchange and correlation parts, $\varepsilon_{xc}(n) = \varepsilon_x(n) + \varepsilon_c(n)$. In the slowly fluctuating density limit, the LDA approximation is accurate, which corresponds to the following condition

$$\frac{q}{k_F} \ll 1, \tag{2.12}$$

where q is a measure of system inhomogeneity

$$q = \frac{|\nabla k_F|}{2k_F}, \tag{2.13}$$

and k_{F} corresponds to the Fermi wave vector for a homogeneous gas, which at the point of local density $n(\boldsymbol{r})$ is given by

$$k_{\mathrm{F}} = \left[3\pi^2 n(\boldsymbol{r})\right]^{1/3}. \tag{2.14}$$

This approximation is easily extended to systems with spin polarization. In this case, the total exchange-correlation energy is the functional of densities of spins pointing up $n_\uparrow$ and down $n_\downarrow$

$$E_{\mathrm{xc}}[n_\uparrow, n_\downarrow] = \int d\boldsymbol{r} n(\boldsymbol{r}) \varepsilon_{\mathrm{xc}}(n_\uparrow, n_\downarrow). \tag{2.15}$$

In LDA, the exchange energy is calculated directly using the analytical dependence on the Fermi wave vector or electron density

$$\varepsilon_{\mathrm{x}} = -\frac{3k_{\mathrm{F}}}{4\pi} = -\frac{3}{4}\left[\frac{3}{\pi} n(\boldsymbol{r})\right]^{1/3}. \tag{2.16}$$

The correlation part is obtained numerically within the quantum Monte Carlo approach [65], using the proper parameterization of the correlation energy's dependency on the electron density [66, 67].

Generalized gradient approximation

In the work in 1965, Kohn and Sham suggested taking into consideration local variations in density by extending the exchange-correlation energy into a series of density gradients [64]. The majority of atomic systems, whose variations in electron density are often quite big, cannot be treated using this method because it violates the sum rules. A novel method known as generalized gradient approximation (GGA) was proposed, where the exchange-correlation energy is a functional of the electron density and its gradients [68, 69, 70]. In a general case for a spin-polarized system, it can be written in the form

$$E_{\mathrm{xc}}[n_\uparrow, n_\downarrow] = \int d\boldsymbol{r} f(n_\uparrow, n_\downarrow, \nabla n_\uparrow, \nabla n_\downarrow). \tag{2.17}$$

The exchange part of this functional for a system without spin polarization can be written as

$$E_{\mathrm{x}}[n] = \int d\boldsymbol{r} n \varepsilon_{\mathrm{x}}(n) F_{\mathrm{x}}(s), \tag{2.18}$$

where $s = |\nabla n|/2k_F n$ is the scaled (dimensionless) electron density gradient. An extension to systems with spin polarization is obtained using the following formula, which holds for the exchange energy

$$E_{\mathrm{x}}[n_\uparrow, n_\downarrow] = \frac{1}{2}\left(E_{\mathrm{x}}[2n_\uparrow] + E_{\mathrm{x}}[2n_\downarrow]\right). \tag{2.19}$$

The $F_x(s)$ function has been proposed in several forms, the most popular of which are detailed in: A. D. Becke (Becke88) [70], J. P. Perdew and Y. Wang (PW91) [71] and J. P. Perdew, K. Burke, and M. Ernzerhof (PBE) [72].

The GGA functional is roughly similar to LDA in the case of small gradients or for a homogenous electron gas. This implies that it should always produce better results than LDA for inhomogeneous systems. However, this is not the case, because for some systems, LDA offers a better partial reduction of exchange and correlation errors than GGA does. LDA usually gives overestimated cohesive energies and underestimated lattice constants. For magnetic systems, i.e., with open d or f shells, the GGA approximation usually gives better results than LDA.

2.1.4 Electron wave functions

Bloch theorem

Bloch's theorem plays a fundamental role in the field of solid-state physics, providing an important framework for understanding the behavior of electrons in periodic potentials. The theorem states that the wave function of an electron in a crystal can be written as a product of a plane wave and a periodic function, known as a Bloch function. This implies that the electronic properties of a crystal are determined not only by the underlying atomic structure, but also by the periodicity of the crystal lattice.

The electronic states in a crystal can be represented by single-particle wave functions, which are the solutions of the Schrödinger equation with a periodic potential $V(\boldsymbol{r})$

$$\left[-\frac{\hbar^2\nabla^2}{2m}+V(\boldsymbol{r})\right]\psi^{\sigma}_{\boldsymbol{k}j}(\boldsymbol{r})=\varepsilon_{j\sigma}(\boldsymbol{k})\psi^{\sigma}_{\boldsymbol{k}j}(\boldsymbol{r}), \tag{2.20}$$

where $\boldsymbol{k}$ is the wave vector, σ denotes the electron spin, and the index j numbers the eigenstates of the Hamiltonian corresponding to energies $\varepsilon_{j\sigma}(\boldsymbol{k})$. According to Bloch's theorem, the electron wave function in a periodic potential takes the form

$$\psi^{\sigma}_{\boldsymbol{k}j}(\boldsymbol{r})=e^{i\boldsymbol{k}\boldsymbol{r}}u^{\sigma}_{\boldsymbol{k}j}(\boldsymbol{r}), \tag{2.21}$$

where $u^{\sigma}_{\boldsymbol{k}j}(\boldsymbol{r})$ is a function that repeats itself periodically and satisfies the requirement $u^{\sigma}_{\boldsymbol{k}j}(\boldsymbol{r})=u^{\sigma}_{\boldsymbol{k}j}(\boldsymbol{r}+\boldsymbol{R}_n)$ for all the translation vectors $\boldsymbol{R}_n$. The Bloch functions are proven to be the eigenvectors of the translation operator

$$\hat{T}_n\psi^{\sigma}_{\boldsymbol{k}j}(\boldsymbol{r})=\psi^{\sigma}_{\boldsymbol{k}j}(\boldsymbol{r}+\boldsymbol{R}_n)=e^{i\boldsymbol{k}(\boldsymbol{r}+\boldsymbol{R}_n)}u^{\sigma}_{\boldsymbol{k}j}(\boldsymbol{r}+\boldsymbol{R}_n)=e^{i\boldsymbol{k}\boldsymbol{R}_n}e^{i\boldsymbol{k}\boldsymbol{r}}u^{\sigma}_{\boldsymbol{k}j}(\boldsymbol{r})=e^{i\boldsymbol{k}\boldsymbol{R}_n}\psi^{\sigma}_{\boldsymbol{k}j}(\boldsymbol{r}). \tag{2.22}$$

The Hamiltonian is invariant under the action of the translation operator, which means that the two operators commute with each other. Bloch's functions are thus also eigenstates of the Hamiltonian, which proves the validity of Bloch's theorem.

Periodic boundary conditions

To describe the electronic states in a crystal with a periodic potential, we need to define the size of the crystal using the number of primitive cells in each direction (N_1, N_2, N_3), where the integer numbers n_i change in the range $n_i = 0, 1, 2, ..., N_i$. When assuming that the wave function has identical values at both ends of the system along each direction, we can apply the Bloch theorem (2.21) to obtain the following condition

$$\psi^{\sigma}_{\boldsymbol{k}j}(\boldsymbol{r}) = \psi^{\sigma}_{\boldsymbol{k}j}(\boldsymbol{r} + N_i\boldsymbol{a}_i) = e^{i\boldsymbol{k}(\boldsymbol{r}+N_i\boldsymbol{a}_i)}u^{\sigma}_{\boldsymbol{k}j}(\boldsymbol{r} + N_i\boldsymbol{a}_i) = e^{i\boldsymbol{k}N_i\boldsymbol{a}_i}\psi^{\sigma}_{\boldsymbol{k}j}(\boldsymbol{r}), \tag{2.23}$$

which is fulfilled when $\boldsymbol{k}N_i\boldsymbol{a}_i = 2\pi n_i$. This relation shows that only discrete $\boldsymbol{k}$ vectors are allowed and the number of wave vectors is equal to the number of primitive cells in the crystal. The conditions imposed on wave functions (2.23) and other physical quantities are called periodic boundary conditions (PBC). In *ab initio* studies, PBC allow performing calculations for crystals or nanosystems using primitive (unit) cells or larger supercells.

Plane waves

When constructing a basis for a quantum mechanical system, it is important to choose a set of functions that can accurately describe the behavior of the particles within the system. While there are many types of basis functions available, the use of plane waves is a common and powerful approach, particularly in the description of the behavior of electrons in a crystal lattice.

Methods of band structure calculations differ from each other in the representations of wave functions used. In general, the wave function can be expressed in the form

$$\psi^{\sigma}_{\boldsymbol{k}j}(\boldsymbol{r}) = \sum_m c^{\sigma}_{jm}(\boldsymbol{k})\phi_{\boldsymbol{k}m}(\boldsymbol{r}), \tag{2.24}$$

were basis functions are denoted by $\phi_{\boldsymbol{k}m}(\boldsymbol{r})$, while the coefficients used to expand the wave function are represented by $c^{\sigma}_{jm}(\boldsymbol{k})$. By expanding the periodic part of the Bloch function in terms of plane waves, the wave function can be written as

$$\psi^{\sigma}_{\boldsymbol{k}j}(\boldsymbol{r}) = e^{i\boldsymbol{k}\boldsymbol{r}}\sum_m c^{\sigma}_{jm}(\boldsymbol{k})e^{i\boldsymbol{G}_{\boldsymbol{m}}\boldsymbol{r}} = \sum_m c^{\sigma}_{jm}(\boldsymbol{k})e^{i(\boldsymbol{k}+\boldsymbol{G}_{\boldsymbol{m}})\boldsymbol{r}}, \tag{2.25}$$

where $\boldsymbol{G}_{\boldsymbol{m}}$ are the reciprocal lattice vectors.

Plane waves are very useful to describe the wave function of an electron in a periodic crystal and the periodic potential it encounters. Using plane waves makes it easier to perform numerical calculations, by applying, e.g., fast Fourier transformation (FFT) algorithm. In practice, the wave functions can be effectively expanded in the plane wave basis only in the interatomic space. In core regions, the wave functions oscillate rapidly and the number of plane waves necessary to describe such behavior is too large for practical applications. To solve this problem, many methods that use the pseudo wave functions and pseudopotentials were developed [73, 74, 75, 76] (see Sec. 2.1.5).

The cut-off energy (E_{cut}) is a parameter that defines how many plane waves are used to calculate wave functions. It establishes the maximum kinetic energy that an electron may have

$$\frac{\hbar^2}{2m}|\boldsymbol{k}+\boldsymbol{G_m}|^2 \leqslant E_{\text{cut}}. \tag{2.26}$$

A higher value for E_{cut} often results in a more accurate result, but it also needs more processing resources. As a consequence, this parameter influences both the accuracy and the computational cost of the calculation. The most matching value for E_{cut} depends on the particular system, and it should be carefully selected to strike a balance between precision and computational effectiveness.

Brillouin zone

The Brillouin zone is a key idea in solid state physics that is used to explain the periodicity of crystals in the reciprocal space. It is defined as the smallest Wigner-Seitz cell of the reciprocal lattice, which houses the reciprocal space's origin. Unique geometrical and symmetry characteristics of the first Brillouin zone are connected with the symmetry of the underlying crystal structure.

In figure 2.1 we can see the representation of Brillouin zones in two-dimensional (2D) simple square lattice. By drawing perpendicular bisectors to the appropriate reciprocal lattice vectors, Brillouin zones for a particular crystal lattice may be created. The shortest reciprocal lattice vector (orange) is often used to begin the construction, followed by the next biggest vector (green), and so on. For the above 2D square lattice, the area designated 1 in this example is known as the first Brillouin zone. The region denoted 2 in the picture is surrounded by perpendicular bisectors corresponding reciprocal lattice vectors (green), and it is called the second Brillouin zone. For actual crystals that have three dimensions, the process for creating Brillouin zones is the same.

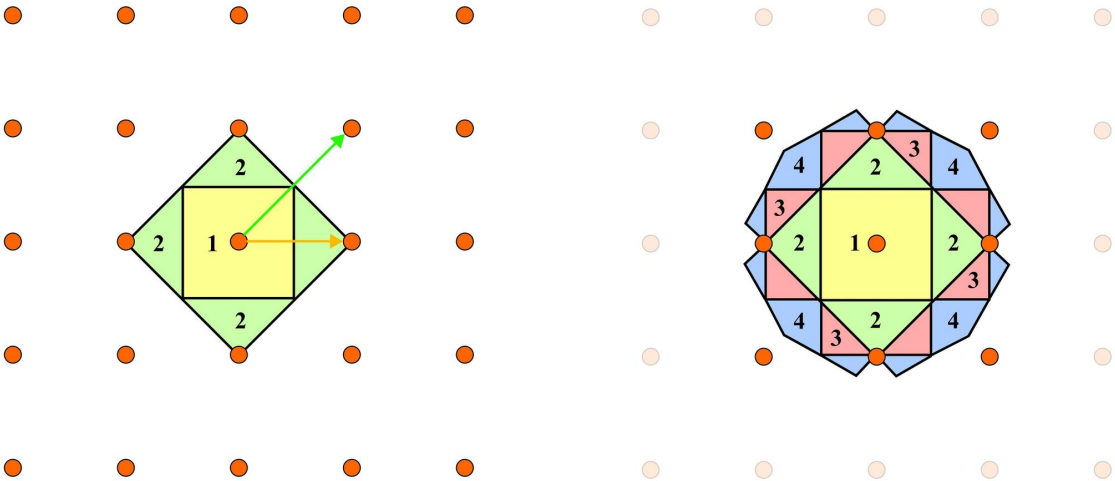

Fig. 2.1. Representation of Brillouin zones.

Summation in reciprocal space

Using the properties of periodic functions, we can properly choose the $\boldsymbol{k}$-points in the first Brillouin zone to minimize the errors in calculation of sums or integrals. The Monkhorst-Pack grid takes advantage of this fact by dividing the reciprocal lattice vectors by an integer value, which leads to a set of $\boldsymbol{k}$-points that are evenly distributed in reciprocal space. This uniform distribution helps to reduce the errors in electronic structure calculations, and ensures that the calculated band structures and other properties are accurate and reliable.

The Monkhorst-Pack (MP) grid [77] is the optimal collection of points, and it can be calculated for three dimensions using the following equation

$$\boldsymbol{k}(n_i) = \frac{2n_i - N_i - 1}{2N_i}\boldsymbol{b}_i, \tag{2.27}$$

where indices n_i take values from 1 to N_i for each $\boldsymbol{i}$=1,2,3, where N_i is the number of $\boldsymbol{k}$-points in the $\boldsymbol{i}$-th dimension. Thus, the set of $\boldsymbol{k}$-points generated by the equation covers the entire Brillouin zone and is evenly spaced in all three dimensions.

Band structure

Band structure is a concept in solid state physics that describes how electrons behave in a crystalline material. It refers to the energy levels of electrons in a material and how they form bands of allowed energy states, which determines the material's electrical and optical properties. The energy level that corresponds to the highest occupied electronic state in a material at absolute zero temperature is known as the Fermi energy.

The band structure of a particular material is made up of all electronic states with energies $\varepsilon^{\sigma}_{\boldsymbol{k}j}$, which are the solutions of the Schrödinger equation (2.20). Energy bands are groups of the accessible electronic states, which correspond to eigenfunctions with index j and spin σ. Regarding shifts by reciprocal lattice vectors $\boldsymbol{G_m}$, eigenenergies corresponding to wave functions (2.25) are periodic

$$\varepsilon^{\sigma}_{\boldsymbol{k}j} = \varepsilon^{\sigma}_{\boldsymbol{k}+\boldsymbol{G_m}j}. \tag{2.28}$$

Therefore, it is sufficient to concentrate on the first Brillouin zone when showing the band structure. Usually, only electronic states for wave vectors $\boldsymbol{k}$ pertaining to specified directions and high symmetry locations in the reciprocal space are shown. In systems with magnetic ordering, due to the exchange splitting the energy of the bands assume different values for the two spin directions, $\varepsilon^{\uparrow}_{\boldsymbol{k}j} \neq \varepsilon^{\downarrow}_{\boldsymbol{k}j}$.

An important quantity characterizing the band structure is the density of electronic states for a given spin direction $\rho_{\sigma}(E)$, which is calculated as a sum over the first Brillouin zone

$$\rho_{\sigma}(E) = \frac{1}{N_k} \sum_{j,\boldsymbol{k}} \delta(\varepsilon^{\sigma}_{\boldsymbol{k}j} - E), \tag{2.29}$$

where N_k is the number of wave vectors $\boldsymbol{k}$ in the first Brillouin zone. The sum of the two spin components, $\rho(E) = \rho_{\uparrow}(E) + \rho_{\downarrow}(E)$, determines the overall density of states. The tetrahedron approach, as opposed to the Monkhorst-Pack grid, is frequently employed in the density of states computation. With this approach, the Brillouin zone as a whole is divided into tetrahedra, and the energy of states at positions $\boldsymbol{k}$ corresponding to the vertices of the tetrahedra are calculated. Utilizing linear interpolation, the energy between these points are computed.

2.1.5 Pseudopotentials

Definition of pseudopotential

Pseudopotentials also known as effective core potentials (ECP) are commonly used in first principles studies to simplify electronic structure calculations by replacing inner core electrons with a spherically symmetric potential. This reduces computational complexity and allows focusing on the more chemically relevant valence electrons. Pseudopotentials are created using a combination of empirical and theoretical methods, and are especially useful for large systems where electronic structure calculations require significant computational resources. However, it is important to carefully select pseudopotentials to ensure reliable and accurate results.

The primary concept behind the pseudopotential is depicted in Fig. 2.2. Essentially, in the atomic core region (where r is less than the cutoff radius r_c), the exact

potential V is approximated using a pseudopotential $\tilde{V}$ that has a finite value at $r = 0$. The corresponding pseudo wave function $\tilde{\Psi}$ is smooth and does not contain oscillations or nodal points in this region. However, for r values greater than r_c, the pseudopotential is identical to the exact potential, and the pseudo wave function is equivalent to the exact wave function Ψ. This approximation allows the pseudo wave function to be expanded into plane waves throughout the entire crystal region.

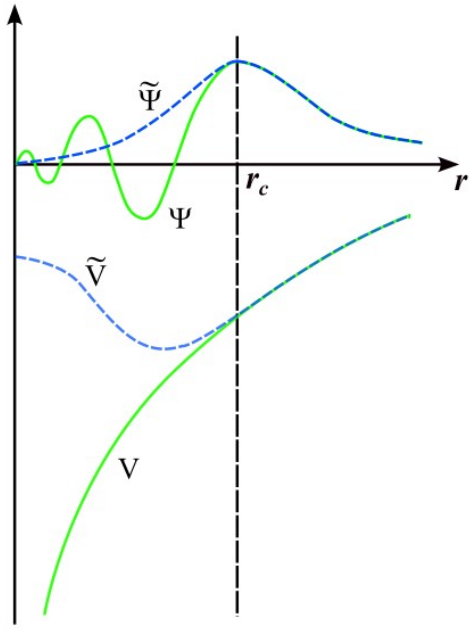

Fig. 2.2. A wave function in the nucleus's Coulomb potential (green) is compared to one in the pseudopotential (blue).

Here are some examples of pseudopotentials:

- **Norm-conserving pseudopotentials** [73]: These are a type of pseudopotential that aims to conserve the norm of the wave function, which ensures that the total electronic charge is conserved. Norm-conserving pseudopotentials were introduced by Hamann and Vanderbilt in 1985, and are widely used in both plane-wave and localized basis set electronic structure calculations.

- **Ultrasoft pseudopotentials** [74]: Pseudopotentials that allow for a more flexible description of the valence electrons by using a set of "ultrasoft" basis functions. They were introduced by Vanderbilt in 1990, and are widely used in plane-wave electronic structure calculations. Ultrasoft pseudopotentials can be constructed using a variety of methods, including density functional theory and many-body perturbation theory.

- **Hartwigsen-Goedecker-Hutter (HGH) pseudopotentials** [75]: These are a type of pseudopotential that were introduced by Hartwigsen, Goedecker, and Hutter in 1998. HGH pseudopotentials are norm-conserving and use a non-linear core correction to improve their accuracy. They are widely used in both plane-wave and localized basis set electronic structure calculations.

- **Projector augmented-wave (PAW) pseudopotentials** [76]: A type of pseudopotentials that were introduced by Blöchl in 1994, and have become a popular choice in electronic structure calculations. PAW pseudopotentials use a partial wave expansion to represent the core electrons, and augment this with a set of projector functions that are used to describe the valence electrons. PAW pseudopotentials can accurately describe both the core and valence electron behavior, while still allowing for efficient electronic structure calculations.

These are just a few examples of the many different types of pseudopotentials that are available for use in electronic structure calculations. The choice of pseudopotential will depend on the specific needs of the calculation and the accuracy required. In the present studies, we use the PAW pseudopotentials, which will be described in more detail in the next section.

Projector augmented-wave method

The PAW method is a widely used approach in electronic structure calculations that enables accurate and efficient treatment of valence electrons. It was first proposed by Blöchl in 1994 [76] and has become a popular choice due to its high accuracy and computational efficiency. In the PAW method, the electrons in core regions are described by a set of pseudo wave functions that are defined by a set of projectors. These projectors are chosen to match the exact wave functions of the isolated atom, and are then used to construct a pseudo Hamiltonian that includes the effect of the core electrons. The valence electrons are treated using a set of auxiliary basis functions that are augmented with the projectors, enabling accurate description of their behavior. The PAW method has been implemented in a range of electronic structure codes and has been successfully used in a variety of applications, including studies of catalysis, surface chemistry, and solid-state physics.

The discussed pseudopotential methods allow for efficient calculation of many physical quantities based on pseudo wave functions. In many cases, more accurate calculations require knowledge of the wave functions of valence electrons, as well as in the atomic core region. The PAW method combines the efficiency of pseudopotentials and the accuracy of full-potential methods. This approach also utilizes pseudo

wave functions $\tilde{\psi}_v$ to describe the valence electrons, which are expanded in plane waves and in the interstitial region match the exact wave functions ψ_v. The main advantage of this method is the ability to determine the exact wave function through a linear transformation of the pseudo wave function

$$|\psi_v\rangle = \mathcal{T}|\tilde{\psi}_v\rangle = (1 + \sum_m \mathcal{T}_m)|\tilde{\psi}_v\rangle. \tag{2.30}$$

In this formula, the operator $\mathcal{T}$ represents the transformation operator that maps the pseudo wave function to the valence wave function. This transformation is necessary because the pseudo wave function is not an exact representation of valence electrons in the core region. The linear operators $\mathcal{T}_m$ act in the core regions for $r \leqslant r_c$ at atomic positions $\boldsymbol{R}_m$. We utilize local bases $|\phi_m\rangle$ and $|\tilde{\phi}_m\rangle$ to expand both functions in the core region

$$|\psi_v\rangle = \sum_m c_m|\phi_m\rangle, \tag{2.31}$$

$$|\tilde{\psi}_v\rangle = \sum_m c_m|\tilde{\phi}_m\rangle, \tag{2.32}$$

with the same coefficients c_m, therefore, the base functions are linked by the same linear transformation, $|\phi_m\rangle = (1 + \sum_m \mathcal{T}_m)|\tilde{\phi}_m\rangle$. For $r > r_c$, the functions are equal, i.e., $|\phi_m\rangle$ is identical to $|\tilde{\phi}_m\rangle$.

The states $|\phi_m\rangle$ are solutions of the Schrödinger equation for the exact atomic potential and are orthogonal to the core states. Each $|\phi_m\rangle$ state corresponds to one pseudo state $|\tilde{\phi}_m\rangle$. By subtracting equations (2.31) and (2.32), we obtain a set of equations that describe the difference between the exact and pseudopotential solutions

$$|\psi_v\rangle = |\tilde{\psi}_v\rangle - \sum_m c_m|\tilde{\phi}_m\rangle + \sum_m c_m|\phi_m\rangle. \tag{2.33}$$

This set of equations can be used to calculate the wave functions in core regions and corresponding eigenvalues. The equation (2.33) can be better understood through the introduction of a scheme presented in Fig. 2.3. This scheme outlines a method in which an exact wave function can be obtained through a combination of a pseudo-onsite partial waves obtained on a radial grid extracted from the pseudo wave function, which utilizes a plane wave basis, and an exact-onsite partial waves. The pseudo-onsite partial waves are used to represent the electron density in the core region and it is obtained from the pseudopotential approximation. The exact-onsite partial waves, on the other hand, represents the electron density in the core region calculated from the exact atomic potential. By combining these two types of partial waves, we obtain an exact wave function that accurately represents the behavior of electrons in both the core and valence regions of the crystal.

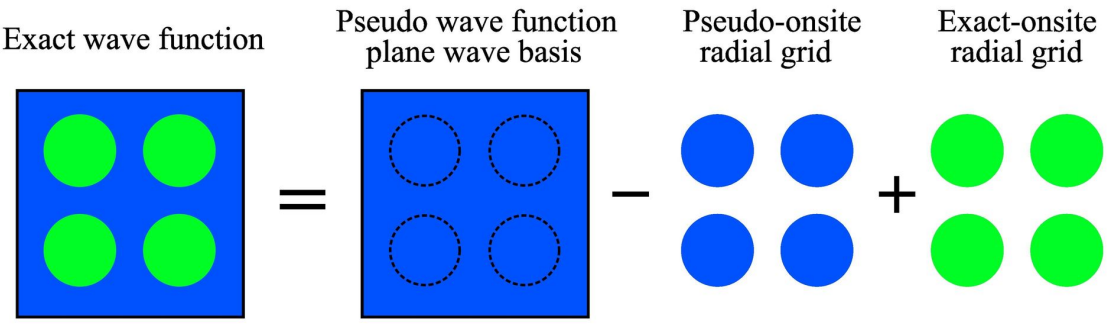

Fig. 2.3. Schematic visualization of the PAW method.

The linearity of the operator $\mathcal{T}$ is dependent on the linearity of coefficients c_m, which are linear functionals of $|\tilde{\psi}_v\rangle$ and can be expressed as

$$c_m = \langle \tilde{p}_m | \tilde{\psi}_v \rangle. \tag{2.34}$$

The projectors $\langle \tilde{p}_m|$ are dual to pseudo states and satisfy the condition $\langle \tilde{p}_m | \tilde{\phi}_n \rangle = \delta_{mn}$, while the sum of all pseudo states satisfies the condition $\sum_m |\tilde{\phi}_m\rangle\langle\tilde{p}_m| = 1$.

From equations (2.33) and (2.34) we get the transformation of the pseudo wave function of the valence electrons in the PAW method to obtain the wave function of the valence electrons, including the correction due to the presence of the core electrons

$$|\psi_v\rangle = |\tilde{\psi}_v\rangle + \sum_m (|\phi_m\rangle - |\tilde{\phi}_m\rangle)\langle\tilde{p}_m|\tilde{\psi}_v\rangle = \left[1 + \sum_m (|\phi_m\rangle - |\tilde{\phi}_m\rangle)\langle\tilde{p}_m|\right]|\tilde{\psi}_v\rangle, \tag{2.35}$$

The wave function $|\tilde{\psi}_v\rangle$ represents the valence electrons in the PAW method, and it is related to the wave function $|\psi_v\rangle$ by the transformation given in the equation (2.30) with the operator

$$\mathcal{T} = 1 + \sum_m (|\phi_m\rangle - |\tilde{\phi}_m\rangle)\langle\tilde{p}_m|. \tag{2.36}$$

To use the PAW method, a set of PAW potentials for the elements in the system must first be generated. These potentials can be obtained from a variety of sources, including databases such as the Materials Project [78] or from first-principles calculations. Once the PAW potentials have been obtained, they can be used in electronic structure calculations with various software packages, such as VASP [79, 80], Quantum ESPRESSO [81], and ABINIT.

2.2 Equation of state

The Murnaghan equation of state is a commonly used model in condensed matter physics and materials science to describe the behavior of solids under compression [82]. It is a polynomial function that relates the pressure and volume, and it is based on the assumption that the interatomic forces are harmonic. The general Murnaghan equation of state can be written as

$$P(V) = \frac{B_0}{B_0'}\Big[\Big(\frac{V}{V_0}\Big)^{-B_0'} - 1\Big], \tag{2.37}$$

where B_0 is the bulk modulus for $P = 0$, defined as

$$B_0 = -V\Big(\frac{\partial P}{\partial V}\Big)_{P=0}, \tag{2.38}$$

and B_0' is the derivative of the bulk modulus with respect to pressure.

By integrating Eq. (2.37) we obtain the dependence of total energy on volume

$$E(V) = E_0 + B_0 V_0\Big[\frac{1}{B_0'(B_0'-1)}\Big(\frac{V}{V_0}\Big)^{1-B_0'} + \frac{1}{B_0'}\frac{V}{V_0} - \frac{1}{B_0'-1}\Big], \tag{2.39}$$

where E_0 is the energy at equilibrium volume V_0. By fitting the total energy to volume and finding its minimal value, the three parameters, which describe the equilibrium state of the crystal, V_0, B_0, and B_0', can be determined.

2.3 Strongly correlated systems

2.3.1 Mott insulators

In systems, where the electronic states resemble localized atomic orbitals due to electron correlations, the standard band theory breaks down. In order to include local Coulomb interactions, Hubbard proposed a model based on the tight-binding approximation, which describes electrons moving in a periodic potential [83]. In the most basic case, we examine single s orbitals at atomic sites. A local Coulomb interaction with a fixed energy U is added to the Hamiltonian to take into account electron correlations in the same orbital. Using the second quantization formalism, the Hubbard model can be written in the form

$$H = \sum_{i,j,\sigma} t_{ij} c_{i\sigma}^{\dagger} c_{j\sigma} + U \sum_i n_{i\uparrow} n_{i\downarrow}, \tag{2.40}$$

where $c_{i\sigma}^{\dagger}$ and $c_{i\sigma}$ are the creation and annihilation operators of an electron with spin σ in the localized Wannier orbital $w(\boldsymbol{r} - \boldsymbol{R}_i)$ at site i, and $n_{i\sigma} = c_{i\sigma}^{\dagger} c_{i\sigma}$ is the particle

number operator. The hopping integrals are given by the formula

$$t_{ij} = \int d\boldsymbol{r} w^*(\boldsymbol{r} - \boldsymbol{R}_i) H_0 w(\boldsymbol{r} - \boldsymbol{R}_j), \tag{2.41}$$

where the single-particle Hamiltonian H_0 is made up of effective atomic potential for $i = j$ and kinetic energy for $i \neq j$. Only the hopping integrals between the nearest neighbors are typically taken into account.

The energy of the Coulomb interaction between two electrons in the same orbital is given by the formula

$$U_i = \int d\boldsymbol{r} d\boldsymbol{r}' |w(\boldsymbol{r} - \boldsymbol{R}_i)|^2 \frac{e^2}{|\boldsymbol{r} - \boldsymbol{r}'|} |w(\boldsymbol{r} - \boldsymbol{R}_i)|^2. \tag{2.42}$$

Mott insulators are a type of materials, whose electronic behavior is determined by strong Coulomb interactions between electrons. The energy gap in this case is primarily due to the discontinuity in the energy functional ($\Delta_{\mathrm{xc}} > 0$) that occurs when the orbital states are filled. The standard approximations used in DFT to calculate the energy gap Δ_{KS} show that it is either zero or very small. It is understandable since the value of the energy gap in Mott insulators is related to the Coulomb interaction energy U, which is not properly included in LDA and GGA. In transition metals, U can be thought of as the energy required for an electron to transfer between two atoms with an initial d-state occupancy of d^n. This process leads to an increase in the number of electrons per atom on one of the atoms d^{n+1} and a decrease on the other d^{n-1}, therefore, the energy is given by this equation

$$U = E(d^{n+1}) + E(d^{n-1}) - 2E(d^n), \tag{2.43}$$

where $E(d^n)$ is the total energy of the system in which a single atom is occupied with d^n electrons. This relationship means that the energy gap itself should be a linear function of U.

2.3.2 DFT+U method

Anisimov, Zaanen, and Andersen proposed the LDA+U method in 1991 [84]. The concept was to relate the single-particle potentials to the local Coulomb interactions described by the Hubbard parameter U. There are a few versions of the LDA+U method [84, 85, 86] that have been developed, which differ in their approach to describing local electron interactions. However, they all use a similar scheme to calculate the total energy with the following formula

$$E_{\mathrm{tot}} = E_{\mathrm{DFT}} + E_U - E_{\mathrm{dc}}, \tag{2.44}$$

where E_{DFT} is the energy obtained using the density functional theory within LDA or GGA, E_U is the energy of local electron interactions, and E_{dc} is the energy of the Coulomb interactions that is approximately included in the DFT functional.

In the rotationally invariant version of DFT+U [85], the electron interactions are described by the formula

$$\begin{aligned} E_U = \frac{1}{2} \sum_{i,\{m\},\sigma} \Big[& \langle m, m'' | V_{ee} | m', m''' \rangle n_{i\sigma}^{mm'} n_{i-\sigma}^{m''m'''} \\ & + \left(\langle m, m'' | V_{ee} | m', m''' \rangle - \langle m, m'' | V_{ee} | m''', m' \rangle \right) n_{i\sigma}^{mm'} n_{i\sigma}^{m''m'''} \Big], \end{aligned} \tag{2.45}$$

where i indexes the sites of the lattice, $\{m\} = (m, m', m'', m''')$ are the magnetic quantum numbers, and the matrix elements of the Coulomb interaction are given by the equation

$$\langle m, m'' | V_{ee} | m', m''' \rangle = \int dr \int dr' \phi_{lm}^*(r) \phi_{lm'}(r) \frac{e^2}{|r - r'|} \phi_{lm''}^*(r') \phi_{lm'''}(r'). \tag{2.46}$$

The wave functions appearing under the integral are defined for the orbital quantum number l, which defines the range of the magnetic quantum numbers $-l \leq \{m\} \leq l$. The occupation numbers of atomic orbitals form a second-order tensor, whose elements are determined by projecting the Kohn-Sham wave functions ψ_{kj}^{σ} onto atomic orbitals

$$n_{i\sigma}^{mm'} = \sum_{k,j} f_{kj}^{\sigma} \langle \psi_{kj}^{\sigma} | \phi_{lm'} \rangle \langle \phi_{lm} | \psi_{kj} \rangle. \tag{2.47}$$

The effective parameters that define the local Coulomb (U) and Hund's exchange (J) interactions can be expressed by the equations

$$U = \frac{1}{(2l+1)^2} \sum_{m,m'} \langle m, m' | V_{ee} | m, m' \rangle = F^0, \tag{2.48}$$

$$J = \frac{1}{2l(2l+1)} \sum_{m \neq m'} \langle m, m' | V_{ee} | m', m \rangle = \frac{F^2 + F^4}{14}, \tag{2.49}$$

where F^0, F^2, and F^4 are Slater integrals.

Using these parameters, we can write the last term in the formula (2.44) in the following form [85]

$$E_{dc} = \frac{1}{2} \left[\sum_i U n_i (n_i - 1) - J \left[n_{i\uparrow}(n_{i\uparrow} - 1) + n_{i\downarrow}(n_{i\downarrow} - 1) \right] \right], \tag{2.50}$$

where $n_{i\sigma} = \mathrm{Tr}(n_{i\sigma}^{mm'})$ and $n_i = n_{i\uparrow} + n_{i\downarrow}$ is the total occupancy of orbitals at site i. The parameters U and J refer to isolated atoms, but the actual value of U used for a specific type of atom takes into account the influence of electron screening and is

specific to the type of material. The value of U for a given system can be estimated using the linear response method by calculating the change in the occupation of electronic states on a particular atom when it is subjected to a local potential [87]. The second parameter J is less sensitive to the type of material and is often obtained from Eq. (2.49).

2.4 Van der Waals interaction

The influence of long-range electron correlations, which are not included in the traditional exchange-correlation functionals, is known as the van der Waals (vdW) or dispersion interaction. It is an attractive interaction that is crucial in molecular crystals such as noble gas crystals with closed electron shells and materials made mostly of neutral molecules. The vdW interactions between atoms and molecules play an important role in many chemical systems. They control, for instance, the structures of DNA and proteins, the packing of crystals, the formation of aggregates, host-guest systems, or the orientation of molecules on surfaces or in molecular films. They are in precise balance with electrostatic and exchange-repulsion interactions.

The electric dipole on one atom (molecule) experiences quantum fluctuations that cause an electric dipole to form on another atom (molecule). Weak attraction of atoms or molecules results from the interaction of these dipoles. The electric field generated by the dipole moment p_1 at the distance R may be described by the following classical formula

$$\mathscr{E} = \frac{p_1}{R^3}. \tag{2.51}$$

If an electric field acts on a molecule with polarizability α, it induces a dipole moment

$$p_2 = \frac{\alpha p_1}{R^3}. \tag{2.52}$$

The average energy of the two dipoles' interaction is

$$E_{\mathrm{vdW}} = -\mathscr{E} p_2 = -\frac{\alpha p_1^2}{R^6}. \tag{2.53}$$

The interaction strength and polarizability must be accurately determined by going beyond the most basic of random-phases approximation (RPA). Taking into consideration electron correlations inside the perturbation theory results in the interaction being dependent on the distance $\sim R^{-6}$.

2.4.1 D2 and D3 methods

The estimated value of the vdW interaction energy can be used in the DFT calcu-

lation as a correction to the total energy of the system

$$E_{\text{tot}} = E_{\text{DFT}} + E_{\text{vdW}}, \tag{2.54}$$

where E_{DFT} is a self-consistent Kohn-Sham functional. According to this method, the vdW interaction just modifies the distance between atoms and has no direct impact on the electronic structure.

In the version proposed by Grimme (D2) [88, 89], the dependence of vdW energy on the distance between atoms R_{ij} has the form

$$E_{\text{vdW}} = -\frac{1}{2}\sum_{i,j} f_{\text{d}}(R_{ij})\frac{C_{6ij}}{R_{ij}^6}, \tag{2.55}$$

where the damping function f_{d} precludes duplicate accounting for correlation effects at intermediate distances while defining the asymptotic behavior for $R_{ij} \to 0$. Its goal is to guarantee that the vdW interaction is constrained to distances bigger than the lengths of normal bonds, as accurately predicted by conventional functionals. For each pair of atoms, the dispersion coefficients C_{6ij} are defined as the geometric mean of the atomic parameters.

Grimme extended the D2 method by including the second term proportional to R^{-8} (D3) [90]

$$E_{\text{vdW}} = -\frac{1}{2}\sum_{i,j}\left[f_{\text{d},6}(R_{ij})\frac{C_{6ij}}{R_{ij}^6} + f_{\text{d},8}(R_{ij})\frac{C_{8ij}}{R_{ij}^8}\right]. \tag{2.56}$$

2.4.2 Tkatchenko-Scheffler method

The Tkatchenko and Scheffler (TS) method only considers the term proportional to R^{-6}, but it also takes into consideration how the charge density affects the dispersion coefficients and cut-off radius. In the approaches being discussed, it is assumed that only two-body interactions are present, and the influence of the surrounding atoms or molecules on the van der Waals interaction is not considered. In an enhanced version of the TS method, self-consistent long-range electrical shielding is taken into account [91].

The dispersion energy is calculated using the same equations as in the D2 and D3 methods, but with modified dispersion coefficients and cut-off radii

$$C_{6i} = \frac{3}{\pi}\int_0^\infty d\omega \left[\alpha_i^{\text{SCS}}(\omega)\right]^2, \tag{2.57}$$

where $\alpha_i^{\text{SCS}}(\omega)$ represents the frequency-dependent dynamic polarizability of the i-th atom. Overall, the D2, D3, and TS approaches calculate van der Waals interactions with varying degrees of precision. These methods are implemented in VASP, and were tested in this work to investigate the impact of van der Waals interactions in the characteristics and behavior of pyrophosphate systems.

Chapter 3

Phonon calculations

Phonons are quasiparticles that represent the collective excitation of lattice vibrations in solids. They are important because they determine the physical properties of materials, such as their thermodynamic properties, structural phase transitions, thermal and electrical conductivity, superconductivity, elasticity connected with the ability to transmit sound, and many others.

One way to calculate the phonon spectrum of a material is to use DFT to compute the electronic structure and interatomic forces within a supercell, as the response to the displacements of atoms. Then this information is used to construct the interatomic force constants (IFC) matrix, which describes the interactions between atoms in the lattice, and the dynamical matrix, which is the Fourier transform of the IFC matrix. The eigenvalues and eigenvectors of the dynamical matrix correspond to the phonon frequencies and polarization vectors, respectively. This approach is called the direct method or the Parlinski-Li-Kawazoe method [92], and it will be described in details in Sec. 3.2. The alternative method of phonon calculations is the density functional perturbations' theory (DFPT) [93], which allows to calculate the dynamical matrix within the second order perturbation theory. Both these approaches use the harmonic approximation, which assumes that the atomic vibrations in the lattice can be described by harmonic oscillators. This allows one to express the potential energy of the lattice as a sum of harmonic terms, and then use this to derive the dynamical matrix. The direct method was generalized to include the anharmonic corrections within the temperature dependent effective potential (TDEP) approach [94], which will be described in Sec. 3.5.

The calculated phonon spectrum can be used to predict the physical properties of the material, such as its heat capacity, thermal conductivity, and elastic constants. It can also be compared to experimental measurements of these properties to validate the accuracy of the calculations. Overall, the calculation of phonon properties is an

important tool for understanding the behavior of materials and for designing new materials with specific properties.

3.1 Lattice dynamics theory

The total energy of a given system is a function of atomic positions within a crystal lattice. The positions of atoms are typically represented by vectors $\boldsymbol{R}^{\mu}_{\boldsymbol{m}}$, where $\boldsymbol{m}$ is the index of the primitive unit cell and μ numbers atoms within that cell. We also introduce the vectors of atom displacements from the equilibrium positions, $\boldsymbol{U}^{\mu}_{\boldsymbol{m}} = \boldsymbol{R}^{\mu}_{\boldsymbol{m}} - \boldsymbol{R}^{0\mu}_{\boldsymbol{m}}$. Assuming that atomic displacements are much smaller than interatomic distances, the total energy can be written as the Taylor expansion

$$E = E_0 + \sum_{N=2} \frac{1}{N!} \sum_{\boldsymbol{m}_1\alpha_1,\ldots,\boldsymbol{m}_N\alpha_N} \sum_{\mu_1,\ldots,\mu_N} \Phi^{\mu_1,\ldots,\mu_N}_{\boldsymbol{m}_1\alpha_1,\ldots,\boldsymbol{m}_N\alpha_N} U^{\mu_1}_{\boldsymbol{m}_1\alpha_1} \ldots U^{\mu_N}_{\boldsymbol{m}_N\alpha_N}, \tag{3.1}$$

where $\alpha = x, y, z$, E_0 is the ground state energy, and $\Phi^{\mu_1,\ldots,\mu_N}_{\boldsymbol{m}_1\alpha_1,\ldots,\boldsymbol{m}_N\alpha_N}$ is the Nth-order derivative of E called the interatomic force constant (IFC)

$$\Phi^{\mu_1,\ldots,\mu_N}_{\boldsymbol{m}_1,\ldots,\boldsymbol{m}_N\alpha_N} = \left. \frac{\partial^N E}{\partial U^{\mu_1}_{\boldsymbol{m}_1\alpha_1} \ldots \partial U^{\mu_N}_{\boldsymbol{m}_N\alpha_N}} \right|_{U^{\mu_1}_{\boldsymbol{m}_1\alpha_1}=\cdots=0}. \tag{3.2}$$

The ground state obtained within DFT is a stationary state of the lowest energy E_0, in which all atoms are placed in the equilibrium positions. Therefore, all first order derivatives of the energy with respect to the atomic displacements are equal to zero. When an atom is displaced from its equilibrium position, it generates a force acting on this atom and forces on all other atoms in the crystal lattice. These forces can be calculated using the Hellmann-Feynman (HF) theorem [95, 96], which states that the derivative of the total energy of a system with respect to a given atomic displacement is equal to the negative of the force exerted on that atom due to the other atoms in the system, with all other atomic coordinates held fixed

$$F^{\mu}_{\boldsymbol{m}\alpha} = -\frac{\partial E}{\partial U^{\mu}_{\boldsymbol{m}\alpha}}. \tag{3.3}$$

Therefore, by calculating the forces on each atom in the crystal lattice using the HF theorem, one can determine the equilibrium atomic positions and explore the vibrational properties of the system, such as phonon spectra and thermodynamic functions.

The standard approach used in phonon calculations is the harmonic approximation (HA), in which we assume that atomic displacements are small. This condition is usually fulfilled at low temperatures. In this case, the expansion in Eq. (3.1) can

be restricted to the first term with $N = 2$. By applying Eq. (3.3) to the total energy E calculated for the harmonic potential, we obtain the linear dependence of forces on atomic displacements

$$F^{\mu}_{\boldsymbol{m}\alpha} = -\sum_{\beta,l,\nu} \Phi^{\mu,\nu}_{\boldsymbol{m}\alpha,\boldsymbol{l}\beta} U^{\nu}_{l\beta}, \tag{3.4}$$

where $\Phi^{\mu,\nu}_{\boldsymbol{m}\alpha,\boldsymbol{l}\beta}$ are the matrix elements of the 2nd-order IFC matrices. Based on the above equation (3.4) we can write the equation of motion in the following form

$$M_{\mu}\frac{\partial^2 U^{\mu}_{\boldsymbol{m}\alpha}}{\partial t^2} = -\sum_{\beta,l,\nu} \Phi^{\mu,\nu}_{\boldsymbol{m}\alpha,\boldsymbol{l}\beta} U^{\nu}_{l\beta}, \tag{3.5}$$

where M_{μ} is the mass of atom μ. This equation describes the movement of atom μ in the harmonic potential under the influence of other atoms.

Within HA vibrations of atoms can be described in terms of independent normal modes, which are called phonon modes, with well-defined wave vector $\boldsymbol{k}$ and the branch number j. Therefore, the solution of Eq. (3.5) is given by the plane wave in the form

$$U^{\mu}_{\boldsymbol{m}\alpha} = \frac{1}{\sqrt{M_{\mu}}}\varepsilon^{\mu}_{\alpha}(\boldsymbol{k}, j)e^{i(\boldsymbol{k}\boldsymbol{R}_m - \omega_{\boldsymbol{k},j}t)}, \tag{3.6}$$

where $\boldsymbol{R}_m$ is the vector defining the position of the primitive cell m and $\varepsilon^{\mu}_{\alpha}(\boldsymbol{k}, j)$ are the components of the polarization vector, describing the displacement of atom μ along the α direction within a given phonon mode.

The dynamical matrix is a Fourier transform of the force constant matrix, and it is defined as

$$D(\boldsymbol{k}) = \frac{1}{\sqrt{M_{\mu}M_{\nu}}}\sum_{\boldsymbol{m}} \Phi^{\mu,\nu}_{0,\boldsymbol{m}} \exp\left[-2\pi i \boldsymbol{k}\cdot(\boldsymbol{R}^{\mu}_0 - \boldsymbol{R}^{\nu}_{\boldsymbol{m}})\right]. \tag{3.7}$$

Introducing Eq. (3.6) into Eq. (3.5) and using Eq. (3.7) we obtain the eigenequation

$$\omega^2(\boldsymbol{k}, j)\boldsymbol{\varepsilon}(\boldsymbol{k}, j) = D(\boldsymbol{k})\boldsymbol{\varepsilon}(\boldsymbol{k}, j), \tag{3.8}$$

from which phonon frequencies and polarization vectors are obtained. Phonon frequencies are directly related to phonon energies, $E_{\boldsymbol{k},j} = \hbar\omega_{\boldsymbol{k},j}$, and polarization vectors describe the displacements of atoms given by Eq. (3.6).

Phonon dispersion relations

The relationship between the frequency and wave vector of phonons is described by phonon dispersion curves obtained by Eq. (3.8). In the theoretical study of phonons, it is common to focus on the first Brillouin zone, which is a primitive, Wigner-Seitz cell of the reciprocal lattice, therefore, it contains all the unique wave vectors that fully

describe the lattice vibrations. High-symmetry points within the first Brillouin zone are usually used as reference points for analyzing the dispersion relations. These points correspond to specific wave vectors that possess higher degree of symmetry than others.

When studying the dispersion relations, we can distinguish between two types of phonons: optical and acoustic waves. Optical phonons involve the out-of-phase vibrations of atoms that may result in changes of the electric polarization and the interaction with electromagnetic waves. These phonons are associated with higher frequencies and are observed in materials with more than one atom in the primitive cell. Acoustic phonons, on the other hand, are related to coherent movements of atoms, and they are associated with the elastic properties and propagation of sound. The number of all phonon dispersion curves is equal to the number of degrees of freedom within the primitive cell $r = 3N_\mathrm{p}$, where N_p is the number of atoms in the primitive cell. In three-dimensional (3D) crystals, there are 3 acoustic branches and $3N_\mathrm{p} - 3$ optical branches of the dispersion relations.

Additionally, we can divide all phonons into longitudinal and transverse modes. Longitudinal phonons involve vibrations where the displacement of atoms is parallel to the direction of propagation, while transverse phonons represent vibrations with displacements perpendicular to the propagation direction. In 3D systems, there is one longitudinal acoustic (LA) mode and two transverse acoustic (TA) modes. The number of longitudinal optic (LO) and transverse optic (TO) modes depends on the crystal symmetry.

Phonon density of states

The phonon density of states describes the frequency distribution of normal modes in a material. It is derived by building a histogram based on the phonon dispersion relations, which connect phonon frequencies with wave vectors, $\omega(\boldsymbol{k}, j)$, calculated using Eq. (3.8). Binning these points into frequency intervals produces a histogram that displays the distribution of phonon frequencies in the crystal. For the frequency bin size $\Delta\omega$ this histogram takes the form

$$g(\omega) = \frac{1}{nd\Delta\omega} \sum_{\boldsymbol{k},j} \delta_{\Delta\omega}(\omega - \omega(\boldsymbol{k}, j)), \tag{3.9}$$

where

$$\delta_{\Delta\omega}(x) = \begin{cases} 1 & \text{if } -\frac{\Delta\omega}{2} < x \leqslant \frac{\Delta\omega}{2}, \\ 0 & \text{otherwise.} \end{cases} \tag{3.10}$$

The summation is performed over wave vectors $\boldsymbol{k}$ within the first Brillouin zone and all phonon branches j. The wave vectors $\boldsymbol{k}$ may be randomly selected with a uniform

distribution across the Brillouin zone, or generated using the MP grid [77]. The variable n represents the number of sampled wave vector points, while d corresponds to the dimension of the dynamical matrix, as indicated by Eq. (3.8). In this case, $d = r$, where r represents the number of degrees of freedom in the primitive unit cell.

The partial phonon density of states, which describes the contribution to the density of states of the selected atom μ vibrating along a given direction, can be calculated using the following matrix

$$g_{il,\mu} = \frac{1}{nd\Delta\omega} \sum_{\boldsymbol{k},j} \varepsilon_i^{\mu}(\boldsymbol{k},j)\varepsilon_l^{\mu *}(\boldsymbol{k},j)\delta_{\Delta\omega}(\omega - \omega(\boldsymbol{k},j)), \tag{3.11}$$

where $\varepsilon_i^{\mu}(\boldsymbol{k},j)$ and $\varepsilon_l^{\mu}(\boldsymbol{k},j)$ are the components of the polarization vectors.

3.2 Direct method

The first *ab initio* approach to calculate phonon dispersion relations was the frozen-phonon method [97], in which the phonon energy is calculated as the difference in the energies of the distorted and ideal crystals. Frank, Elsässer, and Fähnle effectively employed the direct method that involves calculating force constants from HF forces, to determine the phonon dispersion curves for alkali metals such as Li, Na, and K [98]. Meanwhile, Kresse, Furthmüller, and Hafner used the same method to determine the phonon dispersion curves for diamond and graphite [99]. The direct method was further developed and applied to the system with the soft mode by Parlinski, Li, and Kawazoe [92]. This modified and generalized version of the conventional direct method, which is called the Parlinski-Li-Kawazoe method, is implemented in the Phonon program and has been used to study hundreds of crystalline systems.

The direct method consists of a few steps. First, we optimize the crystal supercell by calculating its electronic structure and interatomic forces using the HF theorem (3.3). The relaxation is finished when forces acting on all atoms are equal to zero or their values are smaller than the assumed maximal force. Second, the HF forces are calculated by making small displacements from equilibrium positions of one atom at a time. The number of necessary displacements is determined by the number of nonequivalent atoms in the primitive cell and the site symmetry of a given atom. Next, from the linear dependence of HF forces on atomic displacements (3.4), the force constants matrix elements are derived. The number of HF force components is usually larger than the number of independent force constants when we consider the crystal symmetry. To fit the independent force constants to the HF force components, we use the singular value decomposition method as proposed in Ref. [92]. In the final

step, the dynamical matrix is derived for each wave vector $\boldsymbol{k}$ using Eq. (3.7) and it is diagonalized to obtain phonon frequencies and polarization vectors.

In nonmetallic materials, the LO-TO splitting is a common phenomenon observed in phonon dispersion curves [100]. It arises due to the coupling of long-wavelenght phonons with electromagnetic fields, generated by ions displaced from their equilibrium positions. This additional electric polarization affects the infrared LO modes with the wave vectors close to the Γ point, leading to the splitting of the degenerated dispersion curves into the LO and TO branches. The LO-TO splitting is particularly prominent in polar crystals, such as ferroelectrics, where the displacement of atoms induces the structural transition to the phase with a non-zero electric polarization. In the direct method, the LO-TO splitting is calculated by adding to the dynamical matrix the non-analytical term, which includes the Born effective charges and dielectric constants derived for a given material [101].

3.3 Raman scattering

The Raman effect is the inelastic scattering of photons, in which the frequency and direction of the scattered light are different from the incident light. This phenomenon was first observed by Indian physicist Chandrasekhara Venkata Raman in 1928. Raman scattering occurs when a photon interacts with vibrating atoms in molecules or solids. The energy of the scattered photon is either less or greater than that of the incident photon, depending on whether the vibrational mode of the molecule or solid is excited (Stokes process) or de-excited (anti-Stokes process).

Raman scattering is a very weak phenomenon and is usually observed only when the sample is illuminated with intense monochromatic light, such as that from a laser. The scattered light is collected with a spectrometer, and the resulting Raman spectrum can be used to identify the chemical composition of the sample.

The following formula provides the differential cross-section for Raman scattering in crystals under nonresonant conditions [102]

$$\frac{d^2\sigma}{d\Omega d\omega} = \frac{\omega_s^4 V_{\text{prim}}}{c^4} \sum_j |\boldsymbol{g}_s \cdot \bar{\alpha}(j) \cdot \boldsymbol{g}_i|^2 \frac{\hbar}{2\omega_j}(n_j + 1)\delta(\omega - \omega_j), \tag{3.12}$$

where the frequencies of the incoming and dispersed light beams are denoted by ω_i, ω_s, and for the Stokes process $\omega_j = \omega_i - \omega_s \geqslant 0$, ω_j is the frequency of the j-th phonon mode. The light polarization vectors $\boldsymbol{g}_i$ and $\boldsymbol{g}_s$ are constrained to planes parallel to beam deflections by the light polarization vectors $\boldsymbol{k}_i$ and $\boldsymbol{k}_s$, respectively, such that $\boldsymbol{g}_i \cdot \boldsymbol{k}_i = 0$ and $\boldsymbol{g}_s \cdot \boldsymbol{k}_s = 0$. Equation (3.12) does not directly mention the

versors $\boldsymbol{k}_i$ and $\boldsymbol{k}_s$, but they must be supplied in order to determine the geometry of measurements and computations. The Bose factor of mode j is $n_j = (\exp(\frac{\hbar\omega_j}{k_B T}) - 1)^{-1}$, V_{prim} is the volume of a primitive unit cell, and c is the speed of light.

The Raman tensor $\bar{\alpha}(j)$ is a (3×3) matrix that is symmetric over two indices and it is related to the phonon mode j

$$\bar{\alpha}_{\alpha\beta}(j) = V_{\text{prim}} \sum_{\mu=1,2,\ldots r} \sum_{l=1,2,3} \frac{\partial \chi_{\alpha\beta}}{\partial u_l(\mu)} \frac{\varepsilon_{l,\mu}(\boldsymbol{k}=0,j)}{\sqrt{M_\mu}}, \tag{3.13}$$

where $\chi_{\alpha\beta}$ is the tensor of electric polarizability, directly connected with the tensor of the dielectric constant $\epsilon_{\alpha\beta}$ by the relation

$$\chi_{\alpha\beta} = \frac{1}{4\pi}(\epsilon_{\alpha\beta} - \delta_{\alpha\beta}), \tag{3.14}$$

and $u_l(\mu)$ is a measure of how far the μ atom is displaced in the direction of l. The change of the polarizability tensor with respect to atomic displacements is described by a 3-rank tensor $V[V^2]$. The Raman tensor is defined by phonon polarization vectors belonging to the Γ point, but for the LO modes may further depend on the orientation of the wave vector $\boldsymbol{k}$ pointing to Γ via the non-analitical term of the dynamical matrix, leading to different phonon polarization vectors $\varepsilon_{l,\mu}(\boldsymbol{k}=0,j)$. The Raman scattering cross section (3.12) is expressed in 10^{16} of atomic units. The elements of Raman tensor $\bar{\alpha}_{\alpha\beta}(j)$ are given in $\text{Å}^2/\sqrt{amu}$.

3.4 Thermodynamic functions

Thermodynamic functions are mathematical relationships that describe the energy, entropy, and other properties of materials as functions of its state. They are used to study the behavior of systems in thermodynamic equilibrium, meaning that the systems are in a state of balance and have reached the state of minimum of free energy. They are important quantities for predicting the behavior of crystals and for understanding the underlying physical and chemical processes that govern their behavior. Thermodynamical properties of crystals are directly connected with their lattice dynamics. The vibrational thermodynamic functions, presented below, can be obtained in the harmonic approximation from the phonon frequencies calculated within the direct method.

Internal energy

Internal energy, denoted by E_{ph}, is a thermodynamic function that represents the vibrational part of the total energy of a system. The internal energy of a system is a

state function, meaning that it depends only on the current state of the system and not on the path taken to reach that state.

In the harmonic approximation, the internal energy E_{ph} of the entire crystal can be represented by

$$E_{\mathrm{ph}} = \frac{rN}{2} \int_0^\infty \hbar\omega \coth\left(\frac{\hbar\omega}{2k_B T}\right) g(\omega) d\omega, \tag{3.15}$$

where N is the total number of primitive unit cells in the crystal, r denotes the number of degrees of freedom within each primitive unit cell, $\hbar$ represents the Planck constant, k_{B} represents the Boltzmann constant, and T is the temperature.

Helmholtz free energy

Free energy is an important thermodynamic function, as it describes the ability of a system to do work. It is used in various thermodynamic calculations such as determining the feasibility of a chemical reaction, designing engines, and predicting the maximum work output of a system. The change in free energy of the system is related to the heat added to the system and the work done by the system. The relationship between these three quantities is given by the second law of thermodynamics, which states that the change in free energy of the system must be zero or negative for a process to occur.

The Helmholtz free energy F_{ph} of the whole crystal is given in harmonic approximation by the following formula

$$F_{\mathrm{ph}} = rk_{\mathrm{B}}TN \int_0^\infty \ln\left[2\sinh\left(\frac{\hbar\omega}{2k_B T}\right)\right] g(\omega) d\omega. \tag{3.16}$$

Entropy

Entropy, denoted by S, is a thermodynamic quantity that describes the disorder or randomness of a system. It is a measure of the number of possible microstates that a system can have given the macrostate it is in. The entropy of a system is a state function, meaning that it depends only on the current state of the system and not on the path taken to reach that state.

The second law of thermodynamics states that the entropy of a closed system will never decrease over time. This means that the disorder or randomness of a closed system will never decrease over time. Entropy is also related to the heat added to a system, the temperature, and the energy of the system.

The phonon entropy S_{ph} of the whole crystal is given in harmonic approximation by

$$S_{\mathrm{ph}} = rk_{\mathrm{B}}N \int_0^\infty \left\{ \frac{\hbar\omega}{2k_{\mathrm{B}}T} \left[\coth\left(\frac{\hbar\omega}{2k_{\mathrm{B}}T} \right) - 1 \right] - \ln\left[1 - \exp\left(-\frac{\hbar\omega}{k_{\mathrm{B}}T} \right) \right] \right\} g(\omega) d\omega. \quad (3.17)$$

Heat capacity

Heat capacity, often denoted by C_h, is a thermodynamic property that describes the amount of heat required to raise the temperature of a substance by a certain amount. Heat capacity can be classified into two types, constant volume heat capacity (C_v) and constant pressure heat capacity (C_p). C_v is the heat capacity when volume is constant and C_p is the heat capacity when pressure is constant. The difference between C_p and C_v is the amount of heat required to change the volume of the substance, which is related to the pressure-volume work. The phonon heat capacity $C_{\mathrm{h,ph}}$ of the whole crystal in harmonic approximation is described by:

$$C_{\mathrm{h,ph}} = rk_{\mathrm{B}}N \int_0^\infty \left(\frac{\hbar\omega}{k_{\mathrm{B}}T} \right)^2 \frac{\exp\left(\frac{\hbar\omega}{k_{\mathrm{B}}T} \right)}{\left[\exp\left(\frac{\hbar\omega}{k_{\mathrm{B}}T} \right) - 1 \right]^2} g(\omega) d\omega. \quad (3.18)$$

Thermal displacements

Thermal displacement is a measure of the change in the position of atoms or molecules in a material due to thermal energy. At any temperature, the thermal energy of a material is sufficient to cause the atoms or molecules to vibrate about their equilibrium positions. These vibrations can be modeled using the harmonic approximation, which assumes that the vibrations are small and can be described by a set of harmonic oscillators. The mean square displacements (MSD), which depend on directions in a crystal lattice, are given by the symmetric matrix

$$B_{il}(\mu) = \frac{\hbar r}{2M_\mu} \int_0^\infty \coth\left(\frac{\hbar\omega}{2k_{\mathrm{B}}T} \right) \frac{g_{il,\mu}(\omega)}{\omega} d\omega \quad (3.19)$$

The formula describes the relationship between the mean thermal displacement and the matrix of phonon density of states $g_{il,\mu}(\omega)$ of an atom μ given by Eq. (3.11).

3.5 Anharmonicity

Anharmonicity plays an important role in physical systems, since their behavior usually deviates from the harmonic oscillator approximation. It is responsible

for thermal expansion, finite phonon lifetimes, and a decrease in thermal conductivity due to phonon-phonon interactions. Anharmonicity affects the temperature dependence of elastic constants, lattice vibrations, and phase transitions. Accurate calculations of these phenomena require consideration of anharmonic terms in the potential energy.

Anharmonic methods are computational techniques used to study the behavior of a material's atoms or molecules when they are subject to forces beyond those of simple harmonic motion. These methods take into account the anharmonic potentials, or potential energy surfaces, of a material's atoms or molecules, which describe their interactions and the resulting distortions from equilibrium positions.

There are several anharmonic methods that have been developed, including:

- **Anharmonic perturbation theory** (APT) was the first analytical approach to study the effect of anharmonicity on the coherent scattering of thermal neutrons [103]. Including the cubic and quartic anharmonic terms leads to the broadening and shift of phonon peaks.

- **Quasiharmonic approximation** (QHA) is used to estimate the thermal properties of a material by assuming that the lattice vibrations depend on the crystal volume and can be approximated as harmonic at finite temperatures [104].

- **Temperature dependent effective potential** (TDEP) method considers the temperature dependence of the interatomic potential energy, which enables accurate calculations of phonon energies and thermal properties such as thermal expansion, specific heat, and thermal conductivity [94].

- **Self-consistent phonon** (SCPH) method is used to calculate the dynamical and thermal properties of a material by considering the anharmonic effects beyond the perturbation theory [105, 106].

- **Supercell method**, which uses the series of supercells with atomic displacements to calculate the positions and shapes of the anharmonic peaks [107].

- **Green-Kubo method**, which is used to calculate the thermal conductivity of a material by considering the anharmonic interactions between phonons [108].

In this particular study, the anharmonic calculations have been employed to investigate the properties of pyrophosphate materials. We use the methods that have been implemented within the ALAMODE program (TDEP, SCPH, APT), which specifically focuses on lattice dynamical and thermal properties.

3.5.1 Quasiharmonic approximation

The quasiharmonic approximation (QHA) is a computational approach to study the thermodynamic properties of a system based on its vibrational modes. It assumes that the displacements of atoms are small enough for the harmonic approximation to hold for each volume of the studied system. In other words, it assumes that the *only* source of anharmonicity in the system is the change in the shape of the potential energy due to the change of geometry (e.g. volume) of the system. One of the key applications of QHA is the determination of thermal expansion of crystals [109, 110, 111]. It allows researchers to predict how a material will expand or contract due to the changes of its temperature. Moreover, the method can accurately capture cases where a material exhibits negative thermal expansion [104, 112, 113, 114, 115], wherein the material contracts upon heating. QHA was also used to investigate the structural phase transitions and phase diagrams of materials [116, 117].

The computational approach employed in the QHA studies adopts a harmonic approximation to describe the vibrational behavior of the system. However, it takes into account the influence of volume variations on phonon frequencies. While the harmonic approximation leads to a constant set of phonon frequencies regardless of temperature, this method allows for the calculation of phonon frequencies as functions of a temperature-dependent volume. The fundamental formula used to compute the total Helmholtz free energy within QHA is as follows

$$F_{\mathrm{tot}}(T,V) = F_{\mathrm{el}}(T,V) + F_{\mathrm{ph}}(T,V) = E_0(V) - S_{\mathrm{el}}T + F_{\mathrm{ph}}(T,V), \tag{3.20}$$

where, the electronic part, $F_{\mathrm{el}}(T,V)$, accounts for the contribution of electronic degrees of freedom to the system's free energy at a given temperature T and volume V. In a basic approximation, typically used for semiconductors or insulators [111], only the ground state energy $E_0(V)$, obtained within the DFT calculations, is taken into account. For metals, the entropy of an electronic system S_{el} can be calculated from the Fermi-Dirac distribution of states close to the Fermi energy [118]. The phonon part $F_{\mathrm{ph}}(T,V)$ is given by Eq. (3.16), which describes the contribution of atomic vibrations to the Helmholtz free energy within the harmonic approximation.

The calculation procedure entails several steps. Firstly, a full optimization of the crystal structure, resulting in the ground state energy E_0 and volume V_0 is required. Subsequently, the structure is calculated for different volumes, both larger and smaller than V_0, with small incremental changes in volume (e.g., 1%). Following these calculations, the next step involves determining the total free energy of the material as a function of temperature and volume. This is achieved by evaluating F_{tot} at various temperatures for each volume considered. Finally, the equilibrium volumes

at different temperatures $V(T)$ are determined by obtaining the minima of $F_{\text{tot}}(T, V)$. The resulting data provides valuable information about the relationship between volume, temperature, and the overall thermodynamic stability of the material.

The thermal expansion coefficient $\alpha(T)$ complements this understanding as a material property that quantifies the relative change in size or volume of a substance in response to temperature variations and can be calculated using this formula

$$\alpha(T) = \frac{1}{V(T)} \left. \frac{dV}{dT} \right|_T . \tag{3.21}$$

By representing the rate of expansion or contraction with changing temperature, it provides a crucial metric for analyzing thermal behavior and predicting dimensional changes.

3.5.2 Temperature dependent effective potential

A precise and highly scalable approach was presented by Hellman *et al.* [119] for addressing the lattice dynamics of solids in non-harmonic regime. This method originally relied on first-principles molecular dynamics (MD) simulations and offers a reliable means to extract the most accurate potential energy surface, considering both harmonic and higher-order contributions, at finite temperatures. It is specifically designed to handle strongly anharmonic systems, where QHA may not be applicable. In the next works [94, 120], a comprehensive and precise approach for calculating anharmonic free energies, known as the temperature dependent effective potential (TDEP) method, was introduced. This method involves *ab initio* MD simulations, followed by construction of a model Hamiltonian that captures lattice dynamics. The TDEP method demonstrates the effectiveness within both *ab initio* and classical MD frameworks.

TDEP introduces a model Hamiltonian with potential energy described by Eq. (3.1), which is called the anharmonic lattice model (ALM) [121]. The interatomic force constants (IFC) serve as parameters for ALM, and they depend on the atomic species and crystal structure. When computing the harmonic IFC using the direct method, it is sufficient to displace a single atom from its equilibrium position and consider the resulting forces on the atoms. Similarly, this approach can be extended to calculate anharmonic IFC, where multiple atoms within the supercell are simultaneously displaced. The fundamental principle of this method involves determining IFC by the minimization of the force differences

$$\Delta \boldsymbol{F}^2 = \frac{1}{N_c} \sum_{c=1}^{N_c} \sum_{a=1}^{N_a} |\boldsymbol{F}_{c,a}^{DFT} - \boldsymbol{F}_{c,a}^{ALM}|^2 = \min, \tag{3.22}$$

where summations are over all atoms $a = (\boldsymbol{m}, \mu)$ and configurations of atomic displacements c. $\boldsymbol{F}_{c,a}^{DFT}$ are forces calculated directly using DFT or other methods and $\boldsymbol{F}_{c,a}^{ALM}$ are forces obtained from the model's potential energy. Both sets of forces are calculated using the HF theorem (3.3). ALM is characterized by two adjustable parameters. The first parameter, N_{max}, determines the truncation point of the series, while the second parameter, r_N, defines the radius within which the interacting atoms $(\boldsymbol{m}_1\alpha_1, ..., \boldsymbol{m}_N\alpha_N)$ are considered in the summation. The number of parameters grows rapidly with increasing values of r_N and N_{max}. The comprehensive information and technical documentation for this method can be found at the website dedicated to the TDEP implementation [122].

An alternative methodology aimed at enhancing the analysis of anharmonic properties in materials was introduced by Tadano *et al.* [121]. This paper presents a systematic approach for determining the anharmonic force constants of crystals. The approach utilizes the direct method technique, which involves extracting the anharmonic IFC from the trajectory obtained through high-temperature simulations of first-principles MD. Being implemented in the ALAMODE software [121, 123], this methodology provides a comprehensive framework for analyzing network anharmonicity and thermal properties. ALAMODE seamlessly integrates with external DFT packages such as VASP or Quantum ESPRESSO, allowing simple extraction of harmonic and anharmonic force constants from the DFT results.

3.5.3 Anharmonic perturbation theory

Anharmonic perturbation theory is a theoretical framework used to study the effects of anharmonicity on the properties of physical systems [103]. By treating anharmonic interactions as perturbations to the harmonic system, this approach enables the calculation of more accurate and realistic results for various dynamical properties, such as phonon frequencies and line widths.

The anharmonic perturbation theory, as elucidated by Tadano *et al.* [124, 125], can be combined with the TDEP and SCPH methods, providing a comprehensive approach for studying lattice dynamics on the base of DFT calculations. The Feynman diagrams were employed to illustrate the phonon-phonon interactions. Through this diagrammatic representation, the intricate processes involved in phonon interactions and the corresponding effects of cubic and quartic anharmonicity are effectively described and analyzed.

We must take into account the anharmonic components in order to characterize the intrinsic phonon scattering mechanisms and the temperature dependency of phonon frequencies. In cases where the anharmonic terms are considerably smaller

compared to the harmonic terms, we can consider them as a perturbation, denoted as H', to the non-interacting (i.e. harmonic) Hamiltonian H_0

$$H = H_0 + H' \approx H_0 + U_3 + U_4. \tag{3.23}$$

Fifth- and higher-order terms are usually not included, since their contributions are much smaller compared to cubic and quartic terms. We define $G_q(\omega)$ as the Green's function for one-phonon processes, while $G_q^0(\omega)$ represents the Green's function corresponding to the non-interacting system described by H_0. Subsequently, the Dyson equation can be written as

$$[G_q(\omega)]^{-1} = [G_q^0(\omega)]^{-1} - \Sigma_q(\omega), \tag{3.24}$$

where $\Sigma_q(\omega)$ denotes the anharmonic self-energy, which may be determined using a systematic diagrammatic approach. When the self-energy is small comparing to phonon energies, $\hbar\omega_q \gg |\Sigma_q(\omega_q)|$, the phonon quasiparticle model remains applicable. In this case, the phonon frequency shift Δ_q and the linewidth Γ_q can be simplified to

$$\Delta_q(\omega) = -\frac{1}{\hbar}\mathrm{Re}\Sigma_q(\omega), \tag{3.25}$$

$$\Gamma_q(\omega) = \frac{1}{\hbar}\mathrm{Im}\Sigma_q(\omega). \tag{3.26}$$

Using Eq. (3.26) the phonon lifetime can be calculated as $\tau_q = 1/(2\Gamma_q)$. With the application of Eq. (3.25) and (3.26), the phonon spectral function can be expressed utilizing the subsequent formulation

$$S_q(\omega) = -\frac{1}{\pi}\mathrm{Im}G_q(\omega) \propto \frac{4\Omega_q^2\Gamma_q(\omega)}{[\omega^2 - \Omega_q^2 - 2\Omega_q\Delta_q(\omega)]^2 + [2\Omega_q\Gamma_q(\omega)]^2}. \tag{3.27}$$

The spectral function describes the behavior of the system in the frequency domain and is of particular significance in a detailed analysis of phonon properties. It can also be directly compared with the phonon spectra measured by the inelastic neutron or X-ray scattering techniques.

3.5.4 Self-consistent phonon theory

Self-consistent phonon (SCPH) theory enables one to investigate the lattice vibrations including strong anharmonic effects in a non-perturbative way [105, 106, 124]. The calculation of the updated frequencies in the SCPH approach involves a correction procedure that takes into account the loop diagrams representing the fourth-order anharmonic terms obtained within the TDEP approach [125]. Therefore, this

correction is determined by an expression that incorporates the Fourier transforms of fourth-order force constants

$$\Omega_q^2 = \omega_q^2 + \sum_{q_1} \frac{\hbar\Phi(q;-q;q_1;-q_1)}{4\Omega_{q_1}} \Big[2n(\Omega_{q_1})+1\Big], \tag{3.28}$$

where ω_q are harmonic frequencies and $n(\omega) = 1/(e^{\beta\hbar\omega}-1)$ is the Bose-Einstein distribution function. This equation considers the processes involving four phonons characterized by wave vectors $(q;-q;q_1;-q_1)$. The renormalized phonon frequencies Ω_q are obtained within the self-consistent iterative procedure starting from the harmonic frequencies. Therefore, Eq. (3.28) includes the contributions from the higher-order loop diagrams in the calculations of the anharmonic self-energy. This approach can be applied also for unstable harmonic phonons ($\omega_q^2 < 0$), since the second term in Eq. (3.28) may renormalize them, giving a stable phonon modes ($\Omega_q^2 > 0$).

In the SCPH method, it is possible to compute a correction to the Helmholtz free energy using the following equation [123]

$$\Delta F_{\mathrm{scph}}(V,T) = -\frac{1}{8N}\sum_q \Big[\Omega_q^2(V,T) - \omega_q^2(V)\Big]\Big[2n(\Omega_q)+1\Big], \tag{3.29}$$

where N is a number of phonon wave vectors in the first Brillouin zone.

3.5.5 High efficiency configuration space sampling

The high efficiency configuration space sampling (HECSS) approach was invented by Jochym and Łażewski in 2021 [126]. The main motivation behind HECSS is to achieve thermal equilibrium within a system by selecting independent displacement configurations corresponding to thermodynamic ensemble at a given temperature. Such approach can replace computationally expensive MD simulations, often used to investigate systems at non-zero temperature [119, 127]. In order to obtain uncorrelated sampling of atomic displacements, only a small fraction of configurations generated by the MD trajectory is used, making this approach very inefficient.

HECSS is based on the equipartition theorem, which in its most general version states that a generalized virial for any phase space coordinate (i.e. generalized coordinate or momentum) is proportional to temperature, when averaged over the entire ensemble

$$\left\langle q_m \frac{\partial H}{\partial q_n} \right\rangle = \delta_{mn} k_{\mathrm{B}} T, \tag{3.30}$$

where q_n represents the generalized coordinate or momentum, H denotes the Hamiltonian, T is the temperature, and k_{B} the Boltzmann constant. Assuming the system exhibits ergodicity, the ensemble average can be substituted with a time average.

We can consider a single atomic displacement with a coordinate q, and express the position-dependent portion of the Hamiltonian as a Taylor's expansion with respect to q as follows

$$E_p(q) = \sum_{n=2}^{\infty} C_n q^n, \tag{3.31}$$

hence the remaining coordinates serve as generic functions of the expansion coefficients C_n. This is a specific single-coordinate expansion required by the equipartition theorem (3.30), which can be rewritten in the form

$$k_B T = \left\langle q \sum_{n=2}^{\infty} n C_n q^{n-1} \right\rangle = \sum_{n=2}^{\infty} n C_n \langle q^n \rangle \tag{3.32}$$

and if we divide both sides by 2 and write n as $(n-2)+2$, we get

$$\left\langle E_p(q) \right\rangle = \frac{k_B T}{2} - \sum_{n=3}^{\infty} \frac{n-2}{2} C_n \langle q^n \rangle. \tag{3.33}$$

This expression is analogous to the kinetic energy component of the virial theorem, but it includes an extra term resulting from the anharmonic portion of the potential. This additional term is determined by the third and higher central moments of the probability distribution of displacements. For the harmonic potential this term vanishes, and there is a simple formula for the average potential energy at a given temperature. In weakly anharmonic systems, the second term is usually much smaller than the first one, and can be neglected. For a general case, the main effect of this anharmonic term is to recalibrate the temperature of the system, not changing qualitatively the overall energy distribution, which is governed by the central limit theorem (see below).

The main goal of a new procedure is to generate a set of displacement configurations with the mean potential energy given by Eq. (3.33), neglecting the second term, and with properly distributed potential energies corresponding to thermal equilibrium. For this, we can apply the central limit theorem (CLT) stating that for independent random variables, the distribution of the sample mean tends to the normal distribution. Therefore, we expect that with the increasing number of atoms, the probability distribution of the potential energy will converge to the Gaussian function. Indeed, using the MD simulations, it was demonstrated that both the kinetic and potential energy show the normal distribution even for small number of degrees of freedom [126]. In HECSS, the samples of atomic displacements with the proper energy distribution is generated by the Metropolis-Hastings algorithm [128, 129]. It is initiated with the prior distribution of a similar shape to the target Gaussian distribution, and the variance of the distribution is adjusted by the tuning algorithm in each step of calculations [126].

Designed to create configurations that mimic systems with non-zero temperatures, the HECSS strategy provides an alternative approach to employing the MD simulations as generators of the samples. It shows promise in generating accurate configuration samples for systems in thermal equilibrium, allowing to study of anharmonic effects in crystalline solids. The HECSS method has been successfully used to study the lattice dynamics in the materials with chiral phonons [130], orbital ordering [131], the structural phase transition [132], and the negative thermal expansion [115].

Chapter 4

Copper pyrophosphate

4.1 Investigation of alpha phase of copper pyrophosphate

In this chapter, I present a comprehensive theoretical study on the structural, electronic, and dynamical properties of α-$Cu_2P_2O_7$, and compare the obtained results with the experimental data. These results were partly included in the article entitled *"Ab initio studies for characterization and identification of nanocrystalline copper pyrophosphate confined in mesoporous silica"* published in Nanotechnology [50].

4.1.1 Calculation details

The calculations presented in this study utilized the PAW method [76] and GGA proposed by Perdew *et al.* [133], which were implemented in the Vienna Ab initio Simulation Package (VASP) [79, 80]. The crystal structure was optimized within a $1 \times 1 \times 1$ unit cell that contains 44 atoms. To accurately sample the Brillouin zone, the integration in the k-point space was carried out using a $4 \times 4 \times 4$ Monkhorst-Pack mesh [77]. The cut-off energy of 500 eV was employed, ensuring that the calculations captured the relevant electronic interactions and achieved a desirable level of accuracy.

To investigate the behavior of the electronic bands, the electronic band structure was calculated specifically for the primitive cell, which consisted of 22 atoms. The calculations were carried out using an $8 \times 8 \times 4$ k-point grid, which ensured a comprehensive sampling of the reciprocal lattice.

Furthermore, an essential aspect of this study involved examining the stability of the magnetic ground state. To accomplish this, calculations were performed for the ferromagnetic (FM) and two antiferromagnetic (AFM) configurations. By consider-

ing these distinct magnetic arrangements, we can gain insights into the material's magnetic properties and determine the ground state of copper pyrophosphate.

The GGA+U method [134] was employed in this study to incorporate strong local electron interactions. The on-site Coulomb interaction is particularly prominent in localized orbitals such as d and f electrons, although it can also play a significant role in localized p orbitals. In this particular investigation, due to the lack of precise parameters for the compound under study, typical values were employed based on the characteristics of high-temperature superconductors composed of copper-oxide planes. For copper, a Coulomb parameter $U_d = 9$ eV and a Hund's exchange $J_d = 1$ eV were utilized. As for oxygen, a Coulomb parameter $U_p = 4$ eV and a Hund's exchange $J_p = 0.5$ eV were considered. The electronic structure obtained for these parameters will be compared with the results for smaller values of U.

To address the limitations of standard approximations in accurately capturing long-range dispersion interactions, we incorporated approximate van der Waals (vdW) forces during the crystal structure optimization process. To achieve this, we applied vdW corrections proposed by Grimme, specifically the D2 and D3 corrections [89, 90], as well as the corrections proposed by Tkatchenko and Scheffler (TS) [135]. The D2, D3, and TS vdW corrections were implemented into the computational framework provided by the VASP software [136, 137, 138]. By incorporating these corrections, we aimed to improve the treatment of dispersion interactions and enhance the accuracy of the crystal structure optimization. These corrections are particularly valuable for capturing the subtle yet significant forces associated with van der Waals interactions, which are typically not adequately accounted for by standard approximations.

The calculation of phonon dispersion relations and phonon density of states (PDOS) was performed using the direct method [92] in conjunction with the Phonon [139] and Alamode [121] software programs. To account for longer-range interactions, the computations were conducted within a larger supercell of dimensions $2 \times 2 \times 1$, containing a total of 176 atoms. To accommodate the increased size, the k-point grid was reduced to $2 \times 2 \times 2$. In order to obtain the force-constant matrix, each non-equivalent atom was individually displaced, and subsequently, the HF forces acting on all atoms were calculated. The phonon energies and polarization vectors were then determined through the exact diagonalization of the dynamical matrix. The LO-TO splitting, caused by the macroscopic polarization, was derived by utilizing the static dielectric tensor and Born effective charges in density functional perturbation theory [140]. For the determination of the Raman mode intensities, the differential cross-section for Raman scattering was calculated using Phonon [141].

Additionally, the present study comprehensively presents an in-depth examina-

tion of various thermodynamic functions, meticulously investigates the anharmonic properties, using the HECSS and TDEP methods, and sheds light on a captivating phenomenon known as negative thermal expansion.

4.1.2 Crystal structure and magnetic properties

The $Cu_2P_2O_7$ compound has a crystal structure characterized by the presence of pyrophosphate P_2O_7 groups. These groups arrange themselves in layers parallel to the (001) plane, as shown in Fig. 4.1. In the α phase, the unit cell contains two layers of these pyrophosphate groups.

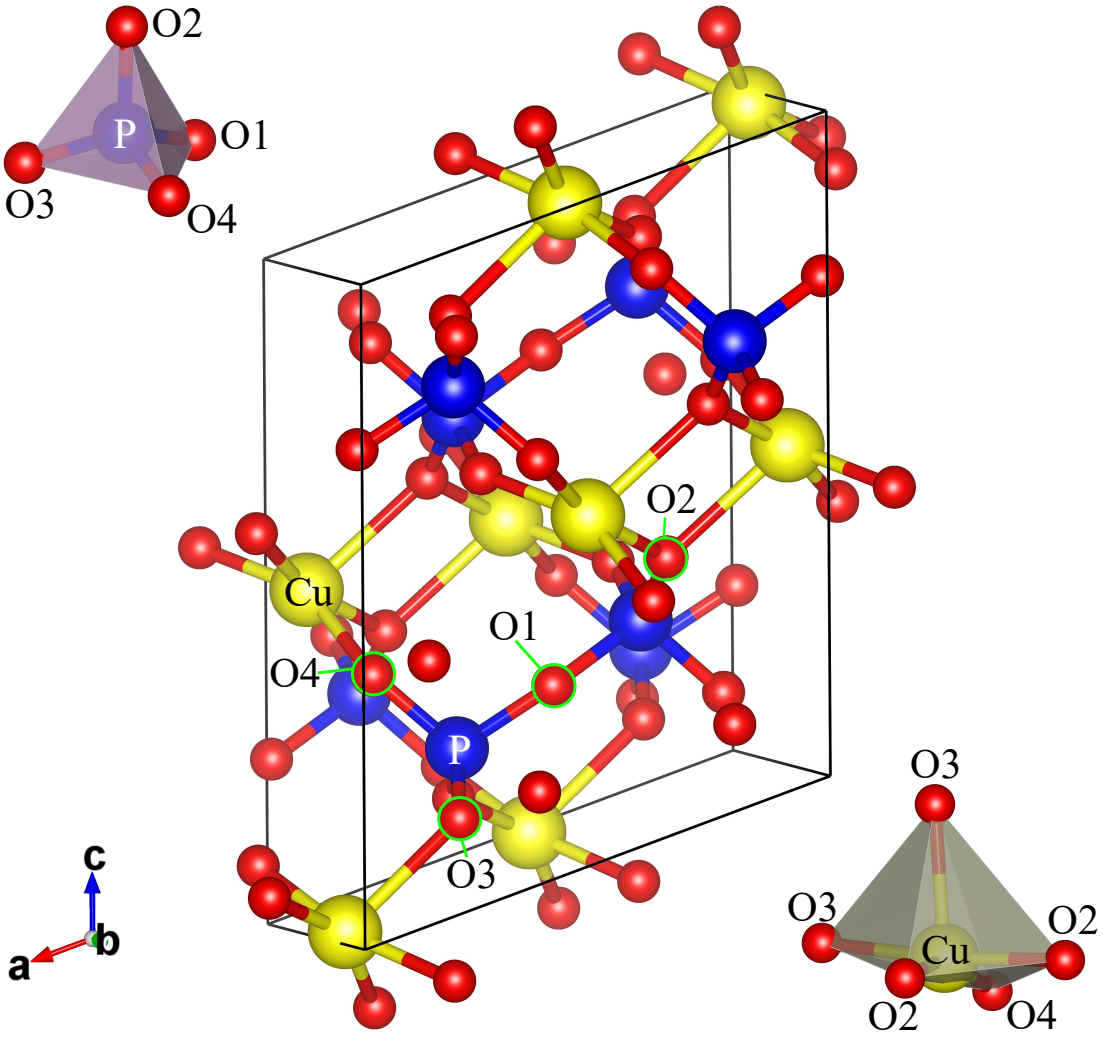

Fig. 4.1. Crystal structure of α-$Cu_2P_2O_7$. Copper, phosphorus, and oxygen ions are represented by yellow, blue, and red balls, respectively. The insets present the PO_4 and CuO_5 groups. The image was rendered using VESTA software [142].

The anion $[P_2O_7]^{4-}$ is composed of two $[PO_4]^{3-}$ tetrahedra that are connected

by sharing a common oxygen atom O1, referred to as the central oxygen atom. The relative angle between these tetrahedra and the lengths of the P-O bonds (both inner and outer) are considered as deviations from the fundamental $[PO_4]^{3-}$ structure, where phosphorus is bonded to four different oxygen atoms (see the inset in Fig. 4.1). The extension of orbitals over the central oxygen atom is influenced by the angle between the pair of tetrahedra, denoted as the P-O-P angle. For the observed value of this angle (157°), the bonding electrons of the central oxygen atom undergo sp^3 hybridization. This hybridization allows the formation of two bonds from the orbitals arranged in a tetrahedral manner, without the presence of any π bonds throughout the molecule. In addition, each copper atom is coordinated with five oxygen atoms, resulting in the formation of CuO_5 pentahedra, which are linked to each other by the shared O2-O2 and O3-O3 edges. They create the dimers, with the shortest Cu-Cu distance (along the b direction), within the (001) layers separated by the pyrophosphate groups. The Cu dimers are connected by the PO_4 units, sharing the common O2, O3, and O4 atoms, within the diagonal (101) planes that are joined by the O1 atoms (see Fig. 4.1).

The crystal structure of α-$Cu_2P_2O_7$ was optimized by using the experimental lattice parameters and atomic positions provided in Tab. 4.1 and 4.3, respectively, as the starting point. Initially, we performed calculations to compare the outcomes of the FM and two AFM arrangements. The magnetic moments on Cu^{2+} ions result from the $3d^9$ electronic configuration, corresponding to one hole with spin $\frac{1}{2}$ in the $d_{x^2-y^2}$ orbital [49]. The orientations of magnetic moments on the copper atoms in two AFM configurations are illustrated in Fig. 4.2. In the AFM1 configuration, the magnetic moments on the copper atoms within the same (100) planes align in parallel, and they have the same directions in the edge-sharing CuO_5 polyhedra (Cu-Cu dimers). In the other configuration (AFM2), the magnetic moments within the Cu-Cu dimers and between them have opposite directions. The AFM2 magnetic order is consistent with the experimental observations [47, 48] and the theoretical study on exchange couplings [49]. The direct magnetic exchange within the Cu-Cu dimers has the AFM character, however, it is reduced by the FM component of the superexchange coupling. The calculated exchange coupling constants between dimers, for different pairs of copper atoms, show the AFM behavior [49]. In our DFT calculations, the AFM2 arrangement shows the lowest energy, while the FM order has the higher energy than both AFM configurations (see Tab. 4.1). The lattice parameters exhibit some dependence on the magnetic order, with the c parameter showing a particularly significant increase in the AFM states. However, it should be noted that these calculated lattice parameters deviate significantly from the experimental values.

Tab. 4.1. The lattice constants a, b, and c, angle β, total energies, and magnetic moments obtained by different computational methods and compared with the experimental data.

	DFT			DFT+U			Exp. Data	
	FM	AFM1	AFM2	FM	AFM1	AFM2	Ref. [50]	Ref. [46]
a (Å)	7.2238	7.2173	7.2441	7.0901	7.0948	7.0968	6.9010	6.9070
b (Å)	8.2259	8.2119	8.2298	8.0961	8.0947	8.0958	8.1080	8.1300
c (Å)	8.7872	9.4285	9.4181	9.3527	9.3548	9.3543	9.1760	9.1810
β (deg)	111.75	111.14	111.97	109.65	109.29	111.19	109.65	109.61
E (eV)	-281.13	-281.19	-281.45	-199.64	-199.65	-199.67	–	–
m (μ_B)	0.554	0.610	0.580	0.840	0.838	0.836	–	1.89 [49]

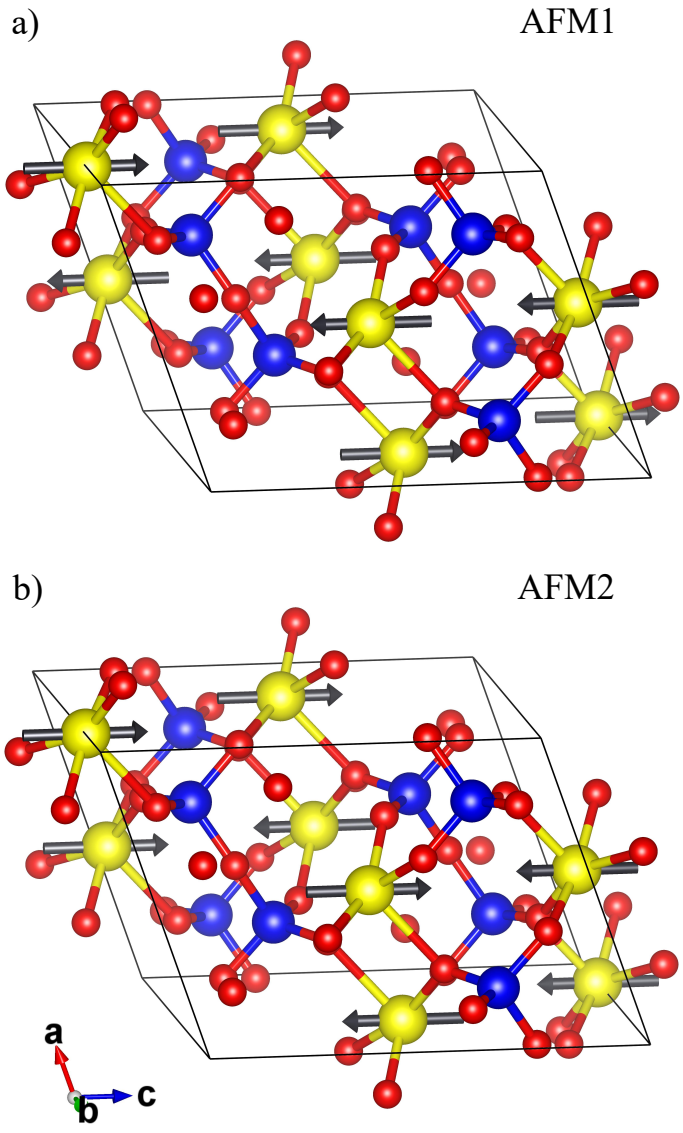

Fig. 4.2. Representation of magnetic moments on the copper atoms of α-$Cu_2P_2O_7$ for a) AFM1 configuration and b) AFM2 configuration.

Tab. 4.2. The lattice constants a, b, and c, angle β, total energies, and magnetic moments obtained by DFT+U method for AFM2 structure using different van der Waals corrections and compared with the experimental data.

	D2	D3	TS	Experimental Data	
				Ref. [50]	Ref. [46]
a (Å)	6.8892	6.9401	6.9752	6.9010	6.9070
b (Å)	8.1063	8.0853	8.0778	8.1080	8.1300
c (Å)	9.1510	9.2217	9.2213	9.1760	9.1810
β (deg)	109.52	110.05	110.21	109.65	109.61
E (eV)	-206.7048	-206.2576	-205.7880	–	–

In order to achieve improved consistency, we employed the DFT+U method in the second step of our analysis. The calculations conducted using this approach once again demonstrated a lower ground state energy for the AFM2 order, however, the differences between energies of different magnetic configurations are smaller than in the DFT calculations. We can notice that all lattice constants are reduced in the DFT+U calculations and they exhibit an improved agreement with the experimental data. As anticipated, the incorporation of the interaction term U lead to the Mott insulating state with the increased magnetic moments on the Cu atoms, slightly improving it when compared to the experimental value (as indicated in Tab. 4.1). One should notice that this value was estimated by fitting the magnetic susceptibility in the paramagnetic phase [49], and the direct measurements of magnetic moments in the order phase are not available. Our results agree very well with the hybrid-DFT calculations, which found the same ground state with the AFM2 order and similar magnetic moments ($m = 0.79\ \mu_B$) [143].

Moving forward with our analysis, we focused solely on the AFM2 order and proceeded with optimizing the crystal structure while considering various vdW corrections. This step allowed us to investigate the impact of these corrections on the overall crystal structure. Through the utilization of the D2, D3, and TS methods, we obtained three distinct sets of lattice parameters presented in Tab. 4.2. We found that all vdW corrections induce a further decrease of the a and c parameters leading to a very good agreement with the experimental data. It is related to the stronger bonding between the layers with the (001) and (100) orientation, due to the attractive vdW forces. The largest change is found for the parameter a (3%), indicating the strongest vdW interaction along this direction. The lattice parameter b is very weakly modified by dispersive interactions but it is very close to the experimental value. We see also that the total energies are lowered because of the negative values of the vdW

Tab. 4.3. Atomic positions in copper pyrophosphate monoclinic $C2/c$ structure as obtained in the DFT+U calculation with the vdW correction (D2), compared with the experimental data.

	experimental data (Ref. [50])			theoretical data		
Atom	x	y	z	x	y	z
O1	0.22080	0.15590	0.11280	0.22414	0.15624	0.11169
O2	0.32150	0.34920	0.38210	0.32731	0.34831	0.38319
O3	0.37570	0.00020	0.36140	0.37647	0.99872	0.36126
O4	0.00000	0.04660	0.25000	0.00000	0.04962	0.25000
P	0.19754	0.00750	0.20566	0.19774	0.00768	0.20503
Cu	0.48186	0.18712	0.00706	0.47748	0.18665	0.00899

corrections (see Sec. 2.4), however, they were calculated using different methods and cannot be compared between each other.

Upon analysis, it was determined that the D2 method exhibits the best compatibility with the diffraction data [46, 50], which are showed in Tab. 4.2. Furthermore, the atomic positions acquired through the implementation of the D2 correction exhibit a very good agreement with the experimental data, as illustrated in Tab. 4.3. Therefore, in the following investigations, we will use the crystal structure optimized with the D2 method. These findings highlight the significance of incorporating local Coulomb interactions and van vdW forces in the investigation of the crystal structure of $Cu_2P_2O_7$. The inclusion of these factors is essential for conducting accurate electronic structure and lattice dynamics studies on this compound.

4.1.3 Electronic properties

The electronic band structure, obtained using GGA, reveals an incorrect metallic state, in accordance with the previous studies conducted using the LDA method [49]. This outcome suggests that further investigations and improvements in the theoretical modeling are required to accurately capture the electronic properties of the system. In this research, we conducted calculations within the DFT+U method, employing different parameters for copper and oxygen atoms. The primary objective of these computations was to gain insights into the electronic properties of the copper pyrophosphate structure, as depicted in Fig. 4.3. The first panel (a) displays the electronic density of states obtained solely with the DFT method, revealing a weak metallic state due to the non-vanishing electronic states at the Fermi energy. In the panel (b), we present the results obtained for the parameters $U_d = 4$ eV, $J_d = 1.$ eV

for the Cu($3d$) states and $U_p = 2$ eV, $J_p = 0.5$ eV for the O($2p$) states. Here, we found the insulating state with the electronic band gap $E_g = 1.66$ eV. However, it is worth noting that this band gap is relatively small when compared to the values reported for the hydrated copper pyrophosphate (2.34 eV) [144] and the copper pyrophosphate nanocrystals (3.76-3.80 eV) [145].

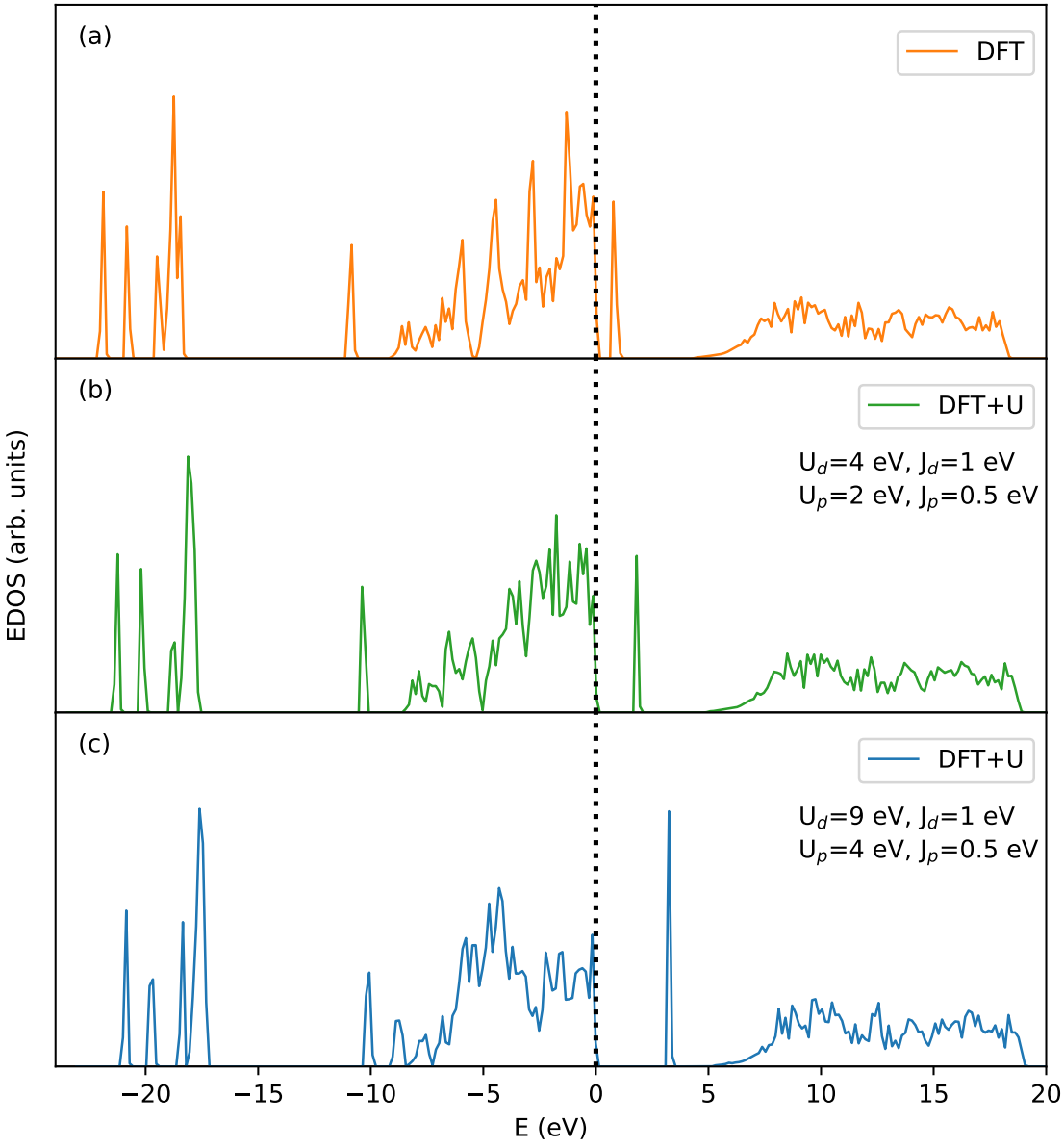

Fig. 4.3. Electronic densities of states in α-$Cu_2P_2O_7$ calculated by a) DFT method and b,c) DFT+U method. The Fermi level (dotted line) was set to zero.

In the pursuit of a more accurate description of the system, we applied the larger values of $U_d = 9$ eV and $U_p = 4$ eV, typically used for the superconducting cuprates [146]. As a result, we obtained the electronic structure presented in the

panel (c), with the band gap of $E_g = 3.15$ eV, which is more consistent with the experimental results and the hybrid-DFT calculations (3.97 eV) [143]. For this set of U and J parameters, we obtained also a very good agreement with the experimental lattice parameters, as shown the analysis performed in the previous section.

These results demonstrate that the introduction of the local Coulomb interaction U has a significant impact on the electronic properties. Specifically, the presence of U leads to the opening of a gap in the electronic band structure. This observation indicates that the insulating ground state of $Cu_2P_2O_7$ belongs to the Mott insulator category. The band structure of $Cu_2P_2O_7$, calculated for the same parameters as in Fig. 4.3(c), is presented in Fig. 4.4. The energy gap, which very weakly depends on the wave vector, exists between the broad valence band with the width ~ 9 eV and the very narrow and flat conducting band. The maximum of the valence band is found at the Γ point but the position of the minimum of the first conduction band cannot be unambiguously determined.

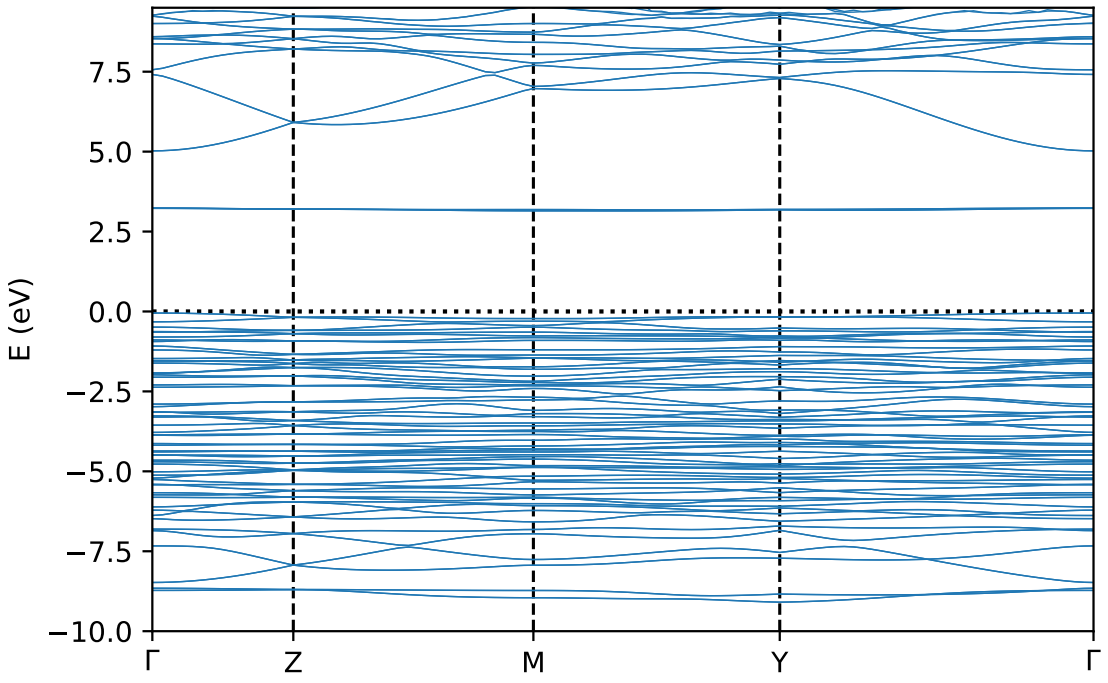

Fig. 4.4. Electronic band structure of α-$Cu_2P_2O_7$. The Fermi level (dotted line) was set to zero.

The occupations of electronic states with separate plots for the spin-up and spin-down components are depicted in Fig. 4.5. As a consequence of the AFM order, the total electronic density of states (DOS) remains identical for both spin components. The DOS analysis, with a focus on the majority spin-up states projected onto a single

Cu atom, reveals the presence of an exchange splitting in the 3d states. Contributions from both spin components can be observed within the energy range spanning from -8 eV to the Fermi energy (E_F). A prominent peak centered around -9 eV primarily consists of spin-up states, representing the lower Hubbard band. Notably, a gap of $E_g = 3.15$ eV emerges between occupied states featuring both spin components and the unoccupied spin-down 3d states, forming the upper Hubbard band. Between -10 eV and E_F, the Cu(3d) states exhibit hybridization with the O(2p) states, which dominate in the range of energies close to E_F. The O(2s) states are localized within the energy range of -22 to -17 eV, and a small contribution from oxygen s and p states is observed in the empty bands above the forbidden gap. Furthermore, the 3p states of the phosphorus atoms are occupied within the energy range of -11 eV to E_F, with an additional peak observed around -11 eV. The narrow bands below -17 eV are primarily occupied by the P(3s) states.

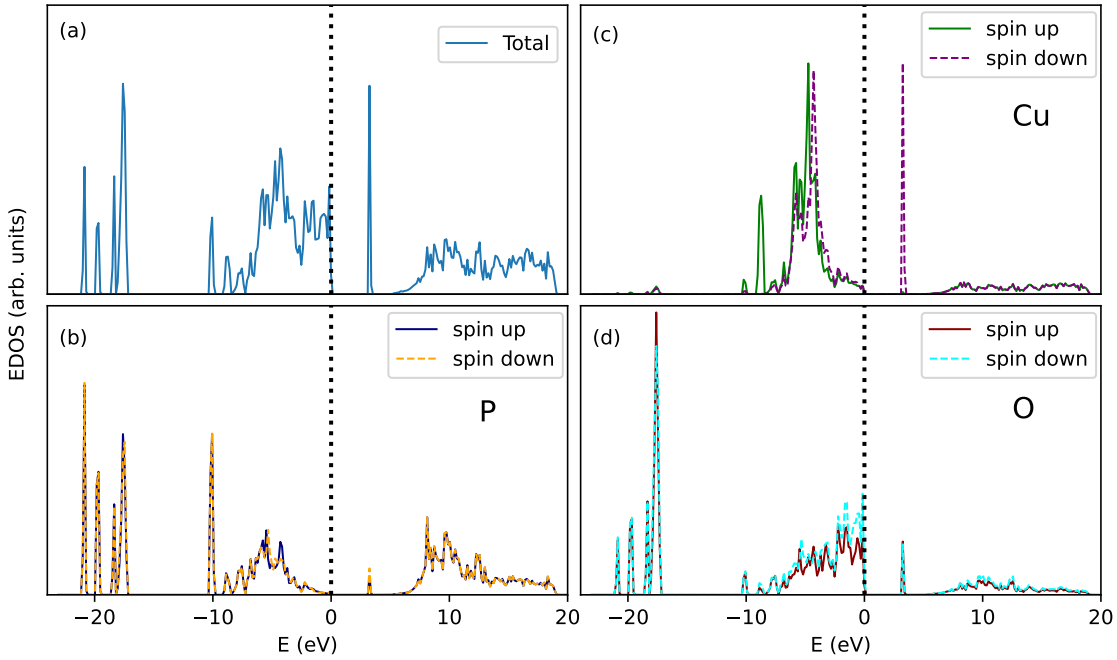

Fig. 4.5. a) The total and element-selected partial electronic densities of states: b) Cu, c) P and d) O, calculated for the spin-up and spin down electrons in the copper pyrophosphate. The Fermi level (dashed line) was set to zero.

4.1.4 Phonon dispersions

Within this section, we delve into the examination of the lattice dynamics of the α phase of copper pyrophosphate. Fig. 4.6(a) depicts the phonon dispersion curves obtained within the harmonic approximation, offering insights into the distribution of

phonon energies throughout the Brillouin zone. The calculated phonon frequencies are all real, indicating the dynamical stability of the α phase at low temperatures. Close to the Γ point, we observe the LO-TO splitting of the infrared modes. The shift of the LO modes to higher frequencies depends on the direction in the Brillouin zone, due to the anisotropy of the electric polarization in the monoclinic structure.

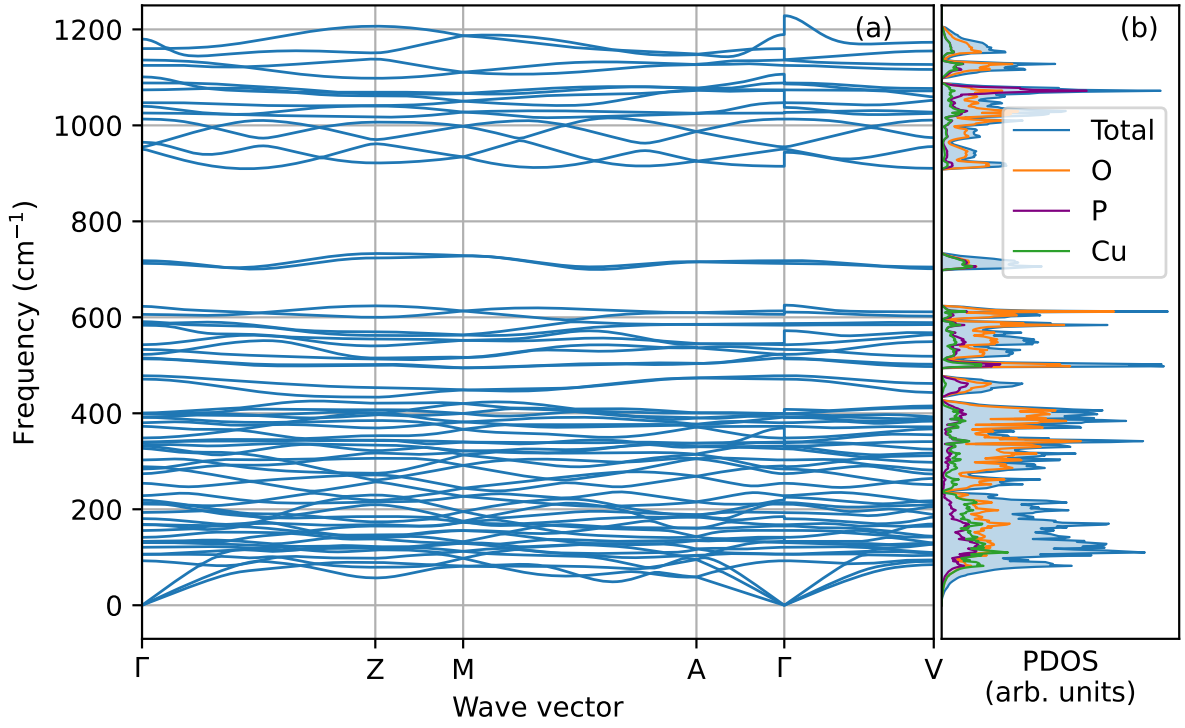

Fig. 4.6. a) The phonon dispersion relations and b) the total and partial element-projected PDOS in α-$Cu_2P_2O_7$.

In the right panel of Fig. 4.6, the total PDOS is presented, alongside the partial contributions of copper, oxygen, and phosphorus vibrations. The high-frequency range of the spectrum extends up to approximately 1200 cm^{-1}. Notably, the vibrations of P and O atoms predominantly contribute to the high-energy band spanning from 900 to 1200 cm^{-1}, which is clearly distinguished from the rest of the spectrum. In the middle part of the PDOS, three distinct bands can be observed. The narrow peak centered around 700 cm^{-1} corresponds to vibrations of all types of atoms. A broader band ranging from 500 to 600 cm^{-1} is primarily composed of vibrations of oxygen atoms, with a smaller contribution from phosphorus and copper atoms. In a separate peak around 400 cm^{-1}, the vibrational modes of oxygen atoms prevail. The low-energy region of the spectrum, ranging from 0 to 400 cm^{-1}, encompasses vibrations of all atoms, with copper and oxygen atoms making the dominant contributions, par-

ticularly below 200 cm^{-1}. Overall, the phonon spectrum provides valuable insights into the vibrational behavior of the different atomic species present in the α phase of copper pyrophosphate.

4.1.5 Raman scattering

The phonon frequencies computed at the Γ point and their associated activities are shown in Tab. 4.4. Using group theory, we can categorize all phonon modes at the zone center into 3 acoustic and 63 optical modes based on one-dimensional irreducible representations

$$\Gamma = 16A_g(\mathrm{R}) + 17B_g(\mathrm{R}) + 16A_u(\mathrm{I}) + 17B_u(\mathrm{I}). \tag{4.1}$$

Here, the labels R and I represent the Raman and infrared modes, respectively. By analyzing the polarization vectors and the nature of vibrations (as detailed in Tab. 4.4), the Raman modes were assigned accordingly. Comparing our findings with the experimental frequencies measured in the previous study by Pogorzelec *et al.* [46], we observe a good agreement between the two sets of results.

The comparison between the theoretical Raman spectrum and the spectroscopic measurement is depicted in Fig. 4.7. It is important to note that the copper pyrophosphate nanocrystals were embedded within the silica mesopores, which significantly impacts the resulting spectrum. The observed spectrum comprises distinct contributions that require careful analysis for accurate interpretation, considering the complex nature of the vibrational modes.

A considerable portion of the spectrum can be attributed to various factors:

- The vibration of the silica network's structural deformation and the presence of point defects, such as E′ centers, NBOHC, or neutral oxygen-deficient centers, which occupy the frequency range of 150-350 cm^{-1} [147, 148, 149].
- Symmetric bands originating from the O-Si-O bending vibrations within n-membered rings, where n is greater than 4. This spectral region spans 350-470 cm^{-1} [150].
- Contributions from O-Si-O bending vibrations within both four- and three tetrahedra-membered rings, which are evident in the range of 470-650 cm^{-1}.

These factors collectively contribute to the complexity of the spectrum, making it challenging to unambiguously attribute specific bands to copper pyrophosphate vibrations. The intricate interplay between silica-related vibrations and those originating from copper pyrophosphate demands careful analysis to distinguish between the two.

In light of these challenges, it becomes essential to employ advanced analytical techniques and theoretical models to disentangle the contributions from copper pyrophosphate and silica. Additional experimental investigations and sophisticated simulations could provide valuable insights into the vibrational behavior and the distinct spectral features of copper pyrophosphate nanocrystals within the silica mesopores.

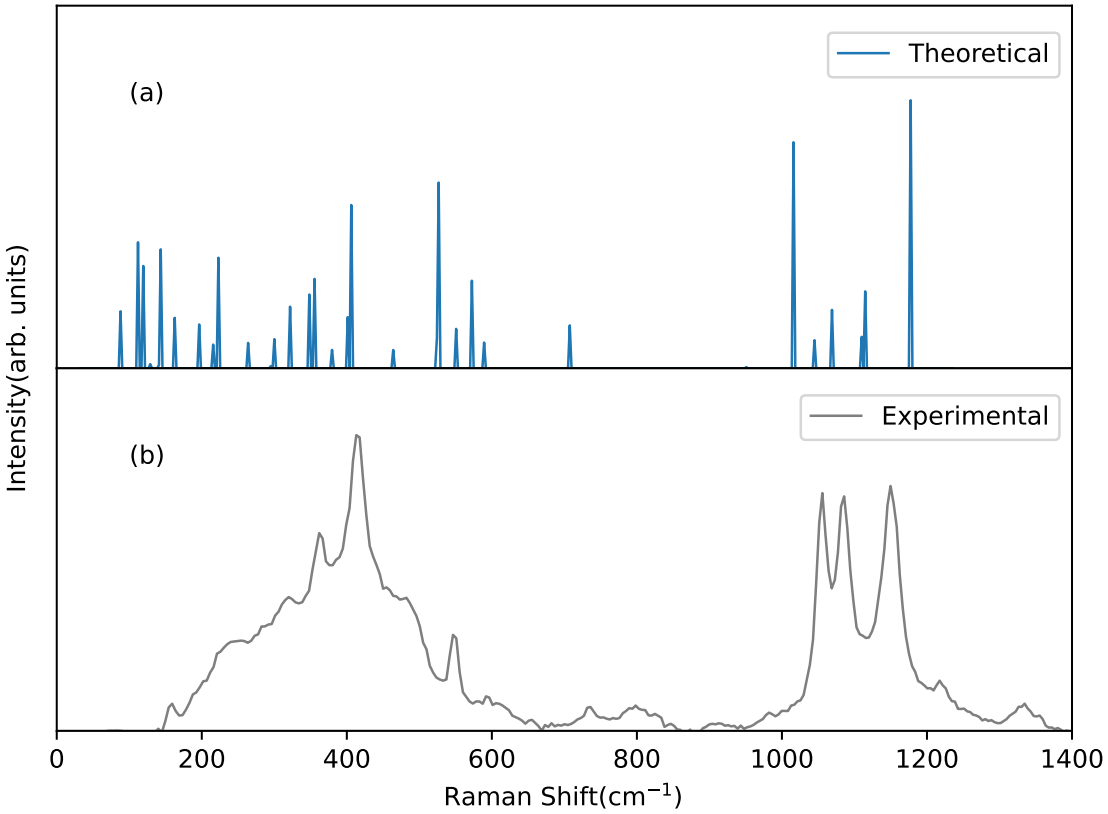

Fig. 4.7. Raman spectra of the copper phyrophosphate obtained experimentally on the nanocrystals embedded inside the SBA-15 silica pores (b) and calculated for the bulk crystal (a).

In this context, a valuable approach involves establishing a band correlation between the experimental and theoretical Raman data by carefully comparing both spectra. Through this procedure, the theoretical Raman data provide essential insights into the nature of the observed experimental bands.

According to the analysis, the theoretical Raman data suggest that the experimental bands located below 170 cm^{-1} can be attributed to the collective motion of atoms in the crystal lattice, contributing to low-frequency spectral features. The bands falling within the range of 200-450 cm^{-1} are identified to originate from the bending, twisting, and rocking modes of the $O - PO_3$ groups. This specific region

of the spectrum reflects the vibrational behavior of these molecular units within the crystal structure.

Notably, two distinct and well-visible bands with maxima around 360 and 414 cm^{-1} exhibit a very good agreement with the corresponding theoretical values of 354 and 404 cm^{-1}. This consistency between the experimental and theoretical peaks further strengthens the reliability of the theoretical model in describing the vibrational modes in this system. The band at 549 cm^{-1} shows a strong correlation with the most intense theoretical peak situated at 527 cm^{-1}. This peak has been identified as the wagging symmetrical mode of the PO_3 group. Additionally, the positions of the dominant bands align well with the data previously reported for the $Cu_2P_2O_7$ crystal [46]. Raman bands around 700 cm^{-1} arise from the symmetrical stretching vibrations of the P-O-P bridges, and their agreement with the corresponding theoretical data provided in Tab. 4.4 is notable. However, it's essential to highlight that all the aforementioned experimental bands, including other weaker bands predicted by theory, remain affected by silica-related contributions. Consequently, caution must be exercised in definitively attributing these bands to copper pyrophosphate vibrations.

The analysis of copper vibrations presents even more challenges. According to the theoretical predictions, the Cu-O stretching motions should manifest as bands centered in the range of 100-300 cm^{-1} [151]. The strongest signal in the partial density of states (see Fig. 4.21) indicates that Cu vibrations are most prominent below 200 cm^{-1}. However, the higher frequency range of Cu-O modes overlaps with Si-O modes, which are characteristic of the silica matrix (as mentioned earlier). Moreover, due to the octahedral copper occupation, the Cu-O modes exhibit relatively weak intensities in Raman spectroscopy. Taking into account the experimental limitations related to the detector, which prevents the collection of reliable signals below 200 cm^{-1}, unambiguously ascribing Cu-O modes to individual experimental bands becomes exceedingly difficult. Consequently, a more precise discussion of this type of vibration was not possible, and the corresponding information was also excluded from Tab. 4.4.

Due to the aforementioned challenges, our focus has shifted to the region above 850 cm^{-1}, which appears more promising for our analysis. Despite the typical presence of silicon-oxygen tetrahedral Q^n (n = 0-4, representing the number of bridging oxygen per SiO_4 tetrahedron) vibrational modes within this range (850-1250 cm^{-1}), these bands are generally weak or very weak. Fortunately, the signals related to the crystalline components are stronger, providing a clearer basis for investigation.

In this higher frequency range, we have identified three prominent experimental bands with similar intensities centered at 1055, 1085, and 1150 cm^{-1}. Remarkably,

Tab. 4.4. Frequencies, irreducible representations (IR), activities (A) (I -Infrared, R-Raman), and assignments of the phonon modes at the Γ point in $Cu_2P_2O_7$. The phonon modes are assigned using the symbols: ν - stretching, δ - in-plane bending, ω - wagging, τ - twisting, ρ - rocking; with indexes: s - symmetrical, a - anti-symmetrical. The experimental frequencies of Raman modes are taken from Ref. [46].

Frequency		IR (A)	Assignment	Frequency		IR (A)	Assignment
Theory	Exp.			Theory	Exp.		
0		A_u(I)	-	392.438		B_u(I)	-
0		B_u(I)	-	395.774		A_u(I)	-
0		B_u(I)	-	402.345		B_g(R)	$\tau_a(O-PO_3)$
87.059	105	A_g(R)	$\rho_s(PO_3)$	404.947	412	A_g(R)	$\tau_s(O-PO_3)$
95.565		A_u(I)	-	414.053		B_u(I)	-
109.175		B_u(I)	-	464.688	475	A_g(R)	$\tau_s(O-PO_3)$
111.543		B_g(R)	$\rho_a(PO_3)$	472.660		A_u(I)	-
111.977		A_u(I)	-	505.183		B_u(I)	-
118.615	121	A_g(R)	$\rho_s(PO_3)$	508.985		A_u(I)	-
127.788		B_g(R)	$\rho_a(PO_3)$	523.362		B_g(R)	$\omega_a(PO_3)$
139.963	135	B_g(R)	$\rho_a(PO_3)$	526.931		B_u(I)	-
143.933	141	A_g(R)	$\rho_s(PO_3)$	527.498	544	A_g(R)	$\omega_s(PO_3)$
159.910		B_u(I)	-	549.947		B_g(R)	$\omega_a(PO_3)$
163.813	160	B_g(R)	$\rho_a(O-PO_3)$	573.630		B_g(R)	$\omega_a(O-PO_3)$
165,881		B_u(I)	-	590.175	590	A_g(R)	$\omega_a(O-PO_3)$
197,470		B_g(R)	$\rho_a(O-PO_3)$	591.843		A_u(I)	-
212.480		A_u(I)	-	599.114		B_u(I)	-
215.048	214	A_g(R)	$\rho_s(O-PO_3)$	707.990	730	A_g(R)	$\nu_s(P-O-P)$
218.118		A_u(I)	-	709.491		A_u(I)	-
223.655	219	B_g(R)	$\rho_a(O-PO_3)$	913.465		B_u(I)	-
252.475		A_u(I)	-	950.224	975	B_g(R)	$\nu_a(P-O-P)$
263.849		B_g(R)	$\rho_a(O-PO_3)$	960.231		A_u(I)	-
276.758		B_u(I)	-	1012.300		B_u(I)	-
294.237	282	B_g(R)	$\rho_a(O-PO_3)$	1016.637	1050	A_g(R)	$\nu_s(PO_3)$
299.440		A_g(R)	$\tau_s(PO_3)$	1029.946		A_u(I)	-
309.747		B_u(I)	-	1044.356		A_g(R)	$\nu_s(PO_3)$
321.589	320	A_g(R)	$\tau_s(PO_3)$	1063.236		B_u(I)	-
341.937		A_u(I)	-	1068.072		B_g(R)	$\nu_a(O-PO_3)$
346.106		B_u(I)	-	1109.001	1080	B_g(R)	$\nu_a(PO_3)$
347.274		B_g(R)	$\delta_a(O-PO_3)$	1114.738		A_g(R)	$\nu_s(PO)$
354.845	360	A_g(R)	$\delta_s(O-PO_3)$	1121.443		A_u(I)	-
378.495		A_u(I)	-	1130.182		B_u(I)	-
380.163		B_g(R)	$\delta_a(O-PO_3)$	1178.082	1146	B_g(R)	$\nu_a(PO_3)$

these frequencies align well with the data reported previously for the α-phase [46]. While the theoretical Raman spectrum shows some minor differences from the experimental data, it still offers valuable insights. Specifically, two predicted bands with strong maxima at 1016 and 1178 cm^{-1} exhibit good agreement with the experiment. As a result, we confidently correlate these bands with the symmetrical A_g mode and anti-symmetrical B_g mode of the terminal PO_3 groups, as listed in Tab. 4.4.

However, the third band centered at 1085 cm^{-1} exhibits significantly greater intensity compared to the theoretical data and the spectrum reported in Ref. [46]. Consequently, its unambiguous interpretation poses challenges. Despite this discrepancy, considering the presence of theoretically predicted bands around this frequency range, we propose assigning this band to symmetrical stretching modes of the terminal PO_3 groups.

Certain disparities observed when comparing the experimental and theoretical data can be attributed to various factors, including the approximations used in the theoretical calculations and specific conditions during the experiment. Notably, the theoretical approach typically assumes an ideal crystal structure devoid of defects, while the real material studied in the experiment contains essential structural imperfections. These defects can significantly influence the positions, widths, and intensities of the bands observed in the Raman spectrum.

Another critical consideration is the crystallization of copper pyrophosphate crystals within the confined space of small hexagonal silica pores, as evident in the TEM images (see Appendix). Interestingly, although the crystal structure parameters are only slightly different from those of a typical bulk system, additional factors such as geometry restriction and surface effects may play a crucial role in dictating the crystallization direction within the silica pores. Consequently, modifications in the crystal geometry near the silica pore and finite-size effects contribute to variations in the arrangement of Raman bands. These effects become particularly pronounced when comparing nanocrystals that crystallize within the pore with bulk data [46], offering valuable insights into the differences observed in the bands' intensity between the theoretical predictions and experimental results.

Despite these challenges, it is essential to highlight that the theoretical Raman data still exhibit good correlation with the experimental data and continue to provide valuable information about the nature of individual bands observed in the Raman spectrum. By considering the interplay of theoretical approximations, structural defects, and confinement effects within the silica pores, we gain a deeper understanding of the material's vibrational behavior and enhance the interpretation of experimental results.

In conclusion, while some discrepancies persist, the overall correlation between theoretical and experimental Raman data allows us to glean important insights into the material's vibrational properties. The careful consideration of theoretical approximations and experimental conditions remains vital in our pursuit of a comprehensive understanding of this complex system.

4.1.6 Anharmonic properties

In our current study, to investigate the anharmonic properties for α-$Cu_2P_2O_7$ we initially generate atomic displacements for three distinct temperatures utilizing the HECSS approach. For each set of displacements the total energy and HF forces acting on all atoms are calculated using VASP. Subsequently, employing ALAMODE, we create a fitting file and proceed with potential and phonon calculations for the given temperatures. In order to generate atomic displacements, we employed an optimized supercell approach, incorporating a parameter of width (w) to describe the initial scale of the prior energy distribution. Additionally, we carefully selected a specified number of generated samples (N) and provided a temperature (T) in kelvins to guide this displacement process.

The atomic displacements of each individual sample must be generated based on a probability distribution, as described in Sec. 3.5.5. It is important to note that while the energy follows a normal distribution, the positions of individual atoms do not necessarily conform to the same distribution. However, when considering a large number of atoms, their average distribution tends to follow a normal distribution as well, just like the average energy distribution mentioned earlier. The overall probability of an individual atom's displacement in the crystal is the sum of all distributions that align with this particular displacement (shown in a Fig. 4.8).

The target distribution is achieved through a process of shaping the prior distribution by assigning weights to the samples. This algorithm accomplishes this objective by repeating samples with higher probabilities while skipping those with lower probabilities. Essentially, integer weights are assigned to all samples in the prior distribution to achieve this effect. The underlying concept is to calculate weights for any given prior distribution by adjusting its histogram. To further enhance the process, the implemented algorithm takes a step beyond and introduces non-uniform binning for the prior distribution, with one sample per bin. Desired weights are then computed to match the probabilities of the samples to the target distribution.

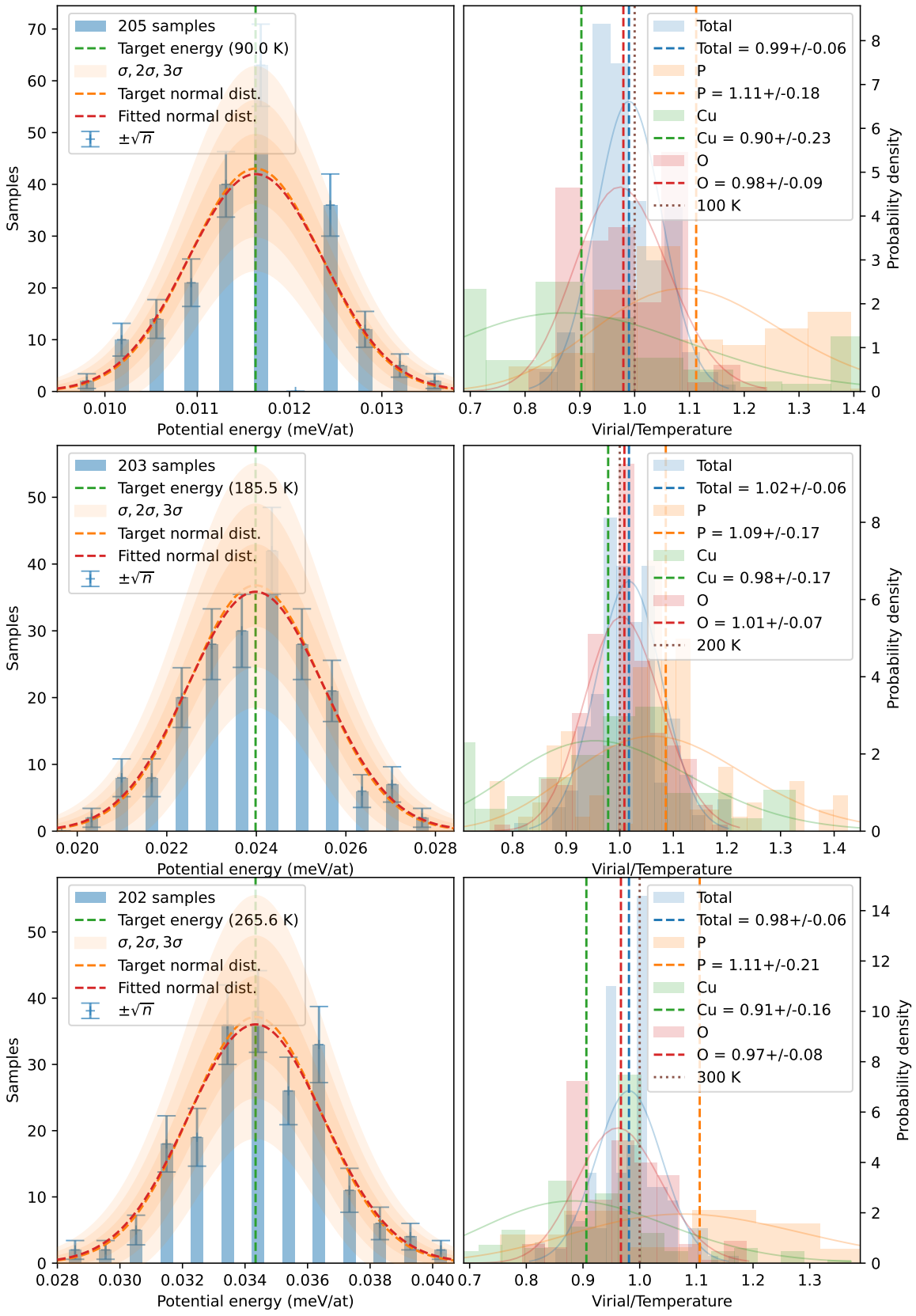

Fig. 4.8. Monitoring histograms for the configuration list (left side) and viral distribution in the sample (right side) for a given temperature.

The outcome of this procedure is a set of weights for the samples that realizes the target distribution. While in principle, this method is applicable to any prior and target distribution, it yields the best results when both distributions share a common support. This common support ensures that data generation is not attempted in empty regions by merely weighting data in other areas.

In our study, the chosen input parameters were as follows: the number of samples generated during the process $N = 50$, the width parameter used to shape the initial scale of the prior distribution $w = 2$, and the initial temperatures T =(100, 200, 300) K. These parameters were carefully selected to facilitate an effective and accurate sampling procedure in our specific case.

The sampling statistics plots (the left side of Fig. 4.8) provide valuable insights into the generated samples. The orange bell curve, accompanied by the green central line, represents the target potential energy distribution, which corresponds to the target temperature. In agreement with Eq. (3.33), the mean potential energy increases for the larger values of temperature, however, the target temperatures are different from the initial temperatures due to the approximations described in Sec. 3.5.5. The target energy distribution is encircled by shaded orange regions representing the σ, 2σ, and 3σ zones. In this context, σ indicates the standard deviations for the samples. The width of the standard deviation band is determined by scaling the square of the target distribution according to the sample's size and the number of bins in the histogram.

The blue-shaded bars in the plots correspond to the population within each histogram bin, while the red dashed curve illustrates a normal distribution fitted to the data points in the sample. In ideal cases, both the histogram bars and the fitted distribution should fit comfortably within the 3σ band, indicating a correct sampling of the target distribution. However, in situations where the sample size is small, statistical fluctuations become prominent, and the bars or the fitted distribution might exceed the 3σ band. In such instances, it is important to take into consideration the size of the variance of the actual histogram bins to assess the quality of the sampling.

The viral distribution plot, displayed on the right side of Fig. 4.8, presents a target energy calculated independently for each type of atom. The dotted brown line represents the given temperature for the samples, while the dashed blue, orange, green, and red lines illustrate the temperature shifts from the central position for all, P, Cu, and O atoms, respectively. These temperature shifts occur due to variations in the extra term in Eq. (3.33) resulting from the anharmonic portion of the potential.

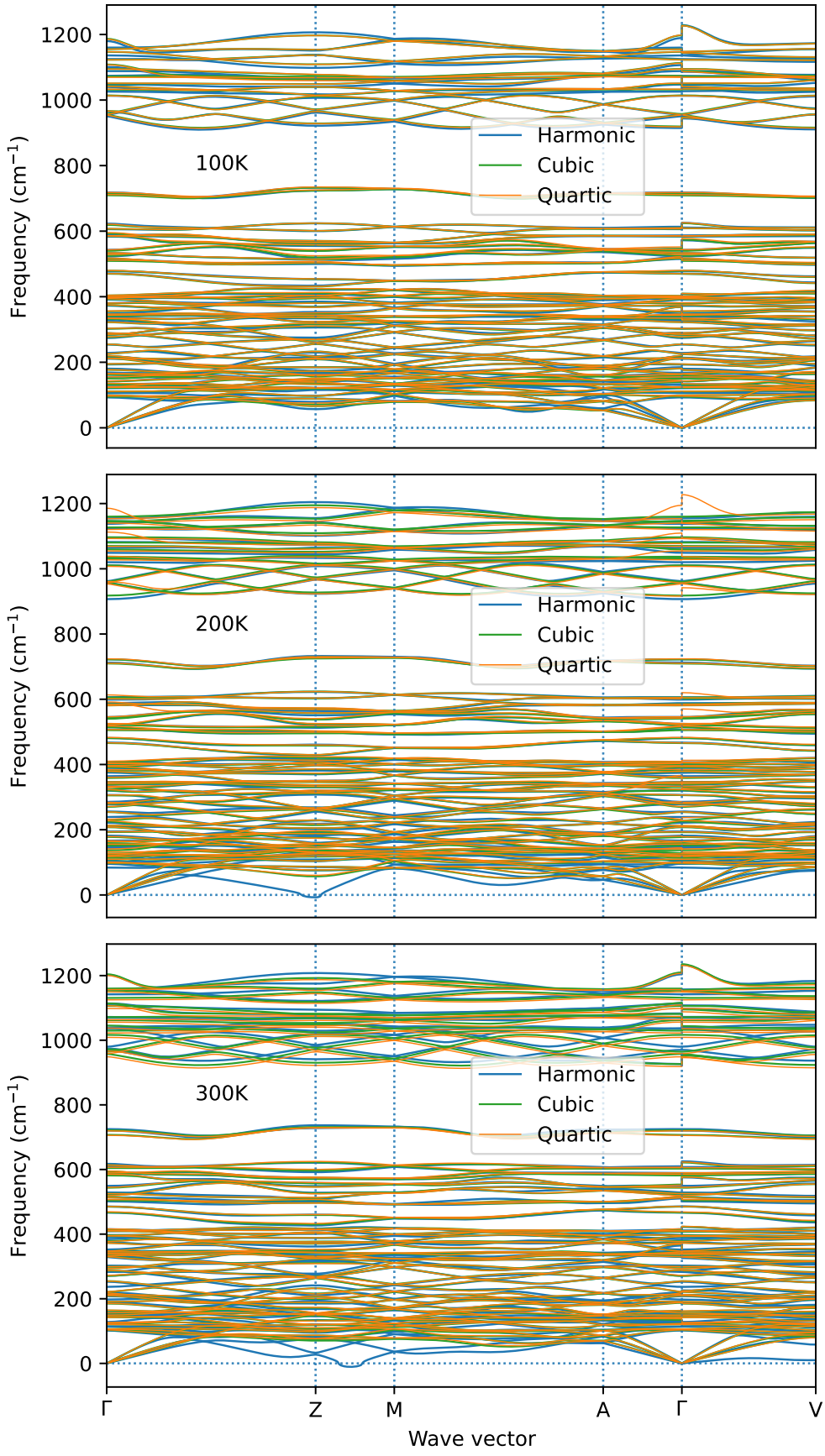

Fig. 4.9. Phonon dispersion relations obtained for α-$Cu_2P_2O_7$ within the harmonic approximation (blue line) and using the TDEP approach with cubic (green line) and quartic (orange line) anharmonic corrections.

Upon analyzing the acquired data from the sampling distribution and atomic virial distribution, we proceed to calculate the phonon dispersion curves for the previously mentioned temperatures, considering the harmonic approximation as well as the anharmonic corrections to the potential up to the cubic or quartic terms obtained within the TDEP approach.

By analyzing Fig. 4.9, we note that at the lowest temperature $T = 100$ K, the results for the harmonic and anharmonic potentials are almost identical, and the structure exhibits the dynamical stability. However, as the temperature increases, the lowest dispersion curves obtained within the harmonic approximation become softer, with a stronger effect observed at the higher temperature ($T = 300$ K), which is close to the phase transition temperature. Nonetheless, the inclusion of anharmonic corrections in the energy potential influences phonon frequencies and stabilizes the structure. It shows the import role of the anharmonic effects in stabilizing the structure of copper pyrophospate, what will be discussed in details in Chapter 4.3.

4.1.7 Thermodynamic functions

Thermodynamic properties play a pivotal role in understanding the behavior of physical systems. In our study we investigate thermodynamic phonon properties such as internal energy (Fig. 4.10), entropy (Fig. 4.11), Helmholtz free energy (Fig. 4.12), and heat capacity (Fig. 4.13). In each figure, we present the results obtained using the equations for the harmonic approximation discussed in Sec. 3.4. However, we will compare the results obtained both for the harmonic potential and the potential with anharmonic corrections up to the quartic terms calculated for three different temperatures $T = 100$, 200, 300 K.

The analysis of the four thermodynamic quantities through graphical representations reveals that, across all three temperatures, the differences between results obtained using harmonic and anharmonic potentials are relatively small. However, for the anharmonic calculation at $T = 100$ K, it is evident that the entropy, heat capacity, and internal energy exhibit a more pronounced increase with temperature compared to the harmonic potential. Examining the free energy, at low temperatures, the harmonic line decreases more rapidly, eventually converging with the anharmonic line towards the end. Moreover, when observing the anharmonic line for $T = 200$ K and 300 K in the entropy, a more substantial difference is noticeable compared to $T = 100$ K. Furthermore, for all three temperatures, the entropy displayed by the harmonic line grows faster than the corresponding anharmonic line. Additionally, in the free energy, the harmonic line decreases more rapidly than its anharmonic counterpart.

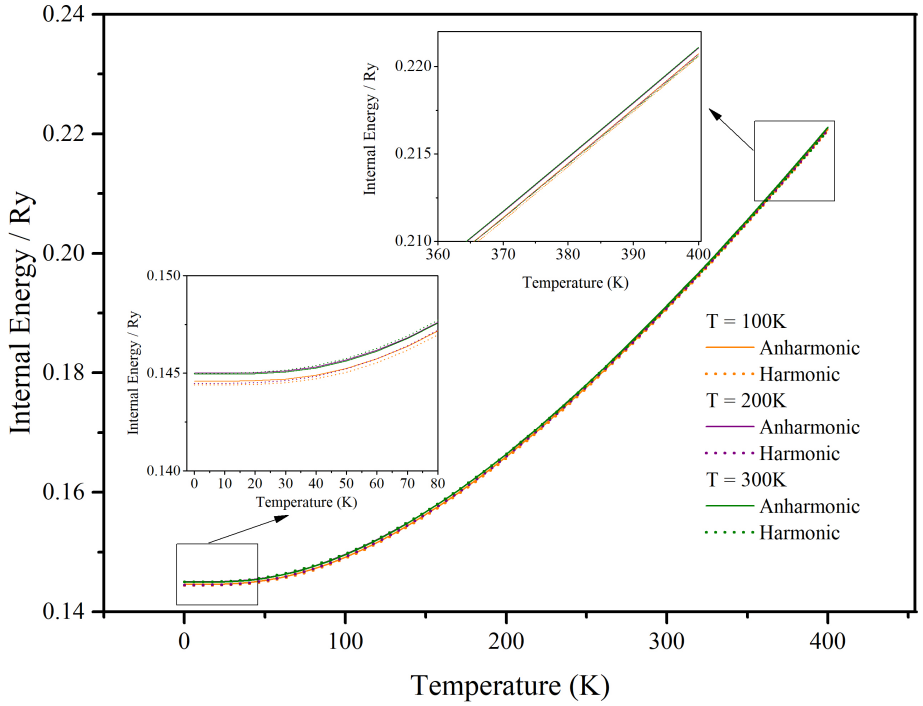

Fig. 4.10. The internal energy omputed for three basic temperatures using both harmonic and anharmonic potentials

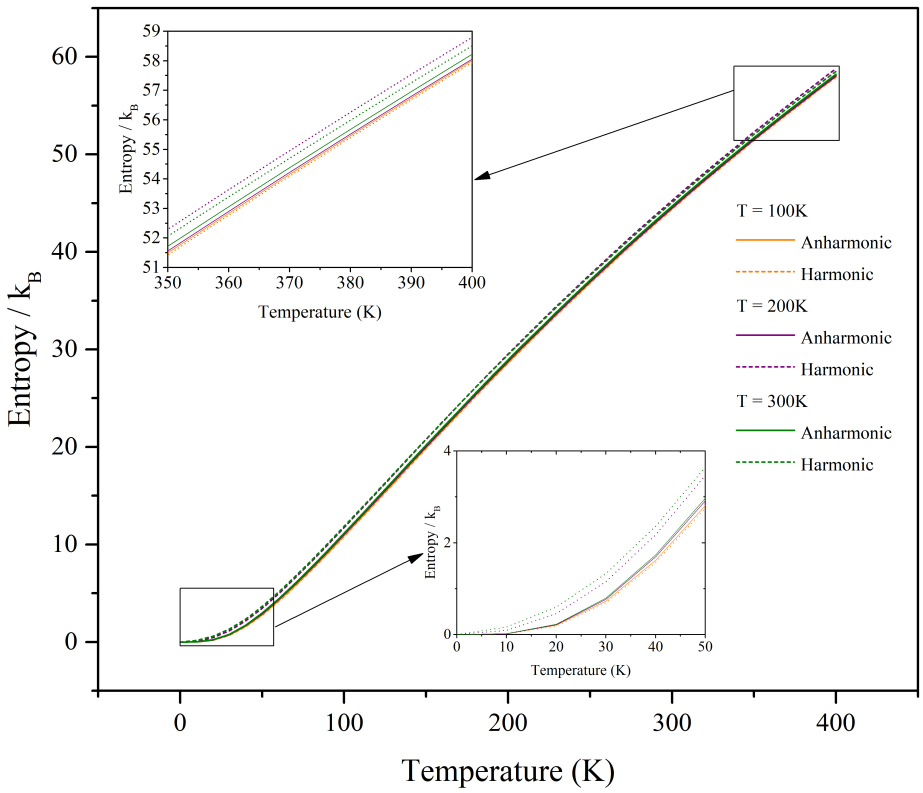

Fig. 4.11. Entropy as a function of temperature calculated for three basic temperatures by harmonic and anharmonic potentials.

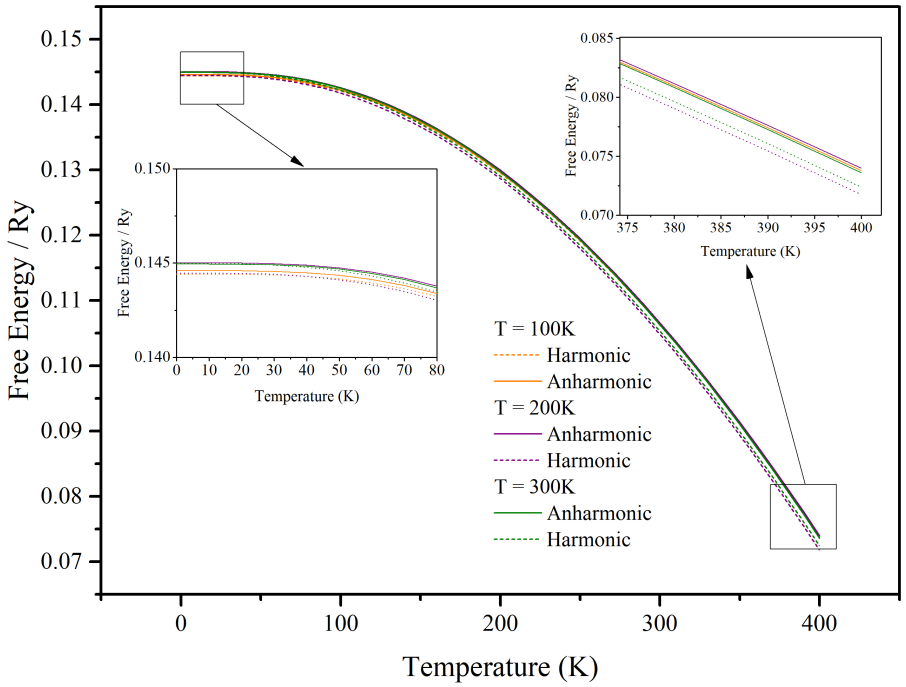

Fig. 4.12. The free energy computed for three basic temperatures using both harmonic and anharmonic potentials

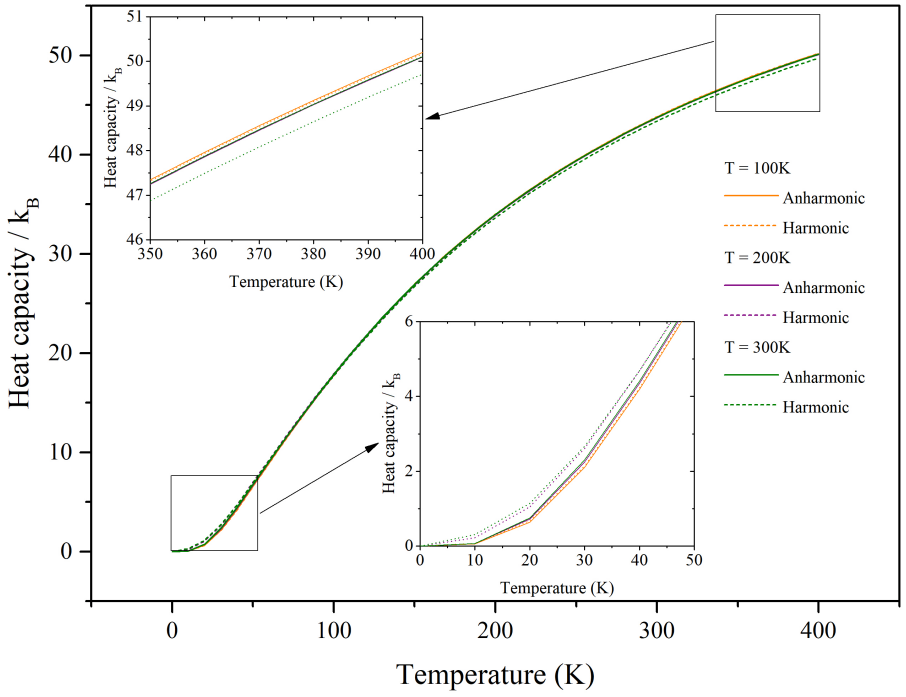

Fig. 4.13. Heat capacity calculated for three basic temperatures with harmonic and anharmonic potentials.

One should notice that the differences between the harmonic and anharmonic calculations result mainly from the low-energy harmonic phonons, which show the softening at higher temperatures (see Fig. 4.9). These observations provide valuable

insights into the effects of harmonic and anharmonic potentials on the thermodynamic properties of the system at different temperatures.

4.1.8 Negative thermal expansion

Copper pyrophosphate exhibits the negative thermal expansion (NTE) behavior, with the highest NTE coefficient among the oxide materials, according to experimental studies conducted by Shi *et al.* [51]. It was found that the material exhibits NTE within a temperature range from 5 K to 373 K. Here, we investigate the thermal expansion of α-$Cu_2P_2O_7$ using the quasiharmonic approximation (QHA) and anharmonic correction within the SCPH approach. To determine the Helmholtz free energy as a function of temperature and volume given by Eq. (3.20), it is necessary to compute the phonon frequencies for selected volumes, smaller and larger than the volume of the ground state V_0. The volume was modified by approximately 1% in the range from 97% to 103% of V_0. For each volume, the lattice parameters and atomic positions were relaxed and phonon spectra were calculated.

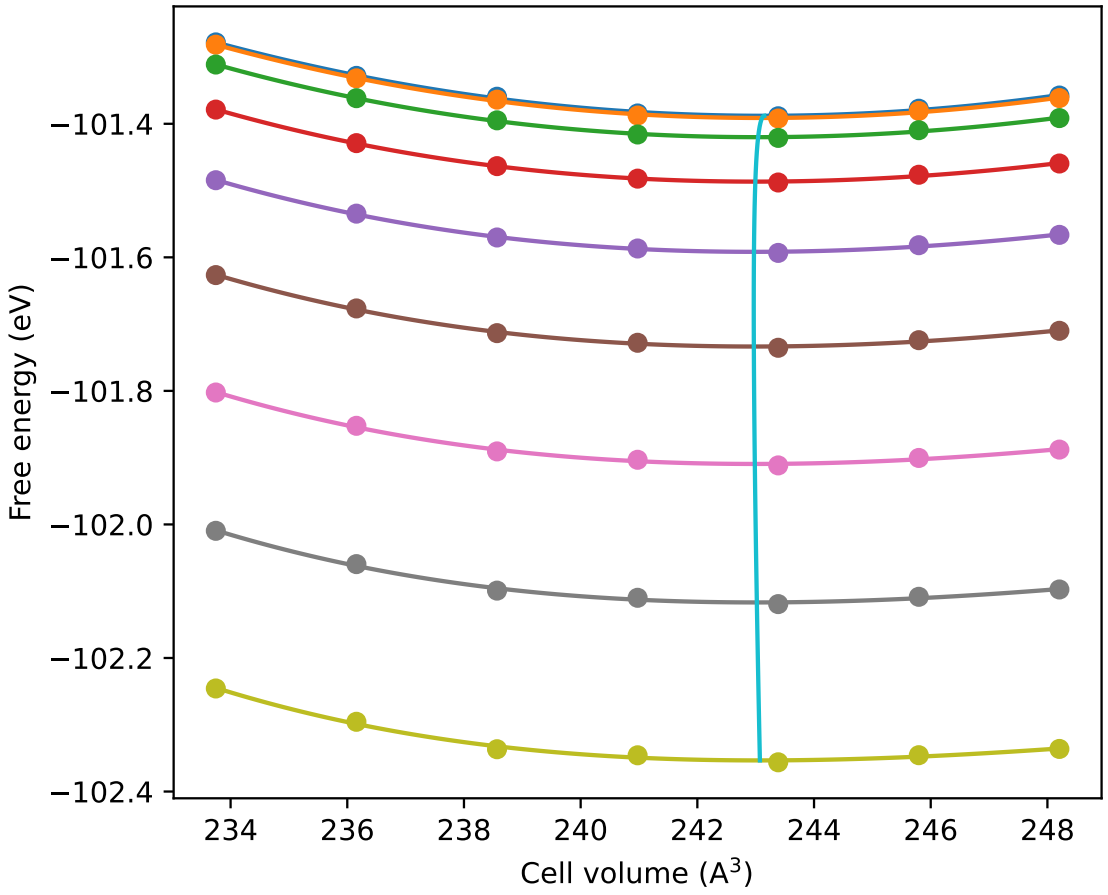

Fig. 4.14. Variation in free energy as a function of material volume calculated for different temperatures within QHA.

The plots presented in Fig. 4.14 depict the free energies obtained within QHA and for temperatures in the range $T = 0 - 350$ K at different volumes of the material. The lines were obtained by the fitting the dependence of the free energy on volume by applying Eq. (2.39). Notably, each specific temperature yields a minimum of $F_{tot}(T, V)$, which defines the corresponding crystal volume for this temperature. The change of the crystal volume in the range of temperatures $0 - 350$ K is depicted in Fig. 4.15. For temperatures higher than 150 K we did not obtain the converged solution of the SCPH equation and the Helmholtz free energy could not be calculated.

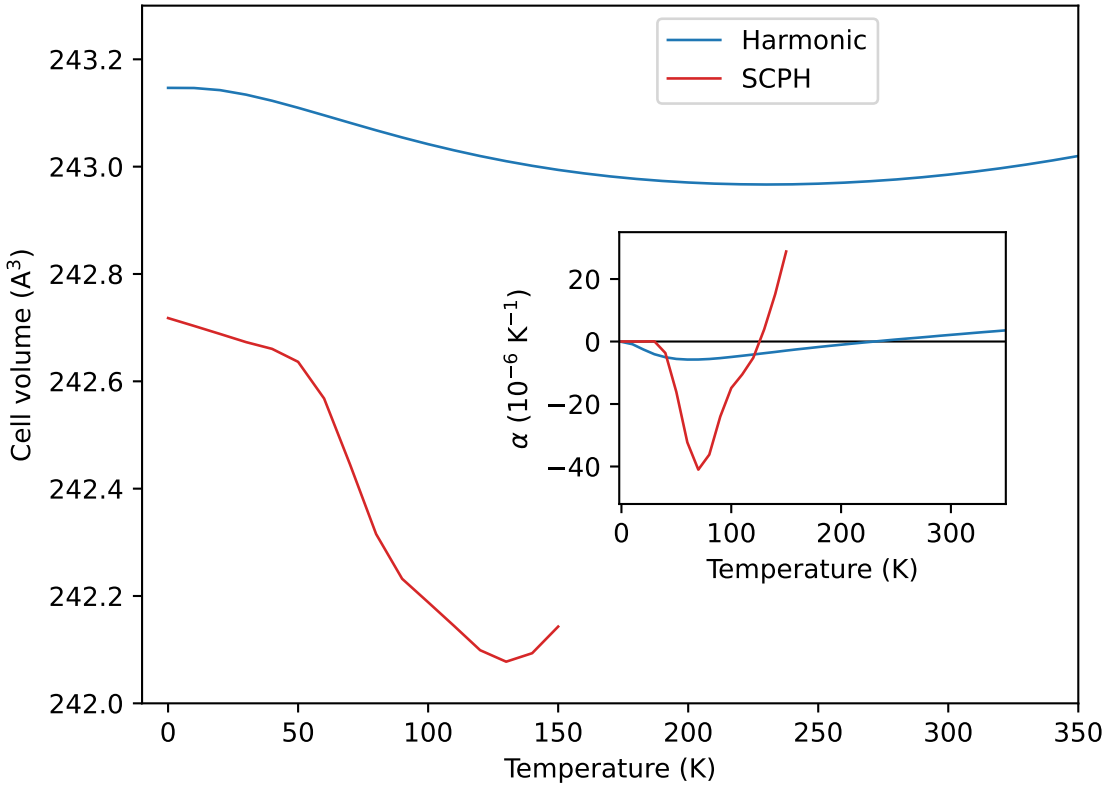

Fig. 4.15. Thermal expansion of α-$Cu_2P_2O_7$. The solid blue line depicts the results obtained from the QHA calculations while the red line depicts the result from the SCPH approach. The inset displays the temperature-dependent volumetric thermal-expansion coefficient.

For harmonic approximation, the volume decreases from $T = 0$ to 235 K and than starts to grow for higher temperatures. For anharmonic calculations, which include the correction to the free energy given by Eq. (3.29), more significant decrease with the temperature is observed. The thermal expansion coefficient presented in the inset of Fig. 4.15 reaches for QHA the minimal value -5.2×10^{-6} K^{-1} at $T = 70$ K. The mean thermal expansivity below the temperature where the transition from NTE to positive thermal expansion (PTE) occurs corresponds to -4.8×10^{-6} K^{-1}. These values are

much lower than the experimentally determined coefficient of thermal expansion $\alpha_V = -27.7 \times 10^{-6}$ K^{-1}. For the SCPH calculation we found the minimal value -41.0×10^{-6} K^{-1} at $T = 70$ K and the average value equals to -31.2×10^{-6} K^{-1}.

In Fig. 4.16, we compare the relative change of the volume with the experimental points taken from Ref. [51]. While the QHA predicts a decrease in the volume of $Cu_2P_2O_7$ with rising temperature, the accord between theory and experiment remains predominantly qualitative. Our calculations result in a relatively shallow minimum in contrast to the behavior of the measured volume, which decreases with temperature up to the α-β structural transition. In the β phase, the crystal structure of $Cu_2P_2O_7$ exhibits the PTE. At elevated temperatures, the QHA theory yields volume changes approximately threefold lower compared to the outcomes from the experiment. This indicates the importance of anharmonic effects in the NTE behavior observed in $Cu_2P_2O_7$. Indeed, the inclusion of quartic anharmonic corrections within the SCPH approach leads to much stronger NTE comparing to harmonic calculations. Below $T = 50$ K, the agreement with the experimental data is quite good but for higher temperatures the decrease of volume becomes much faster. In order to obtain a better consistency with the measurements, also the cubic corrections should be probably included. As found by the *ab initio* studies of NTE in ScF_3, the contribution from the cubic terms to the free energy is significant and has the opposite sign to the SCPH free energy [123]. The investigation of the effect of the cubic corrections, which would likely improve the quantitative agreement with the experimental data, is planned as the next step of our studies.

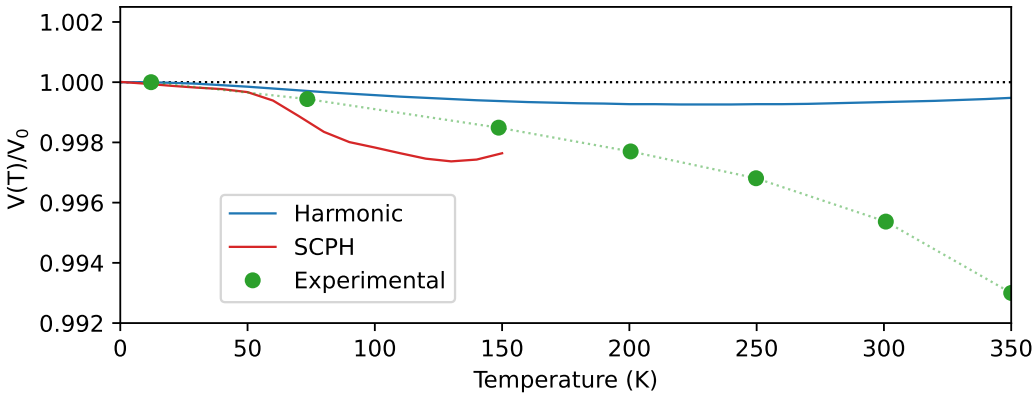

Fig. 4.16. The dependence of the relative volume of $Cu_2P_2O_7$ on temperature, with the blue line depicting the results obtained from QHA calculations and the red line depicting the results from the SCPH method. The experimental data, represented by green points, were extracted from the reference [51].

In our quest to uncover the underlying factors responsible for the structural dis-

tortions, which ultimately lead to NTE, we have extracted additional information through the mean square displacement (MSD) calculation. Notably, our findings show the presence of strong anisotropic displacements for the O1 and O4 atoms, as depicted in Fig. 4.17. Specifically, the MSDs for O1 along the y and z directions and O4 along the x direction exhibit significant increases compared to other MSDs within the NTE temperature range. These results show a good qualitative agreement with the neutron diffraction measurements [51], which revealed even stronger anisotropy in oxygen thermal displacements. The large transverse vibrations of the O1 and O4 atoms induce the twist and rotation of the PO_4 and CuO_5 polyhedra. Such deformations do not modify the P-O and Cu-O bonds within the rigid units but leads to the decrease of the nonbonded Cu-P and Cu-Cu distances with increasing temperature. Consequently, the lattice parameters a and c show the NTE behavior, leading to the volume contraction [51]. Similar mechanism of NTE, in which low-frequency phonon modes induce rotations of rigid units, was found and studied in other compounds [113, 152, 153, 154].

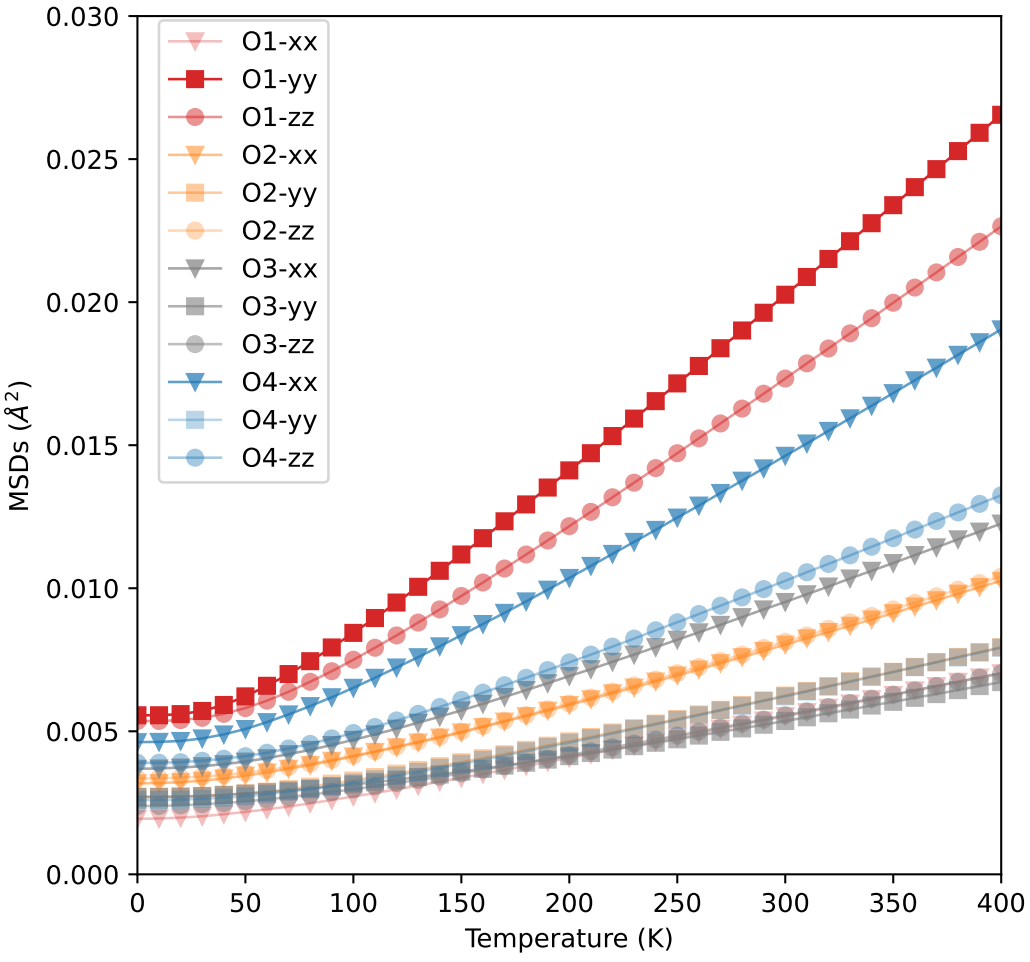

Fig. 4.17. MSDs of oxygen atoms in α-$Cu_2P_2O_7$.

4.2 Investigation of beta phase of copper pyrophosphate

The primary objective of our current first-principles study is to gain in-depth insights into the structural, electronic, and dynamical properties of β-$Cu_2P_2O_7$. Moreover, in the next section (Sec. 4.3) we specifically focus on elucidating the mechanism driving the α–β phase transition. Through our phonon dispersion relation calculations, we have identified the presence of a phonon soft mode that plays a pivotal role in the structural transformation. Our research highlights the essential role of anharmonicity in stabilizing the β phase at higher temperatures. This study seeks to offer a comprehensive insight into the behavior and characteristics of β-$Cu_2P_2O_7$, elucidating the dynamics of phase transition and the significant influence of anharmonicity in this context. Some of these findings have been included in the paper entitled *"Anharmonicity and structural phase transition in the Mott insulator $Cu_2P_2O_7$"* published in Physical Review B [155], contributing to the scientific understanding of this intriguing material.

4.2.1 Calculation details

During the optimization of the crystal structure for the beta phase, the integration in the k-point space was carried out using a $4 \times 4 \times 8$ Monkhorst-Pack mesh [77]. The cutoff energy for this calculation was set to 500 eV. To account for local electron interactions, we applied the GGA+U method, employing the same parameters as those used in the calculations for the alpha phase. We included also the vdW correction D2, which gave the best agreement with the experimental data for the α phase.

The interatomic force constants and phonon energies were computed using the Alamode software [125]. Initially, the direct method [92] was employed to calculate the phonon dispersion relations and phonon density of states (PDOS) within the harmonic approximation. To obtain the HF forces, we induced small displacements of individual atoms within a $2 \times 1 \times 2$ supercell consisting of 88 atoms, while using a $2 \times 2 \times 2$ k-point grid. These HF forces served as the basis to construct the force constants and dynamical matrices. Subsequently, the phonon frequencies and polarization vectors were determined through direct diagonalization of the dynamical matrix.

In the next step, we employ the TDEP approach [119, 94] to account for anharmonic effects. This method determines the atomic potential by considering forces induced by thermal atom displacements at finite temperatures. The configurations of atomic displacements are generated using the HECSS method [126]. The calculations involved utilizing 100 configurations of atomic displacements generated within

a supercell containing 88 atoms, and the analysis was performed at a temperature of $T = 500$ K.

To investigate the impact of anharmonicity on phonon frequencies and to examine the stability of the β phase at elevated temperatures, we implement the SCPH method [125]. The SCPH equation (3.28) was solved using a $4 \times 4 \times 4$ q-point grid. Additionally, we calculate the frequency shift and linewidth of phonons using the real and imaginary parts of the phonon self-energy, within the perturbation theory accounting for the quartic and cubic anharmonicity [125].

4.2.2 Crystal structure

In the β phase of $Cu_2P_2O_7$, the average position of the O1 atom, which is defined by the $C2/m$ space group, corresponds to the linear arrangement of the P-O1-P bridge with the angle of 180° (Fig. 4.18).

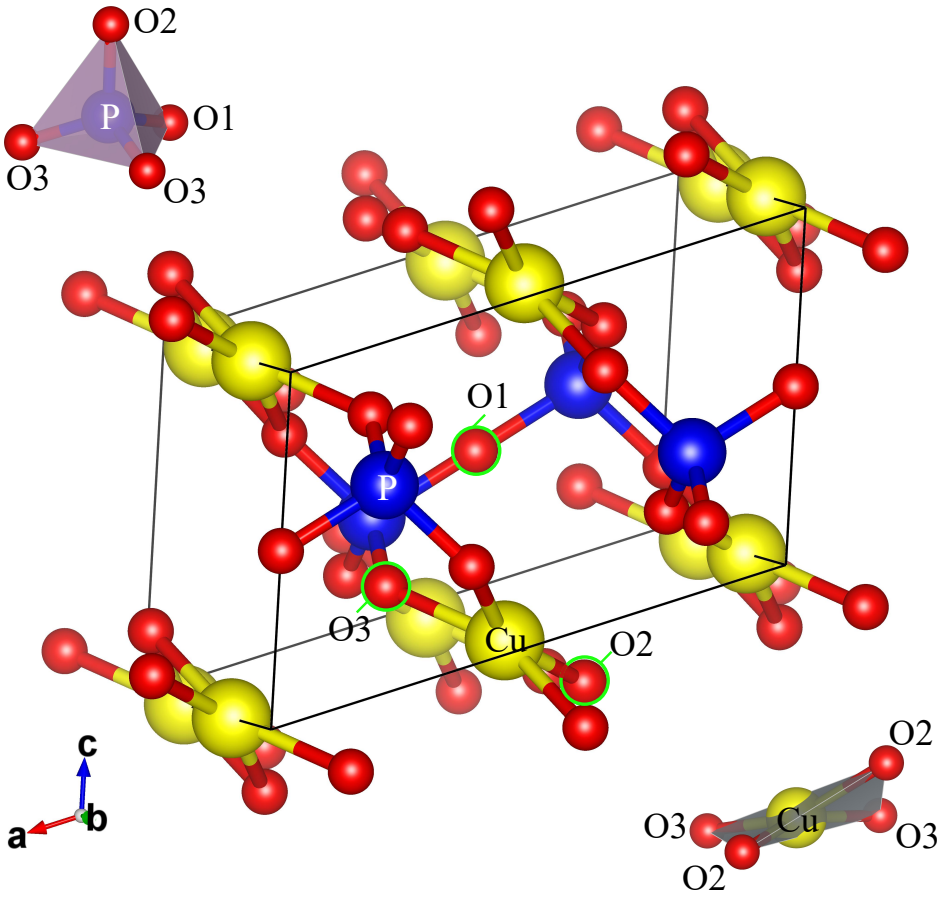

Fig. 4.18. Crystal structure of β-$Cu_2P_2O_7$. Copper ions are represented by yellow balls, phosphorus ions by blue balls and oxygen ions by red balls. The image was rendered using VESTA software. [142].

However, due to a positional disordering, the O1 atoms are displaced randomly to the left or right along the b direction [44]. As a result, the unit cell is approximately two times smaller in the c direction than in the α phase, and it includes only one layer of pyrophosphate groups. Within this unit cell, each Cu atom is coordinated only with four oxygen atoms, thereby forming CuO_4 plaquettes. It is connected with the longer Cu-O3 bond, which increases to 2.655 Å, if compared to the α phase (2.255 Å). In the β phase, also the number of non-equivalent positions of oxygen atoms is reduced to three.

Tab. 4.5 summarises the lattice constants, magnetic moments, and total energies obtained for the β phase of copper pyrophosphate and the experimental data. First we focus on the effects connected with the Coulomb interaction U. As expected and noticed before [50], the magnetic moments on Cu atoms increase with U, improving agreement with the value measured at low temperatures (see Tab. 4.1). Similarly as in the GGA+U calculations for the α phase, we observe the decrease of the lattice constants a and b resulting in a better agreement with the experimental data. The parameter c weakly increases comparing to the GGA calculation. If we compare the total energies with the corresponding values obtained for the α phase (see Tab. 4.1), we see that independently on the method, the α phase, which is the stable structure at low temperatures, correctly exhibits the lower energy than the β phase.

In further analysis we performed the crystal structure optimization including the vdW correction D2. In this case, two lattice parameters b and c only slightly decrease but the parameter a is strongly reduced, therefore, its agreement with the experimental value is significantly improved. Also the monoclinic angle β obtained with the D2 correction agrees very well with the measured value. With this correction, the total energy of the β phase remains higher than the ground state energy for the α phase (see Tab. 4.2). These calculations reveal that the crystal structure of β-$Cu_2P_2O_7$ is also significantly impacted by local Coulomb interactions and van der Waals forces, and they should be incorporated into electronic structure and lattice dynamics studies to accurately characterize the material's behavior.

4.2.3 Electronic properties

Electronic properties of β-$Cu_2P_2O_7$ were thoroughly analyzed through the calculation of partial densities of states for selected atoms, including both the spin-up and spin-down components (see Fig. 4.20). Although the β phase, which is a stable structure at high temperatures, show the paramagnetic behavior, we found the magnetic ground state corresponding to the AFM2 order in the α phase. The computed magnetic moment for Cu was found to be 0.836 μ_B, the same as in α-$Cu_2P_2O_7$ (see

Tab. 4.5. The lattice constants a, b, and c, angle β, total energies, and magnetic moments obtained by different computational methods for β phase of copper pyrophosphate and compared with the experimental data.

	DFT	DFT+U	DFT+U D2	Exp. data [46]
a (Å)	7.0329	6.9415	6.8554	6.8607
b (Å)	8.2148	8.1210	8.0930	8.1367
c (Å)	4.3131	4.3509	4.3238	4.5782
β (deg)	111.14	111.16	109.65	109.29
E (eV)	-280.9090	-199.2978	-206.0920	–
m (μ_B)	0.611	0.835	0.836	–

Tab. 4.1.) This consistency in magnetic moment suggests common underlying magnetic interactions in the both phases of $Cu_2P_2O_7$, providing further evidence for the similarity of these crystal structures. Moreover, the investigation also determined a magnetic moment of 0.032 μ_B on P atoms in the β-$Cu_2P_2O_7$ structure.

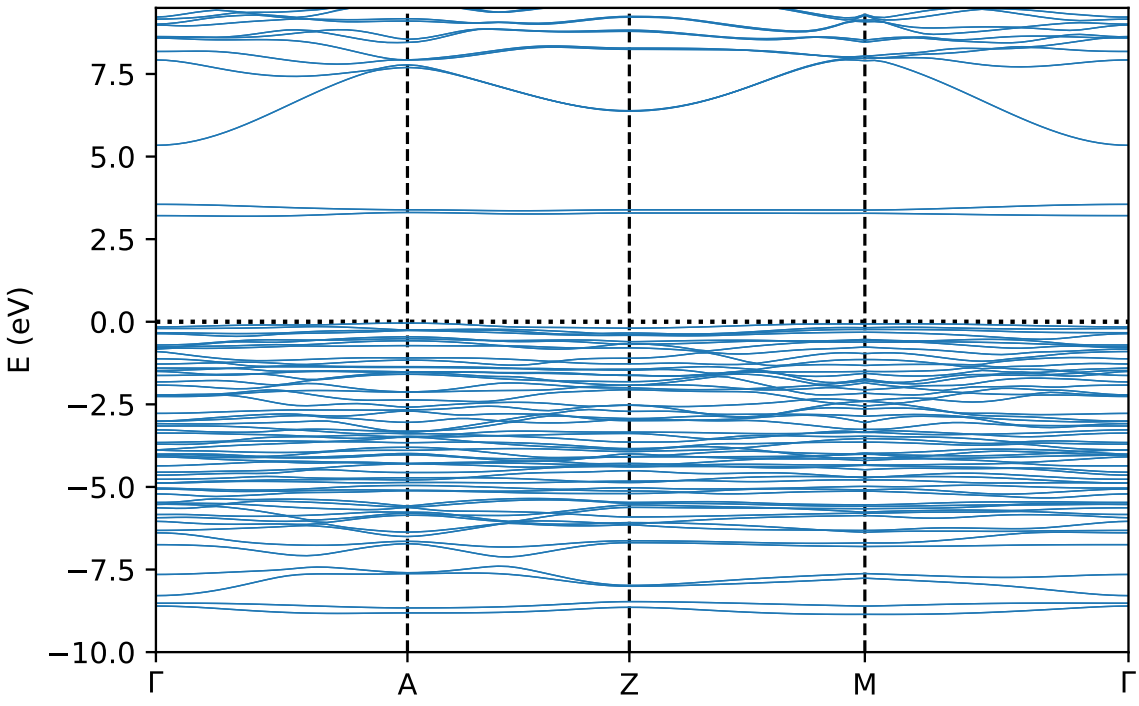

Fig. 4.19. Electronic band structure of β-$Cu_2P_2O_7$. The Fermi level (dotted line) was set to zero.

The electron band structure presented in Fig. 4.19 exhibits the band gap with a magnitude of 2.94 eV, which is reduced by about 7% comparing to the α phase. The

lowest conduction band is also very narrow but now it splits into two subbands. The total and partial electron density of states, which is presented in Fig. 4.20, show similar characteristics as in the α phase. In the vicinity of E_F, the electronic states of the system are predominantly influenced by the O($2p$) orbitals. The lower Hubbard band, characterized by a prominent peak at -9 eV, mainly consists of majority-spin Cu($3d$) states, with a minor contribution from O($2p$) orbitals. On the other hand, the energy gap is evident between the occupied states with both spin components and the upper Hubbard band, which predominantly comprises the empty minority-spin Cu($3d$) states. Between -11 eV and E_F, the $3p$ states on phosphorus atoms are occupied.

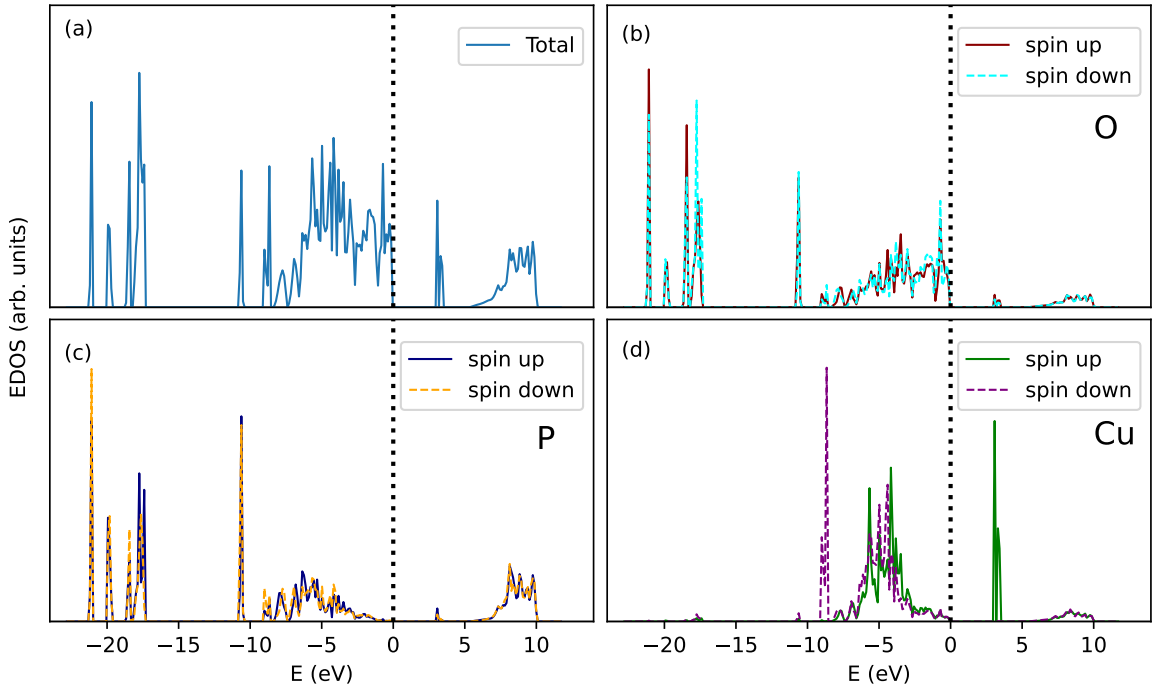

Fig. 4.20. The total and partial density of states (DOS) for the β phase of copper pyrophosphate. The Fermi level (black dash line) is set to 0 eV.

4.2.4 Phonon dispersions

In this section, we analyze the lattice dynamics of the β phase of copper pyrophosphate. The calculated phonon dispersion curves along the high-symmetry directions are shown in Fig. 4.21(a). All phonon frequencies are real apart from one transverse mode close to the A point. The phonons with the imaginary frequencies are plotted here with the negative values. In the next section we discuss the role of this soft mode in the structural phase transition observed in $Cu_2P_2O_7$.

In Fig. 4.21(b), the total PDOS and the partial contributions of Cu, O and P vi-

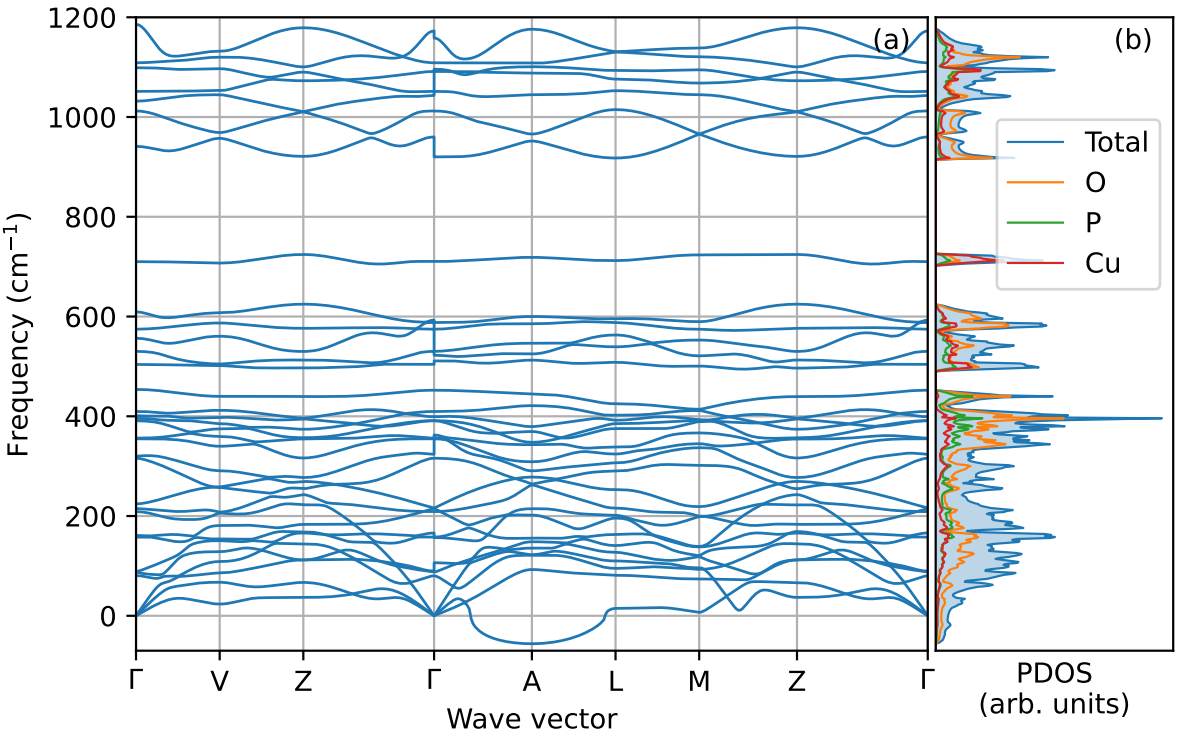

Fig. 4.21. (a) The phonon dispersion relations and (b) the total and partial element-projected PDOS in β phase of copper pyrophosphate.

brations are shown. In the low-frequencies range (approximately 0-200 cm^{-1}), the phonon states are dominated by O vibrations, and the contributions of Cu and P atoms are smaller than in the α phase. In the band about 400 cm^{-1}, the vibrational modes of oxygen atoms prevail. At intermediate frequencies (approximately 500-600 cm^{-1}), there are similar contributions from all types of atoms besides a narrow band around 600 cm^{-1}, where oxygen atoms dominate. In the narrow band around 700 cm^{-1} and at the highest frequencies (approximately 900-1200 cm^{-1}), we observe the enhanced density of Cu states compared to the α phase. In the soft mode (below 0 cm^{-1}), the main contribution comes from the oxygen atoms.

Using group theory, all phonon modes in the center of the Brillouin zone (3 acoustic and 30 optical modes) can be classified according to one-dimensional irreducible representations

$$\Gamma = 8A_g(\mathrm{R}) + 7B_g(\mathrm{R}) + 7A_u(\mathrm{I}) + 11B_u(\mathrm{I}), \tag{4.2}$$

where R and I denote the Raman and infrared modes, respectively. Tab. 4.6 presents the calculated frequencies of the Raman active modes at the Γ point obtained using the Phonon software. Most of the modes show a good agreement with the experimental values taken from Ref. [46]. Addionally, we included several Raman modes

Tab. 4.6. Frequencies and symmetries of the Raman modes at the Γ point in $Cu_2P_2O_7$ compared with the experimental data.

Theory		Experiment [46]	
α-phase [50]	β-phase	α-phase	β-phase
87.059 (A_g)	87.816 (B_g)	105	-
163.813 (B_g)	157.765 (B_g)	160	159
215.048 (A_g)	208.787 (A_g)	214	211
223.645 (B_g)	214.719 (B_g)	-	255
321.589 (A_g)	316.010 (A_g)	320	318
347.274 (B_g)	354.898 (B_g)	-	-
354.845 (A_g)	356.436 (A_g)	360	358
404.947 (A_g)	391.070 (A_g)	412	407
-	409.568 (B_g)	-	-
527.498 (A_g)	530.301 (A_g)	544	544
573.630 (B_g)	574.585 (B_g)	590	587
707.990 (A_g)	710.141 (A_g)	730	645
950.224 (B_g)	1011.554 (A_g)	975	969
1016.637 (A_g)	1051.480 (A_g)	1050	1050
1109.001 (B_g)	1108.790 (A_g)	1080	1080

calculated previously for the α phase [50]. We present here only phonon modes with similar frequencies as in the β phase, while all zone center modes are presented and discussed in Sec. 4.1.5.

4.3 Structural phase transition

In this section, we present a comprehensive study of the structural phase transition by analysing the phonon dispersion relations calculated for the β phase. The investigation reveals the presence of a soft mode at the A point of the Brillouin zone, indicating the dynamical instability of the β phase at low temperatures. Moreover, we derive a double-well potential associated with the soft mode, and its implications on the mechanism of the structural phase transition to the α phase are discussed. To further explore the thermal behavior of the system, we perform self-consistent phonon calculations based on the temperature-dependent effective potential. The presence of the soft mode and its temperature-dependent behavior underscore the importance of considering anharmonic effects in understanding the structural phase transition.

4.3.1 The soft mode

In the structural phase transformation observed in $Cu_2P_2O_7$, the volume and lattice parameters change continuously, therefore, it was classified as the second-order phase transition [44]. It is also supported by the analysis of the symmetry elements in the α and β phases. Usually, the second-order structural transitions are driven by the soft phonon modes that describe the collective motion of atoms, transforming a higher-symmetry crystal structure into a lower-symmetry crystal structure. As the critical temperature is approached, such a phonon mode with decreasing frequency may stand out, signaling a structural phase transformation [156]. In $Cu_2O_2O_7$, the phonon dispersions have not been measured and the soft-mode behaviour has not been observed experimentally yet.

As presented in Fig. 4.21, our calculations revealed such soft mode, which appears around the A point at the Brillouin zone boundary with the wave vector $\mathbf{k} = (0, 0, 0.5)$. This wave vector corresponds to a structural deformation, which doubles the lattice parameter c in the α phase, and this soft mode may be responsible for the structural transformation. Indeed, by the group theory analysis, we confirmed that the structural phase transition can be described by the following group-subgroup relation

$$C2/m \rightarrow A_1^- \rightarrow C2/c, \tag{4.3}$$

where the irreducible representation A_1^- plays the role of the order parameter. By analysing the atomic displacements induced by the soft mode, we found that only O1 atoms show the pronounced amplitude and the contribution of other atoms is much smaller. As displayed schematically in Fig. 4.22, the O1 atoms oscillate along the b direction, which is perpendicular to the P–O–P bridge. Notably, the direction of its displacement changes between consecutive unit cells along the c direction. Consequently, the condensation of the soft mode in the α phase causes the unit cell to double along the c direction.

Below the phase transition, the soft mode is stabilised and changes into the optical mode at the Γ point with the symmetry A_g. In Tab. 4.6, it is lowest Raman-active mode with the frequency 87.06 cm^{-1}. This particular mode was previously connected with the strong NTE observed in $Cu_2P_2O_7$ [51]. Therefore, our analysis shows that the same phonon mode is responsible for the NTE in the α phase and the α-β phase transition.

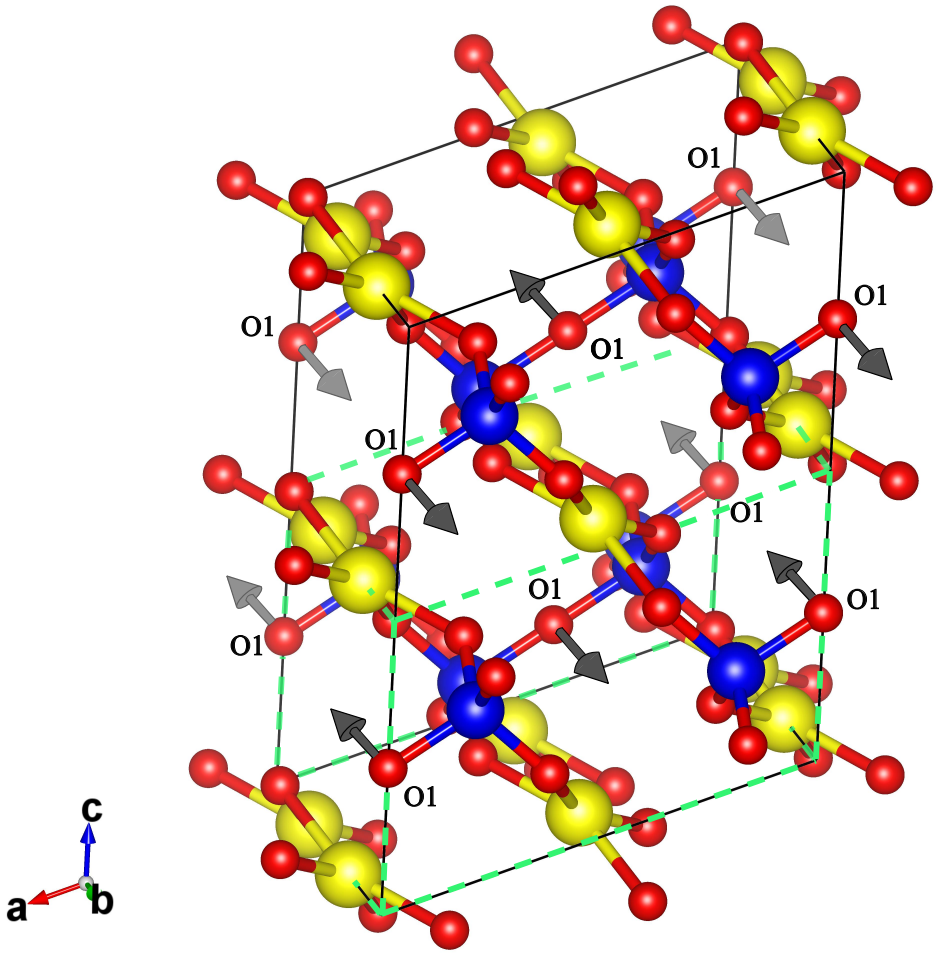

Fig. 4.22. The crystal structure of $Cu_2P_2O_7$ and schematic representation of oxygen displacements (indicated by black arrows) in the soft mode inducing the α-β phase transition. The unit cells in the α and β phases are plotted by the solid black and dashed green lines, respectively. Copper ions are represented by yellow balls, phosphorus ions by blue balls and oxygen ions by red balls. The image was rendered using VESTA software. [142].

4.3.2 The double-well potential

A typical energy potential associated with the soft mode has the shape of a double well with two minima shifted from the central position. In the case of copper pyrophosphate, it governs the movements of O1 atoms in the high-temperature disordered phase and determines their static displacements in the α phase. This potential can be determined by calculating the change of the total energy ΔE of the unit cell as a function of the O1 displacement u using the soft mode's polarization vector as shown in Fig. 4.23. The central position of O1 corresponds to $u = 0$. The energy ex-

hibits a decreasing trend, reaching its minimum value at an amplitude of $u = 0.23$ Å, which well agrees with the position of O1 obtained from diffraction measurements for the β phase, $u_{\mathrm{exp}}(\beta) = 0.27$ Å.

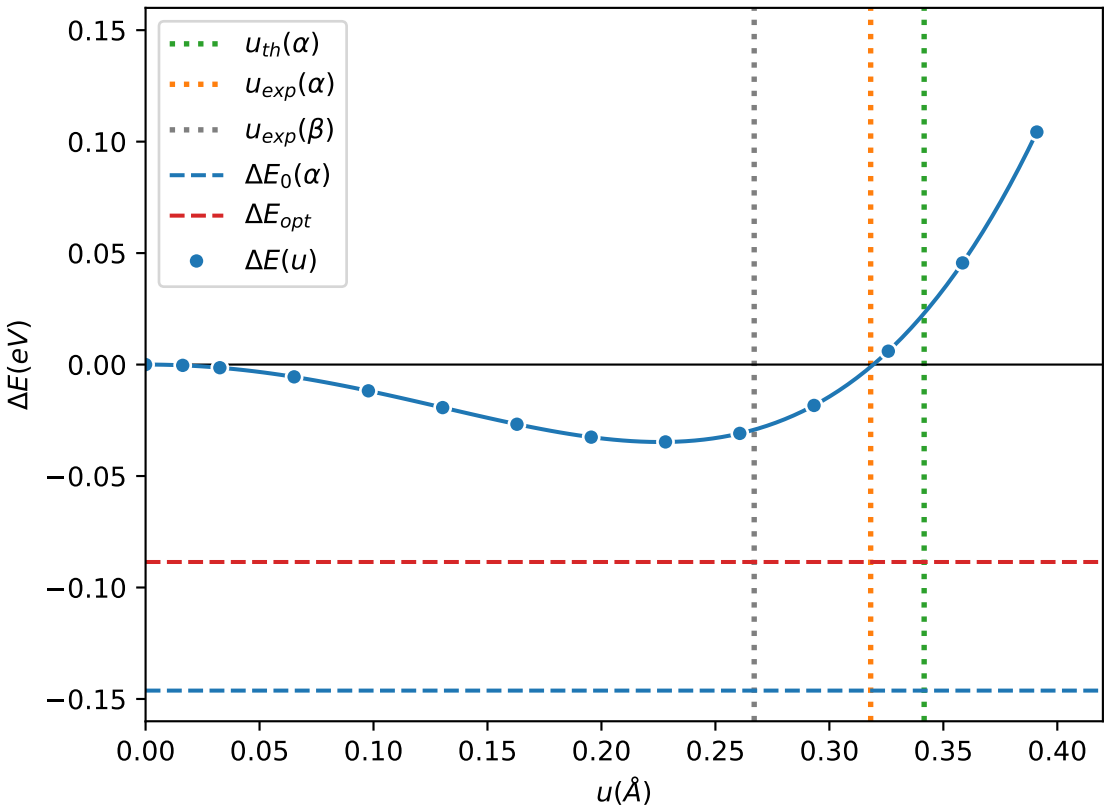

Fig. 4.23. The energy potential of the soft mode at the A point as the function of the amplitude of the O1 oxygen. The energy of the distorted β phase after relaxation and the ground state energy of the α phase are plotted with the dashed red and blue horizontal lines, respectively. The experimentally determined positions of O1 in the β and α phases are plotted with the dotted gray and orange vertical lines, respectively. The theoretical position of O1 in the α phase is shown with the dotted green vertical line.

The relaxation of the distorted structure results in a lower energy state, as indicated by the dashed red line in Fig. 4.23. However, this energy value remains higher than the ground state energy attained through the full optimization process, initiated from the experimental atomic positions and lattice parameters within the α phase (dashed blue line). The displacement of O1 from its central position, determined for the α phase, is equal to $u_{\mathrm{th}}(\alpha) = 0.34$ Å, in a good agreement with the experimental value of $u_{\mathrm{exp}}(\alpha) = 0.32$ Å. This correspondence between the calculated and experimental values further validates the accuracy of the theoretical predictions and the reliability of the full optimization procedure.

4.3.3 Anharmonic lattice dynamics

Thermal effects play a significant role in stabilizing the soft mode at the A point, leading to a notable dependence of its frequency on temperature. Therefore, in order to properly describe the lattice dynamics of the high-temperature phase, we need to include the anharmonic effects.

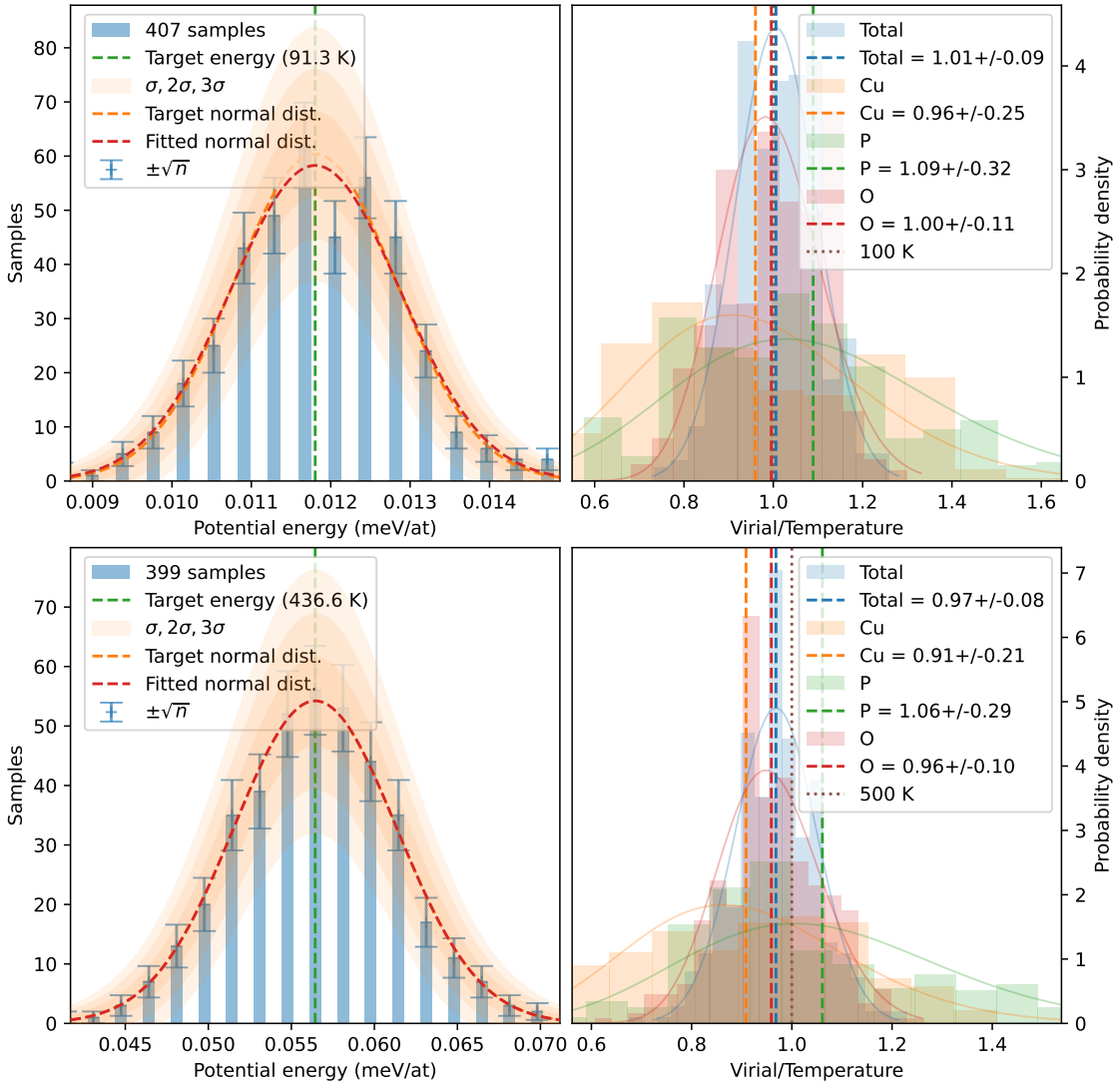

Fig. 4.24. Monitoring histograms for the configuration list (on the left side) and the viral distribution within the sample (on the right side) obtained for β-$Cu_2P_2O_7$ at temperatures 100 K and 500 K.

Initially, we create atomic displacements at several distinct temperatures using the HECSS method. Subsequently, we use VASP to calculate the total energy and HF forces acting on all atoms for each set of displacements. This process mirrors the one followed for the α phase. Next, utilizing ALAMODE, we generate a fitting file and proceed with potential and phonon calculations for the specified temperatures.

Additionally, we meticulously select a specified number of generated samples (N) and provide a temperature (T) in kelvins to guide this displacement process. It's worth noting that the beta phase is a high-temperature phase, so to achieve better results, we generate twice as many samples compared to the alpha phase ($N = 100$).

The overall probability of an individual atom's displacement in the crystal is determined by summing all distributions that align with this specific displacement, as illustrated in Fig. 4.24.

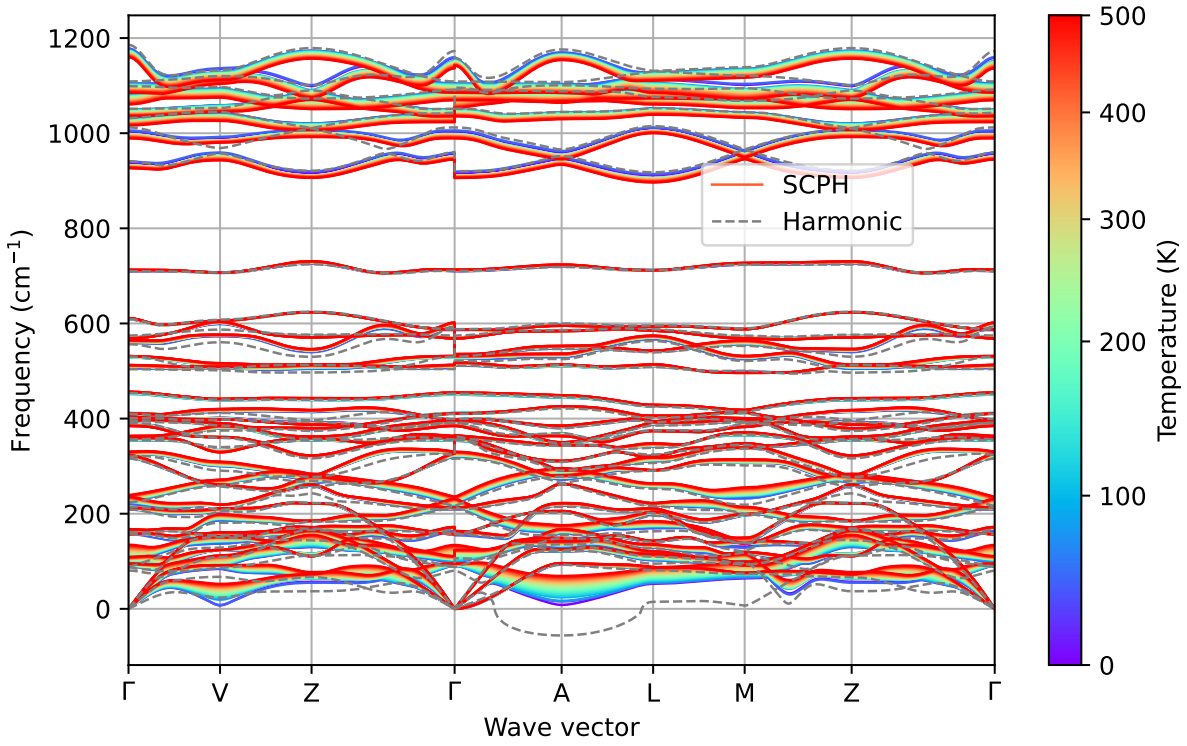

Fig. 4.25. Phonon dispersion relations obtained for β-$Cu_2P_2O_7$ within the harmonic approximation (dashed gray line) and using the TDEP+SCPH approach (rainbow color bar).

In this figure, we present data only for two selected temperatures for the comparison ($T = 100$ and 500 K). After examining the data obtained from the sampling distribution and atomic virial distribution, we move forward with computing the phonon dispersion curves for the range of temperatures. This calculation takes into account the anharmonic corrections to the potential, considering terms up to cubic or quartic order, as determined within the TDEP method.

The phonon dispersion relations of β-$Cu_2P_2O_7$ obtained within the SCPH method in the temperature range $T = 0 - 500$ K are presented in Fig. 4.25. They are compared with the phonon dispersions calculated by the direct method and analyzed in Sec. 4.2.4. We observe that the soft mode is stabilized by the anharmonic correction

and shows a strong temperature dependence. The strongest effect is found at the A point but also other phonons belonging to the lowest dispersion curve, especially at the V and L points, exhibit substantial shift to higher frequencies with increasing temperature. This observation underscores the essential contribution of anharmonicity in stabilizing the high-temperature β phase of copper pyrophosphate.

4.3.4 Phonon spectral function

In the final step, we calculate the phonon spectral function $S_q(\omega)$ using the phonon linewidth (Γ_q) and frequency shift (Δ_q) obtained from the the phonon self-energy including the bubble diagrams [125]. The calculation of $S_q(\omega)$ is based on the SCPH results, therefore, the final phonon frequencies are equal to $\omega_{\mathrm{SCPH}}(q) + \Delta_q$. In order to study the anharmonic behavior of the soft mode, in Fig. 4.26 we present the phonon profiles calculated for the A point with $\boldsymbol{q} = (0, 0, 0.5)$ using Eq. 3.27.

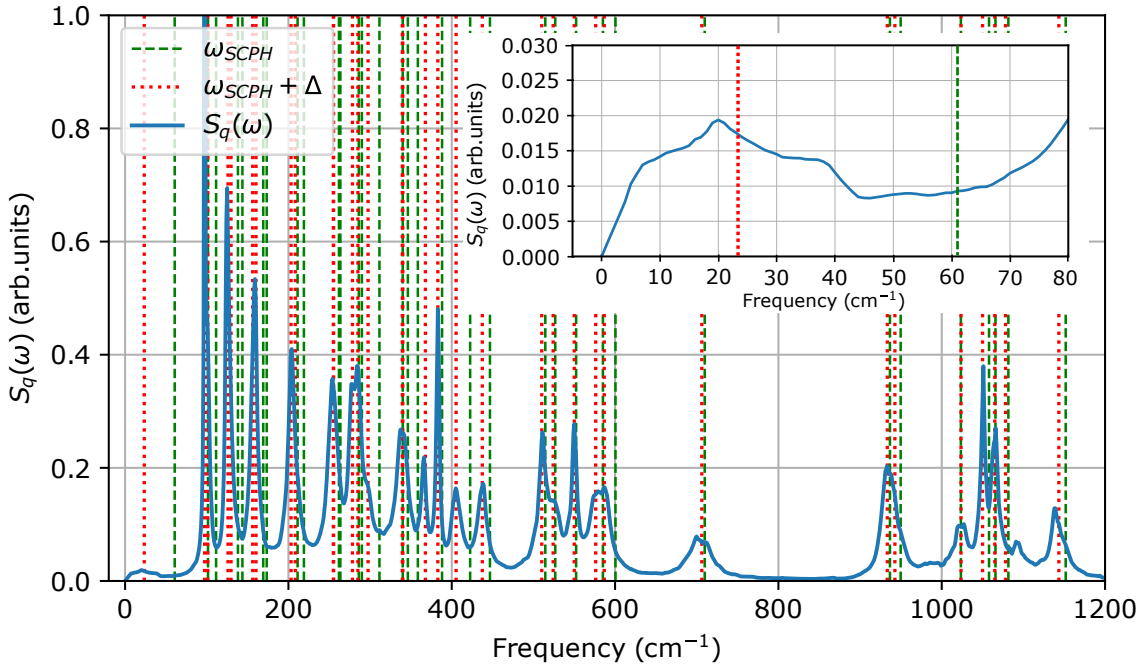

Fig. 4.26. The phonon spectral function obtained from the anharmonic self-energy at the A point with $\boldsymbol{q} = (0, 0, 0.5)$ for $T = 500$ K.

The frequencies of phonons obtained within the SCPH method are marked by the dashed green lines, while the positions of phonon peaks by dotted red lines. Since $\Delta_q < 0$, all corrected frequencies are shifted to lower values. As we see, most of the phonon peaks show very weak frequency shift comparing to the SCPH values and their linewidths are rather small. A radically different behavior is observed for the

lowest mode, which exhibits a strong damping and softening due to the anharmonic effects (see the inset in Fig. 4.26).

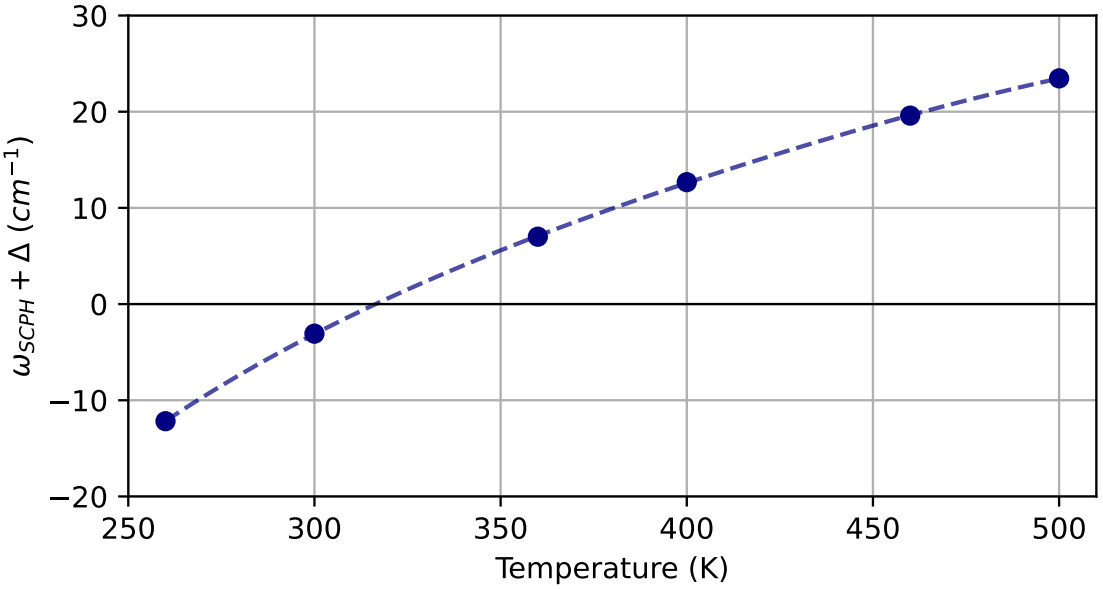

Fig. 4.27. Temperature dependence of the soft-mode frequency.

Using the SCPH method, we found that the frequency of the soft mode approaches zero with decreasing temperature (Fig. 4.25), leading to the structural phase transition. However, in order to estimate the critical temperature we have to take into account the shifts of frequencies Δ_q, which depend on temperature. In Fig. 4.27, we plot the corrected frequency of the soft mode as a function of temperature. The frequency goes to zero when we approach $T \sim 320$ K, and we can treat it as the temperature of the structural phase transition. It is only the approximate estimation of the critical temperature, but it corresponds quite well to the experimental value, which is approximately 360 K [46, 44, 45].

The presented results demonstrate that the anharmonic and thermodynamic properties of copper pyrophosphate can be successfully studied within the TDEP and SCPH methods in connection with the recently developed HECSS approach. It opens a new route to investigate even more complicated materials, molecular crystals or heterostructures.

4.4 Summary

The theoretical analysis was focused on the structural, electronic, and dynamical properties of the α and β phases of $Cu_2P_2O_7$ using DFT. The optimized lattice parameters and atomic positions of the α phase were compared with the diffraction

data obtained for copper pyrophosphate nanocrystals embedded within SBA-15 silica mesopores. Incorporating local Coulomb interactions and van der Waals corrections into the calculations results in the lattice parameters of both phases closely matching the experimental data. Furthermore, previous studies on the $Cu_2P_2O_7$ crystal were considered for comparison. The electronic band structure exhibited a Mott insulating state, attributed to electron interactions within copper ions. The Mott insulating band gap in the β phase, which is $E_g = 2.94$ eV, is slightly narrower than that in the α phase (3.17 eV). This value aligns closely with experimental observations. The antiferromagnetic configurations identified in both phases, where the magnetic moments are 0.86 μ_B, closely resemble each other and are consistent with the experimentally observed long-range order below the critical temperature $T_N = 27$ K.

The calculated phonon frequencies and their assignments for the α phase exhibited good agreement with the previous non-polarized Raman spectroscopy studies conducted on single crystals. The Raman spectrum also matched the measurements performed on the nanocrystals embedded in SBA-15 silica pores. Additionally, the investigation explored the anharmonic properties of the α phase of copper pyrophosphate. Finally, the negative thermal expansion, which is particularly pronounced in this material, was theoretically described. The calculations demonstrated the important role of anharmonic effects in this phenomenon.

The calculated phonon dispersion curves and phonon density of states provided confirmation of the dynamical stability of the α phase at low temperatures. Additionally, the β phase dynamic instability at low temperatures was identified by a soft mode at the A point of the Brillouin zone through phonon dispersion calculations. Also, a double-well potential associated with this soft mode was derived and its role in the structural phase transition to the α phase was discussed. The soft mode mainly causes O1 atom vibrations, which produces static displacements in the b direction and doubles the lattice parameter c in the α phase. We were able to determine the positions of O1 atoms in good agreement with the diffraction data due to the obtained double-well potential. Furthermore, self-consistent phonon calculations, considering temperature-dependent effective potential, revealed a significant temperature dependence and demonstrated the stabilization of the β phase at high temperatures, primarily due to anharmonic effects. The estimated transition temperature was found to be 320 K, which well corresponds to the experimental value of around 360 K.

Consistent with prior observations, it has been established that NTE is related to the vibrations of O1 atoms along the direction perpendicular to the POP bridge. Our analysis suggests that the lowest optical A_g mode in the α phase, which is responsible for NTE, corresponds to the soft mode identified in the β phase. Moreover, the

study emphasized the significant impact of anharmonicity on the structural phase transition, as evidenced by the pronounced temperature dependence and substantial line width of the soft mode.

Chapter 5

Iron pyrophosphate

Within this section, a theoretical examination is conducted, focusing on the structural, electronic, and dynamical properties of $Fe_4(P_2O_7)_3$. This study includes a thorough comparison between the ascertained outcomes and empirical observations. Notably, the investigation of structural and electronic properties is undertaken through calculations encompassing three distinct antiferromagnetic configurations.

5.1 Calculation details

The computations presented within this study employed the projector augmented-wave (PAW) approach [76] and the generalized gradient approximation (GGA) [133] implemented within the Vienna Ab initio Simulation Package (VASP) [79, 80]. The optimization of the crystal structure was conducted within a unit cell, which is equivalent to the primitive cell, housing a total of 124 atoms. To effectively sample the Brillouin zone, integration within the k-point space was performed employing a Monkhorst-Pack mesh of $4 \times 2 \times 4$ [77]. A cut-off energy of 500 eV was utilized to ensure a favorable level of precision in the calculations. Moreover, the investigation encompassed the evaluation of magnetic ground state through computations conducted for three distinct antiferromagnetic (AFM) configurations.

Within this research, computations were executed using the DFT+U technique, incorporating distinct parameters for iron and oxygen atoms. The central aim of these calculations was to get insights into the electronic characteristics of the iron pyrophosphate structure. The outcomes presented herein pertain to the employment of $U_d = 8$ eV and $J_d = 0.9$ eV for the Fe($3d$) states, as well as $U_p = 4$ eV and $J_p = 0.5$ eV for the O($2p$) states. This parameter set yielded an insulating state, featuring an electronic band gap $E_g = 2.57$ eV. This specific combination of U and J parameters yielded good compatibility with the experimental lattice parameters, as showcased

in Tab. 5.1. We should note that the calculations performed for smaller values of $U_d = 4$ eV and $U_p = 2$ eV, as well as for $U_d = U_p = 0$, have not converged to a well-defined equilibrium state, indicating the importance of local Coulomb interactions in iron pyrophosphate.

5.2 Crystal structure and magnetic order

At room temperature, $Fe_4(P_2O_7)_3$ crystallizes in the $P2_1/n$ (14) space group with four chemical formulas in the primitive cell. There are four distinct crystallographic positions of iron encompassed within distorted octahedral geometries, with terminal oxygen atoms originating from diphosphate (P_2O_7) groups serving as their coordination ligands. The six O atoms come from six different diphosphate groups. As illustrated in Fig. 5.1, both of these octahedron types are connected to one another via three common oxygen atoms (thus sharing one face) to form double octahedrons (Fe_2O_9 dimers).

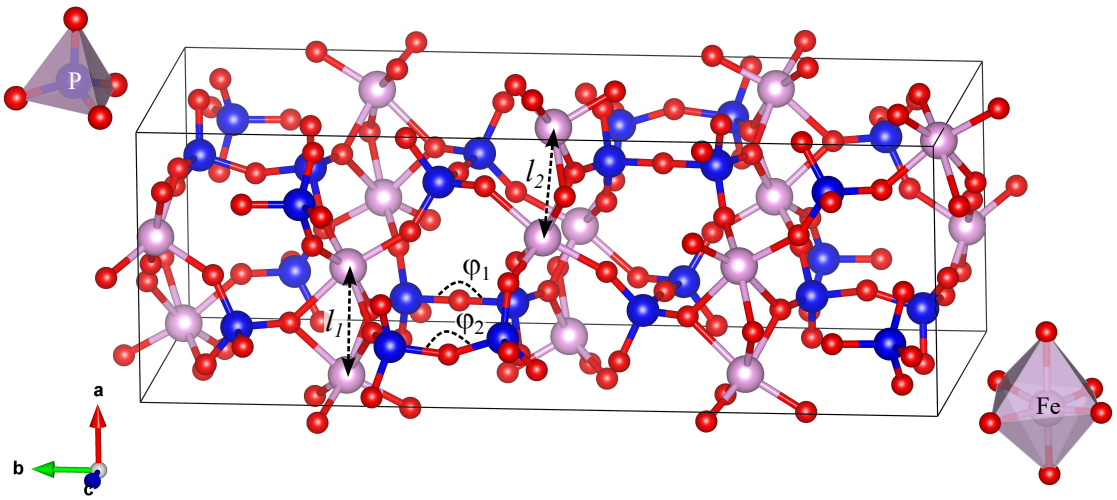

Fig. 5.1. Crystal structure of $Fe_4(P_2O_7)_3$. Iron ions are represented by pink balls, phosphorus ions by blue balls and oxygen ions by red balls. The lengths l_1, l_2 and angles φ_1, φ_2 represent the intradimer Fe-Fe distances and bridging bond P-O-P angles, respectively. The image was rendered using VESTA software [142].

The O-surface manifests a mirror plane intrinsic to each of the two distinct double octahedral configurations, thus endowing the clusters with $P2_1/n$ symmetry. This interconnected arrangement engenders notably abbreviated iron-iron separations, specifically quantified as l_1 = 3.005 Å and l_2 = 3.048 Å. The obtained values agreed very well with experimental data [61], where corresponding values were reported to be equal l_1 =2.967 Å, l_2 =3.048 Å. The arrangement further encompasses

	AFM1 (D2)	AFM2	AFM3	Experimental [61]
a (Å)	7.441 (7.409)	7.441	7.438	7.389
b (Å)	21.571 (21.459)	21.569	21.571	21.337
c (Å)	9.583 (9.535)	9.583	9.585	9.517
β (deg)	90.07 (90.03)	90.08	91.27	90.03
E (eV)	-667.372	-667.305	-667.302	–
m (μ_B)	4.598	4.602	4.600	4.55(5)

Tab. 5.1. The lattice constants *a*, *b*, and *c*, angle *beta*, total energies, and magnetic moments obtained for three types of the AFM configuration of iron pyrophosphate were compared with the experimental data.

three distinct forms of crystallographically non-equivalent diphosphate groups. In all instances, the coordination of iron atoms involves the utilization of all six oxygen atoms, although the bridging oxygen atom remains uninvolved. This non-participation is attributed to the geometric disposition wherein the mirror plane, perpendicular to the lattice's a-axis, encompasses both phosphorus atoms, the bridging oxygen atom, and one of the terminal oxygen atoms. It is noteworthy that in this structure we have two variants of P_2O_7 anions that exhibit two bridging bond angles, characterized by a φ_1=179.81° and φ_2=148.20°.

The cell parameters and magnetic moments on Fe atoms were calculated for three different types of antiferromagnetic configurations (AFM1, AFM2, AFM3) presented in Fig. 5.2 and compared with the experimental data in Tab. 5.1. The AFM1 order corresponds to the magnetic configuration observed by the neutron diffraction measurements below the Néel temperature $T_{\mathrm{N}} = 50$ K [61]. In this arrangement, the magnetic moments on two Fe atoms within the dimers (along the *a* direction) have opposite directions, and the nearest-neighbor iron atoms along the *c* direction exhibit parallel alignment of magnetization. The antiparallel arrangement of moments within the Fe dimers results from the direct AFM interaction due to relatively small Fe-Fe distances and indirect superexchange interactions along the Fe-O-Fe path [61]. The interactions between dimers exhibit the frustrated character due to the FM and AFM superexchange via phosphorus ions. AFM2 is characterized by the opposite directions of moments along the *a* and *c* directions, while AFM3 possesses the arrangement of moments with antiparallel alignment along the *c* direction and parallel magnetizations within the dimers. The calculated values of magnetic moments ($m \simeq 4.6\ \mu_{\mathrm{B}}$) as well as the lattice parameters depend very weakly on the particular AFM configuration. Only the monoclinic angle β obtained for AFM3 shows a slightly

worse agreement with the experimental value (see Tab. 5.1). AFM3 also exhibits the highest total energy due to the parallel alignment of magnetic moments within the Fe dimers.

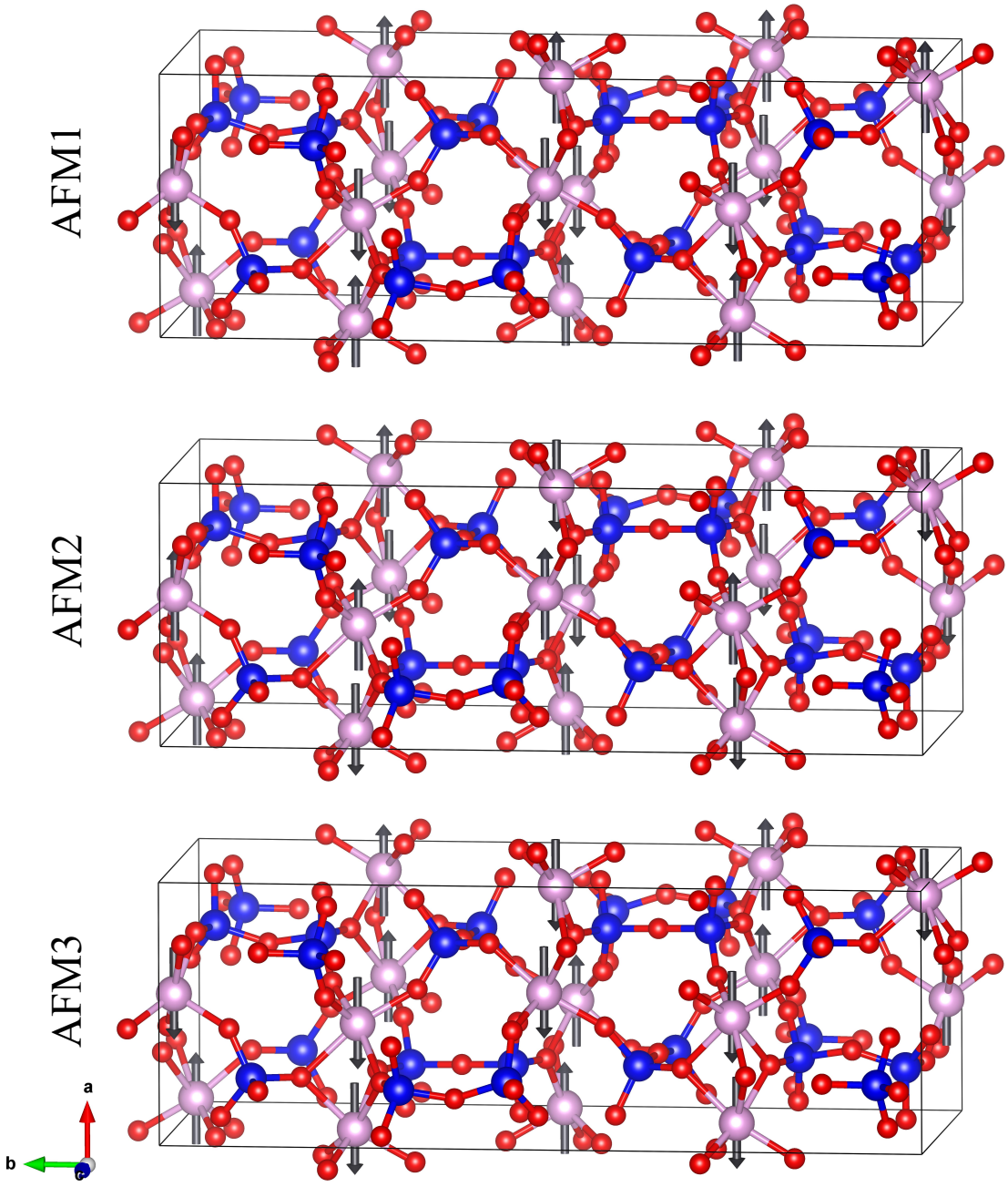

Fig. 5.2. Representation of magnetic moments on the iron atoms of $Fe_4(P_2O_7)_3$ for three AFM configurations.

Our findings exhibit a high degree of agreement with experimental observations. The established ground state, characterized by the AFM1 arrangement, correlates closely with the experimental outcomes, showing a very good agreement with the measured magnetic moment $m = 4.55\ \mu_B$ at $T = 1.7$ K [61]. Furthermore, the prelim-

inary calculations, which took into account the van der Waals correction D2, demonstrate a notable impact on the lattice parameters, yielding values much closer to those obtained experimentally (see Tab. 5.1). Continuing with our investigation, our scrutiny was centered exclusively on the AFM1 configuration.

5.3 Electronic properties

The electronic characteristics of $Fe_4(P_2O_7)_3$ were subjected to an exhaustive analysis, involving the calculation of partial densities of states for selected atoms, encompassing both spin-up and spin-down components. The calculated magnetic moment for iron was determined to be 4.598 μ_B, a value in close proximity to the experimental observation of 4.55 μ_B (see Tab. 5.1). This high-spin configuration results from the first Hund's rule applied to the occupied $3d^5$ states in Fe^{3+} ions.

The electronic band structure of $Fe_4(P_2O_7)_3$ reveals the presence of a band gap with a width $E_g = 2.57$ eV (Fig. 5.3). The energy gap, which exhibits a minimal dependence on the wave vector, is observed between the wide valence band with a width of approximately 11 eV and the narrow and flat conducting band.

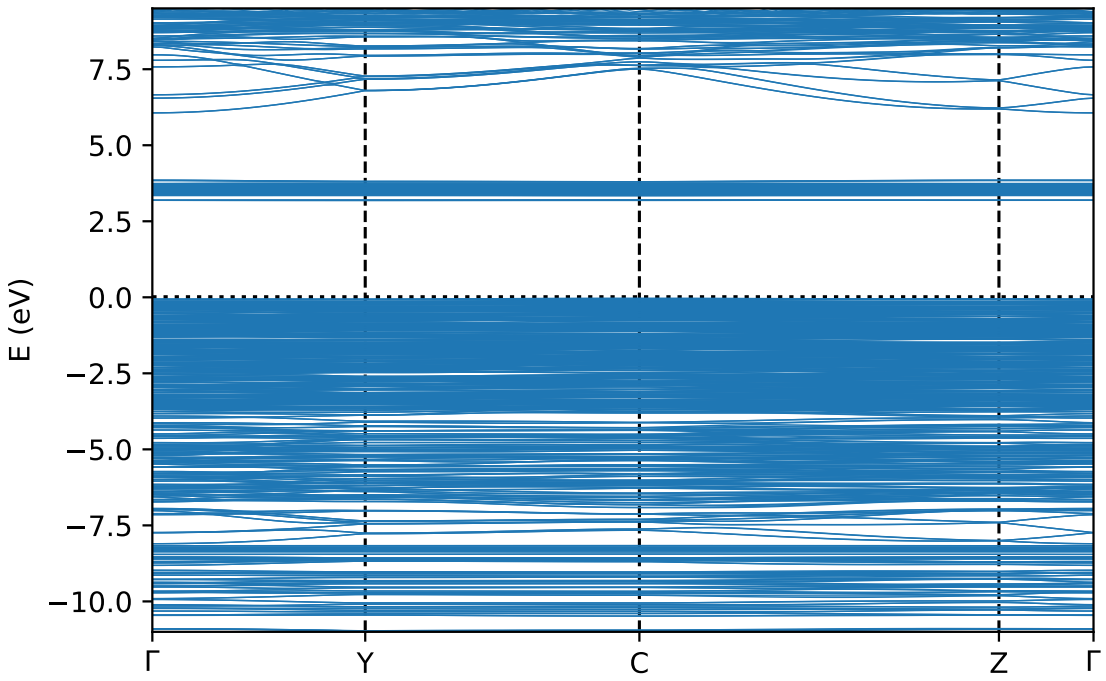

Fig. 5.3. Electronic band structure of copper pyrophosphate. The Fermi level (dotted line) was set to zero.

The AFM1 ordering leads to an equivalent overall electronic density of states (DOS) for both spin orientations (Fig. 5.4). An analysis of the partial DOS, presenting

the electronic states projected onto all types of iron atoms, discloses the manifestation of exchange splitting within the 3*d* states. Weak contributions originating from both spin components become apparent within the energy interval ranging from -7 eV to the Fermi energy (E_F). A notable band, centered approximately at -8 eV, predominantly comprises majority-spin states, constituting the lower Hubbard band. A distinct gap with a width of $E_g = 2.57$ eV becomes discernible between occupied states embracing both spin components and the unoccupied minority-spin 3*d* states, the latter exhibiting a pronounced peak at around 4 eV forming the upper Hubbard band.

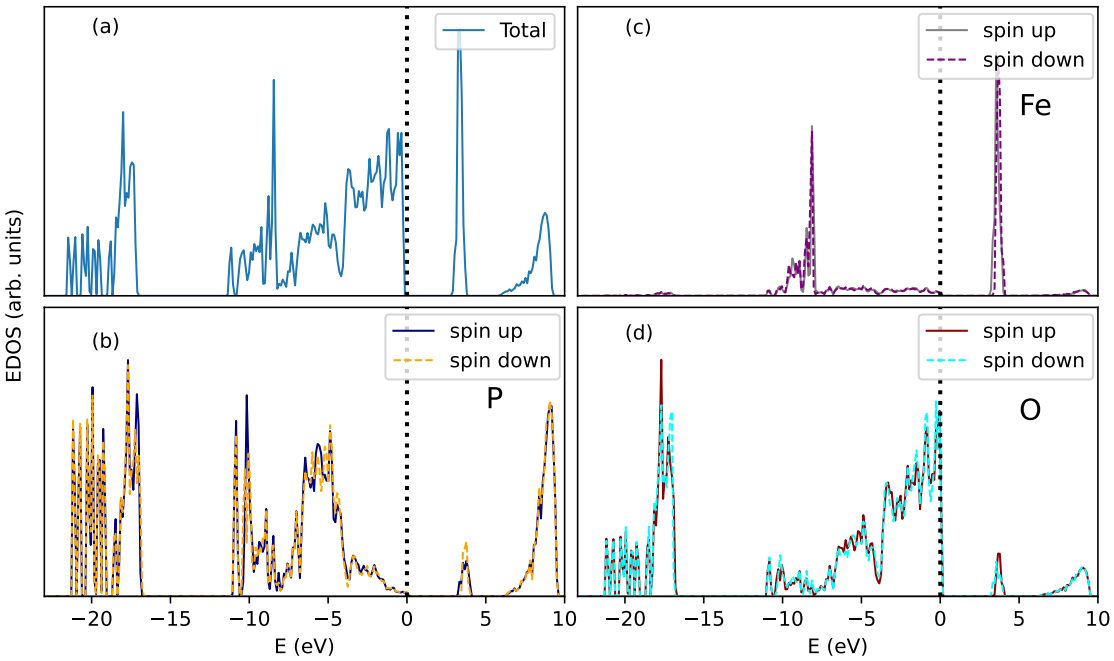

Fig. 5.4. The total and partial electronic density of states of iron pyrophosphate. The Fermi level (dotted line) was set to zero.

Within the range spanning from -12 eV to E_F, the Fe(3*d*) states exhibit hybridization with the O(2*p*) states, the latter prevailing in the energy vicinity of E_F. The O(2*s*) states are localized within the energy bracket of -22 to -17 eV. In the vacant bands situated above the forbidden gap, a minor contribution stemming from oxygen *s* and *p* states becomes discernible. Additionally, the 3*p* states inherent to the phosphorus atoms remain occupied within the energy span from -11 eV to E_F, accompanied by an extra peak discernible around -11 eV. The slender bands below -17 eV primarily accommodate the P(3*s*) states.

It is noteworthy to observe that the electronic density of states for oxygen and phosphorus atoms exhibits a similar pattern within the iron pyrophosphate structure as observed in the previously investigated copper pyrophosphate configuration. The

obtained insulating gap is smaller than in copper pyrophosphate, probably due to weaker electron correlations on Fe atoms. However, we are not aware of any measurements of the optical gap in iron pyrophosphate, and the calculated gap cannot be compared with the experimental data.

5.4 Dynamical properties

In this section, we will explore the lattice dynamical properties of iron pyrophosphate. Fig. 5.5(a) illustrates the phonon dispersion curves, which have been calculated using the harmonic approximation. These curves provide valuable insights into how phonon energies are distributed across the Brillouin zone. Due to a large size of the primitive cell, containing 124 atoms, the phonon spectrum consists of 372 dispersion curves. With the exception of four phonon modes near the *Y* and *C* points, all frequencies are found to be real. Notably, the lowest soft mode occurs at the Y point. Those phonons exhibiting imaginary frequencies are represented in the plots with negative values, signifying their unique behavior within the lattice dynamics of iron pyrophosphate.

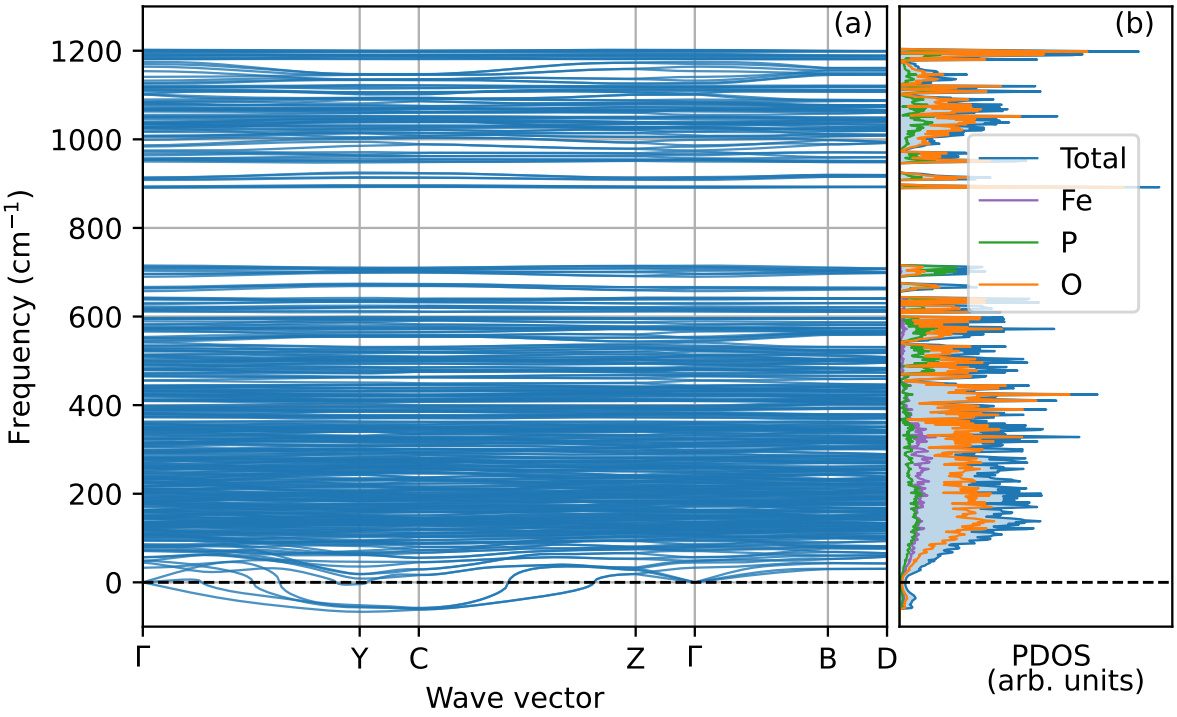

Fig. 5.5. a) The phonon dispersion relations and b) the total and partial element-projected PDOS in $Fe_4(P_2O_7)_3$.

In Fig. 5.5(b), we present the total PDOS alongside the individual contributions

from Fe, O, and P vibrations. Within the low-frequency range, the phonon states are primarily governed by O vibrations, with relatively smaller contributions from Fe and P atoms. Moving to the middle portion of the figure (600-750 cm^{-1}), three distinct bands emerge. Within the 600-700 cm^{-1} range, the vibrational modes of oxygen atoms dominate. In the band around 720 cm^{-1}, we observe the prevalence of vibrational modes associated with phosphorous atoms. At the highest frequencies (approximately 900-1200 cm^{-1}), an increased density of O atom vibrations is evident, while P atom vibrations are slightly smaller in comparison. In the soft modes (below 0 cm^{-1}), we observe a pronounced predominance of contributions from oxygen atoms, with notably smaller contributions from iron and phosphorous atoms.

5.5 Structural instability

The dynamic investigation has unveiled several soft modes, indicative of structural instability within iron pyrophosphate. To identify the specific atoms or groups responsible for this instability, we have analyzed atomic displacements induced by the lowest soft mode found at the Y point of the Brillouin zone. This analysis led to the identification of three distinct types of oxygen displacements in the P-O-P bridges, as illustrated in Fig. 5.6.

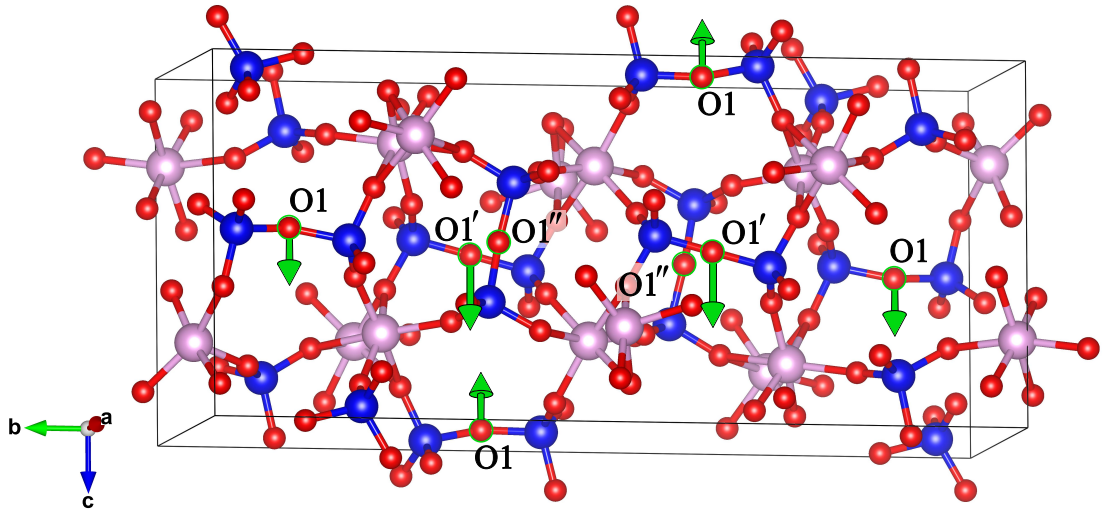

Fig. 5.6. The crystal structure of $Fe_4(P_2O_7)_3$ and schematic representation of three type of oxygen displacements (O1, O1′, O1") indicated by green arrows in the soft mode.

Notably, in the P-O1-P bridge with the angle of 148.2°, only minor displacements along the c-direction were observed. In contrast, the P-O1′-P bridge, characterized by

an angle of 179.81°, exhibited considerably larger displacements in the same direction. The third type of displacement in the P-O1"-P bridge was found to be minimal, indicating its relative stability. These vibrational patterns of oxygen atoms within the P-O-P bridges suggest the possibility of a structural phase transition at low temperatures. The soft mode at the Y point with the wave vector $q = (0.5, 0, 0)$ and transverse vibrations of oxygen atoms could induce the doubling of the unit cell along the a direction. However, the absence of experimental analysis within the low-temperature range hinders the confirmation of this hypothesis at present.

5.6 Summary

In conclusion, the investigation into the properties of $Fe_4(P_2O_7)_3$ has provided valuable insights into its structural, electronic, and dynamical characteristics. The calculations performed within the context of three distinct antiferromagnetic configurations have yielded significant findings. By employing the DFT+U technique with appropriate parameters for Fe and O atoms, the electronic band gap was determined to be $E_g = 2.57$ eV, and the AFM ground state was found to closely match the experimental observations.

The crystal structure analysis revealed the presence of interconnected double octahedrons of iron ions, coordinated by terminal oxygen atoms from diphosphate groups. The obtained lattice parameters, iron-iron separations, and bond angles exhibited good agreement with experimental data, validating the accuracy of the computational approach. Moreover, the investigation highlighted the presence of three distinct forms of crystallographically non-equivalent diphosphate groups, each contributing to the overall structural stability of $Fe_4(P_2O_7)_3$.

The electronic properties investigation showcased a significant exchange splitting within the Fe($3d$) states, contributing to the magnetic behavior of the compound. The calculated magnetic moment for iron closely matched experimental observations, further confirming the reliability of the theoretical approach. The electronic band structure exhibited an insulating state with a band gap of 2.57 eV, indicating the compound's potential for various electronic and optical applications.

Furthermore, the phonon dispersion curves were investigated unveiling the presence of soft modes. The large size of the primitive cell, housing 124 atoms, resulted in a phonon spectrum of 372 dispersion curves. The dominance of O vibrations in the low-frequency range, along with the emergence of distinct vibrational bands associated with specific atoms at higher frequencies, further enriches our understanding of the compound's dynamic behavior. The identification of the lowest soft mode at

the Y point and the analysis of the atomic displacements associated with the P-O-P bridges indicate a possibility of the structural phase transition at low temperatures.

Conclusions

In conclusion, this thesis aimed to comprehensively investigate the physical properties of metal ion pyrophosphates through *ab initio* calculations, shedding light on their unique characteristics for specific applications. The focus was placed on both copper and iron pyrophosphates due to their intriguing properties and potential applications.

The study of α-$Cu_2P_2O_7$ illuminated its intricate dynamics and thermal expansion behavior. By integrating local Coulomb interactions and van der Waals corrections into the calculations, remarkable agreement between theory and experiment was achieved. The antiferromagnetic arrangement of magnetic moments on copper atoms was confirmed to yield the lowest total energy, aligning with experimental observations. Dynamical stability at low temperatures was confirmed through phonon dispersion curves and phonon density of states analysis. The calculated phonon frequencies matched well with Raman spectroscopy measurements conducted on both single crystals and nanocrystals embedded in mesopores, validating the theoretical insights. Anharmonic properties of the α phase were also explored, contributing to an in-depth understanding of its distinct characteristics, including its strong negative thermal expansion behavior.

The investigation extended to the β phase of copper pyrophosphate revealed the importance of the dynamical instability at low temperatures attributed to a soft mode discovered in the phonon dispersion relations. This soft mode drives the structural phase transition from the high-temperature β to the low-temperature α phase and plays a pivotal role in the negative thermal expansion observed in copper pyrophosphate materials. The strong anharmonicity of the soft mode and its correlation with the NTE behavior were highlighted, providing valuable insights into the structural phase transition.

The investigation into $Fe_4(P_2O_7)_3$ yielded profound insights into its electronic, structural, and dynamical traits. Through comprehensive electronic band structure calculations and detailed analysis of its crystal structure, this study established a clear connection between theory and experiment. The calculated crystallographic parame-

ters and magnetic moments exhibit good agreement with experimental observations, showcasing the predictive power of the theoretical approach. The identification of distinct diphosphate groups and their contributions to structural stability deepened the understanding of the compound's architecture.

Both studied pyrophosphates exhibit electronic characteristics typical for Mott insulators. This designation is primarily due to their energy gap dependency on the parameter U. Concerning the magnetic properties, the antiferromagnetic ground state with magnetic moments localized on transition metal ions was found in both compounds. However, a notable distinction arises between these two materials, namely, the Néel temperature, which is approximately two times higher in iron pyrophosphate, indicating stronger magnetic interactions within the $Fe_4(P_2O_7)_3$ compound. Furthermore, both materials manifest a structural instability related to the dynamics of P_2O_7 groups, especially the vibrations of central oxygen atoms in the P-O-P bridges. In the case of copper pyrophosphate, this instability becomes pronounced at elevated temperatures, driving the α-β phase transition. In contrast, the calculations for iron pyrophosphate point towards a phase transition occurring at a lower temperature regime. Unfortunately, the lack of diffraction measurements at low temperatures hampers our ability to conclusively verify this prediction.

This thesis fulfilled its general aim by delving into the unique characteristics of metal ion pyrophosphates, exemplified through the cases of α and β phases of copper pyrophosphate and iron pyrophosphate. The comprehensive insights gained through *ab initio* calculations have not only enriched the understanding of these materials' physical properties but also paved the way for potential applications in various fields. Specifically, the electronic properties of copper and iron pyrophosphates demonstrate promise in the realms of electronic devices, semiconductors, energy systems, sensors, and advanced materials. Further research is indispensable to delve into their suitability for high-pressure physics and advanced devices. Meanwhile, the magnetic properties of iron pyrophosphate may find utility in data storage, sensors, industrial materials, and may have implications for medical technology and energy conversion. This research has underscored the interplay between structure, dynamics, and functionality in these compounds, advancing the realm of materials science and providing a solid foundation for further exploration and utilization of metal ion pyrophosphates.

Appendix

In this Appendix, a brief overview of synthesis method of materials used in Sections 4.1.2 and 4.1.5 for the comparison with the theoretical studies will be presented. The performed calculations for α-$Cu_2P_2O_7$ were compared with the experimental studies on copper pyrophosphate nanocrystals [50].

The fabrication of homogeneous and well-separated few nanometer sized crystals of $Cu_2P_2O_7$ is a challenging task, while most experimental studies concentrate on the synthesis of bulk form of such material. In order to perform a meaningful comparison of theoretical data with the experiment results, the new synthesis route was used [157], which allows for obtaining of copper pyrophosphate nanocrystals inside SBA-15 silica mesochannels.

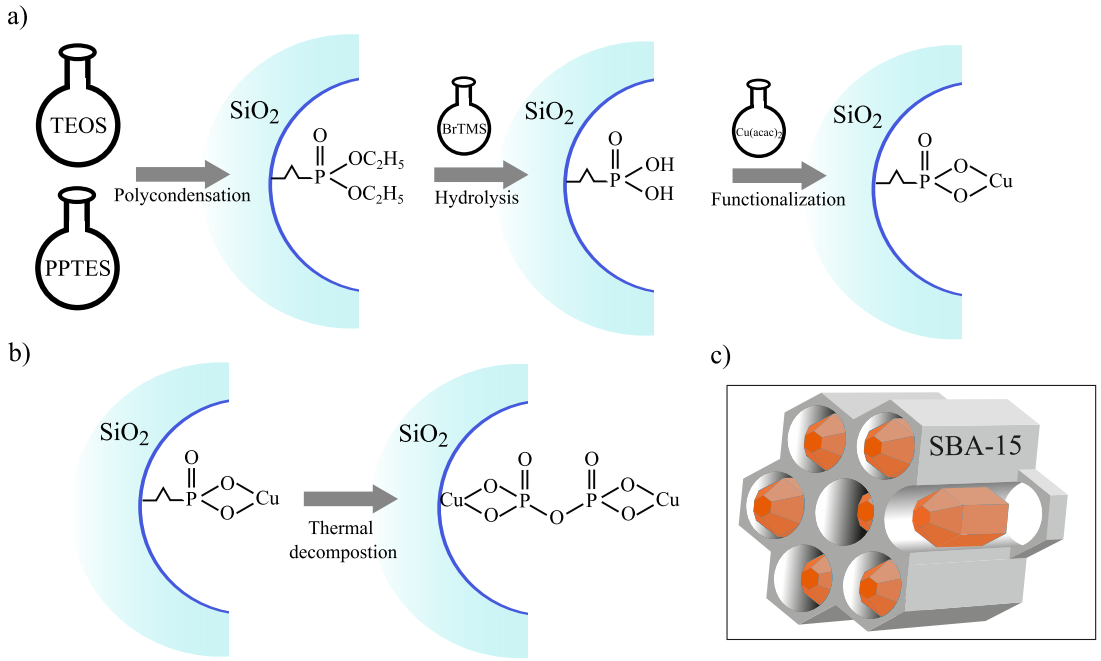

Fig. 5.7. Schematic representation of $Cu_2P_2O_7$ nanocrystals synthesis process: a) synthesis of initial structure with copper phosphonate units, b) thermal decomposition with copper pyrophosphate formation, c) visualization of nanocrystals inside SBA-15 silica.

The nanocrystal fabrication in silica nanoreactors is based on the functionalization of the SBA-15 mesoporous silica with selected functionalities and further their thermal decomposition, which causes the formation of desired material. The silica channels in this case play the role of nanoreactors, in which nanocrystals are created and cause the significant spatial confinement of grown crystallites preventing their diameter to be larger than silica channel size. The synthesis procedure of final

material consists of two stages, the synthesis of SBA-15 mesoporous silica possessing propyl copper phosphonate units inside the pores and thermal decomposition of above functionalities, leading to the formation of copper pyrophosphate nanocrystals. The schematic representation of such method is shown in Fig. 5.7.

The material from the first synthesis stage was prepared according to the direct-synthesis route [13, 14], which is based on the co-condensation of tetraethyl orthosilicate (TEOS) and propyl phosphonate dietyltriethoxysilane (PPTES) in the presence of triblock copolymer Pluronic P123 as the structuring agent under acidic conditions. Further material was hydrolyzed with the use of bromotrimethylsilane (BrTMS) and functionalized with $Cu(acac)_2$ units to obtain the proper functional groups inside silica channels. Finally, the formation of copper pyrophosphate nanocrystals (second synthesis stage) were done using calcination of initially synthesized material at temperature 350°C.

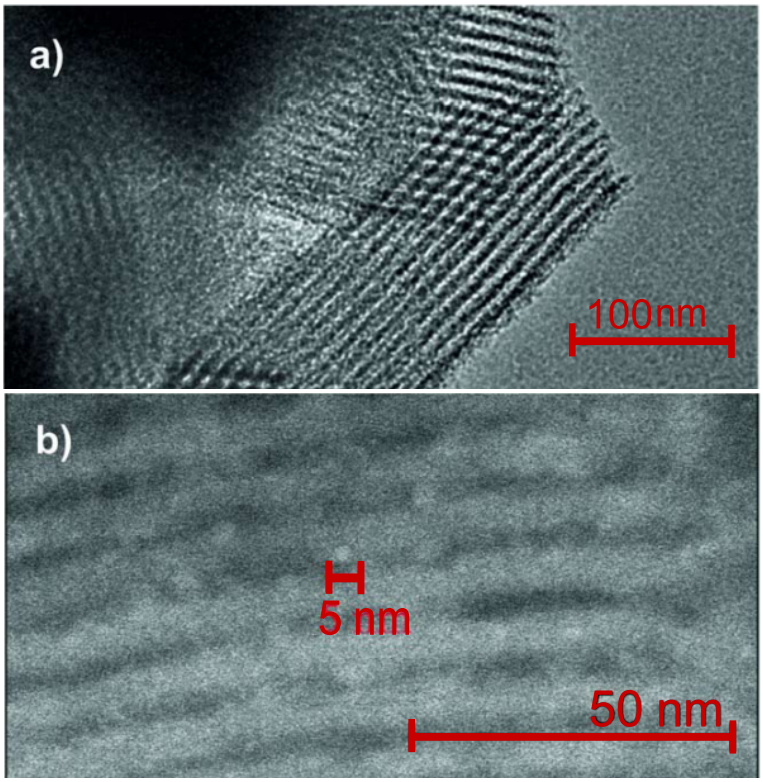

Fig. 5.8. TEM image of SBA-15 silica structure activated by copper phosphonate groups (a) and copper pyrophosphate nanocrystals inside the silica pores (b)

The performed transmission electron microscopy of synthesized sample confirms the formation of nanocrystals inside the silica SBA-15 pores (Fig. 5.8). The obtained structures of copper pyrophosphate have a spherical shape and a diameter of 5 nm, which is consistent with the pore size of SBA-15 matrix.

The synthesis of copper pyrophosphate inside the SBA-15 silica pores was per-

formed at the Institute of Nuclear Physics Polish Academy of Science, Department of Molecular Engineering and Nanoelectronics (Cracow, Poland). The TEM measurements and diffraction analysis were done at the Institute of Earth Sciences, University of Silesia, Faculty of Natural Sciences (Sosnowiec, Poland). The Raman spectroscopy study was carried out at the Institute of Materials Engineering, University of Silesia, and Silesian Center for Education and Interdisciplinary Research (Chorzów, Poland).

Scientific achievements

List of publications

Publications During Ph.D. School

- **S. Pastukh**, P. T. Jochym, O. Pastukh, J. Łażewski, D. Legut, P. Piekarz "Anharmonicity and structural phase transition in the Mott insulator $Cu_2P_2O_7$" Phys. Rev. B, 2023, 108, 104104. DOI: 10.1103/PhysRevB.108.104104

- O. Pastukh, M. Kąc, **S. Pastukh**, D. Kuźma, M. Zelent, M. Krawczyk, Ł. Laskowski "Magnetic Behavior of the Arrays of Iron Cylindrical Nanostructures: Atomistic Spin Model Simulations" Crystals 2023, 13(3), 537. DOI:10.3390/cryst13030537

- O. Pastukh, D. Kuźma, **S. Pastukh** "Simulations of Temperature-Dependent Magnetization in Fe_xGd_{100x}(20 x 80) Alloys", Magnetism 2023, 3(1), 34-44. DOI:10.3390/magnetism3010004

- **S. Pastukh**, M. Laskowska, M. Dulski, T. Krzykawski, K. Parlinski, P. Piekarz "Ab initio studies for characterization and identification of nanocrystalline copper pyrophosphate confined in mesoporous silica" Nanotechnology 2021, 32(41), 415701. DOI:10.1088/1361-6528/ac10e5

Publications Before Ph.D. School

- T.P. Zemła, K.M. Szczęśniak, A.Z. Kaczmarek, **S. Turchuk**, "Characterization of the superconducting phase in tellurium hydride at high pressure" Modern Physics Letters B, 33.16 (2019): 1950169. DOI:10.1142/S0217984919501690

- D. Szczęśniak, A. Z. Kaczmarek, R. Szczęśniak, **S. Turchuk**, Hengli Zhao, and E. A. Drzazga. "Superconducting properties of under-and over-doped $Ba_xK_{1-x}BiO_3$ perovskite oxide." Modern Physics Letters B 32, no. 16 (2018): 1850174. DOI:10.1142/S0217984918501749

Scientific internships

- NAWA STER program - internalization of doctoral school by implementing the project: "Experimental and ab initio studies of iron pyrophosphates inside silica nanoreactors" at the Karlsruhe Institute of Technology (KIT) in Germany (01.04.2022-30.04.2022).

- NAWA STER program - internalization of doctoral school by implementing the project: Investigation of the negative thermal expansion of the copper pyrophosphate lattice in IT4Innovations National Supercomputing Center at VSB Technical University of Ostrava (15.11.2022-15.12.2022).

- NAWA PROM program - internationalization of doctoral schools by implementing the project: First principle studies of transition metal phosphates in Advanced Technologies Research Institute (ATRI), Trnava, Slovakia (20.03.2023-24.03.2023).

Conferences

- New challenges for Polish science, CREATIVETIME, Gdańsk, 5-9 September 2020, oral session, "Obliczenia ab initio własności strukturalnych i dynamicznych pirofosforanu miedzi".

- 2nd International Online-Conference on Nanomaterials, 15-30 November 2020, poster session, "Ab initio calculations of the structural and dynamical properties of copper pyrophosphate "

- The Joint European Magnetic Symposia 2020, Portugal, Lisbon, 7-11 December 2020, poster session, "Crystal structure and magnetic properties of metal pyrophosphate materials $Fe_4(P_2O_7)_3$ and $Cu_4(P_2O_9)_2$"

- YOUNG MULTIS - Multiscale Phenomena in Condensed Matter - conference for young researchers, 5-7 July 2021, oral session, "Ab initio calculations for the alpha phase of cooper pyrophosphate".

- DyProSo 2021 (38th International Symposium on the Dynamical Properties of Solids) Luxemburg, 6-8 September 2021, oral session, "Structural and dynamical characterization of copper pyrophosphate".

- XI International conference Relaxed, nonlinear and acoustic optical processes and materials RNAOPM, Lutsk Ukraine, 1-5 June 2022, oral session, Ab initio methods for investigation of crystal structures and dynamical properties of phosphate materials (invited speaker)

- Multiscale Phenomena in Condensed matter Multis, Cracow, 27-30 June 2022, oral session, Investigation of electronic and magnetic properties of copper pyrophosphate.

- Joint Meeting of PSRS Members and SOLARIS Centre Users, Cracow, 20-23 September 2022, poster session, Manganese oxide nanoparticles obtained through the thermal decomposition of Mn12 SMMs as prospective multifunctional material.
- Recent Progress in Ab initio phonon calculations, Cracow, Poland (IFJ PAN), 9 May 2023, oral session, Mechanism of the structural phase transition in the Mott insulator $Cu_2P_2O_7$

Organizing activity

- 5th workshop on ab initio phonon calculations, Cracow, Poland, 3-6 December 2019. (member of organizing committee)
- Recent Progress in Ab initio phonon calculations, Cracow, Poland (IFJ PAN), 9 May 2023 (member of organizing committee)

Science popularization efforts

- Support in creating tasks for the game "Understanding Physics" implemented as part of the project "Physics as the key to understanding the world" (30.08.2021)
- Preparation of experiences presented during Children's Day with IFJ PAN (01.06.2021)
- Participation in the Małopolska Researchers' Night, preparation of experiments presented during the MRN (24.09.2021)
- Support in the implementation of the project "Physics as the key to understanding the world" (member of the competition committee and presenter during the settlement of the competition)(1.05.2022 - 30.06.2022)
- Preparation of experiences presented during Children's Day with IFJ PAN (01.06.2022)
- Participation in the Małopolska Researchers' Night, Young Engineer Workshop (30.09.2022)
- Support in the implementation of the "Enchanted with Physics" competition as part of the project "Physics as the key to understanding the world" (member of the competition committee and presenter during the settlement of the competition) (01.02.2023 - 20.02.2023)
- Support in the implementation of popular science shows "Exciting Physics" as part of the project "Physics as the key to understanding the world" edition 2 (30.05.2023 - 06.06.2023)

- Assistance in the implementation of workshops for children as part of the "Young Scientist's Tent" project (17.07.2023 - 04.08.2023)
- Participation in the Małopolska Researchers' Night, Young Engineer Workshop (29.09.2023)

Bibliography

[1] F. H. Westheimer, "Why nature chose phosphates," Science, vol. 235, no. 4793, pp. 1173–1178, 1987.

[2] S. C. Kamerlin, P. K. Sharma, R. B. Prasad, and A. Warshel, "Why nature really chose phosphate," Quarterly Reviews of Biophysics, vol. 46, no. 1, pp. 1–132, 2013.

[3] S. Ameen and M. S. Akhtar, "Introductory chapter: An overview of phosphate mineral and electrochemical detection of phosphate for environmental remediation," Functional Phosphate Materials and Their Applications, 2023.

[4] S. Minchin and J. Lodge, "Understanding biochemistry: structure and function of nucleic acids," Essays in Biochemistry, vol. 63, no. 4, pp. 433–456, 2019.

[5] J. Dunn and M. H. Grider, "Physiology, adenosine triphosphate," in StatPearls [internet], StatPearls Publishing, 2022.

[6] T. Hunter, "Why nature chose phosphate to modify proteins," Philosophical Transactions of the Royal Society B: Biological Sciences, vol. 367, no. 1602, pp. 2513–2516, 2012.

[7] H. Zhao and Z.-Y. Yuan, "Insights into transition metal phosphate materials for efficient electrocatalysis," ChemCatChem, vol. 12, no. 15, pp. 3797–3810, 2020.

[8] H. Yu, H. Yang, E. Shi, and W. Tang, "Development and clinical application of phosphorus-containing drugs," Medicine in Drug Discovery, vol. 8, p. 100063, 2020.

[9] T. J. Greenfield, M. Julve, and R. P. Doyle, "Exploring the biological, catalytic, and magnetic properties of transition metal coordination complexes incorporating pyrophosphate," Coordination Chemistry Reviews, vol. 384, pp. 37–64, 2019.

[10] A. Rabenau, "The role of hydrothermal synthesis in preparative chemistry," Angewandte Chemie International Edition in English, vol. 24, no. 12, pp. 1026–1040, 1985.

[11] H. Schmalzried, "Solid state reactions," 1981.

[12] O. Kaygili, "Synthesis and characterization of paramagnetic mn doped $Ca_2P_2O_7$ ceramics by sol-gel method," Journal of Ceramic Processing Research, vol. 16, pp. 54–58, 2015.

[13] L. Laskowski, M. Laskowska, J. Jelonkiewicz, M. Dulski, M. Wojtyniak, M. Fitta, and M. Balanda, "SBA-15 mesoporous silica free-standing thin films containing copper ions bounded via propyl phosphonate units-preparation and characterization," Journal of Solid State Chemistry, vol. 241, pp. 143–151, 2016.

[14] M. Laskowska, M. Oyama, I. Kityk, M. Marszalek, M. Dulski, and L. Laskowski, "Surface functionalization by silver-containing molecules with controlled distribution of functionalities," Applied Surface Science, vol. 481, pp. 433–436, 2019.

[15] M. Laskowska, I. Kityk, O. Pastukh, M. Dulski, M. Zubko, J. Jedryka, K. Cpałka, P. M. Zieliński, and Ł. Laskowski, "Nanocomposite for photonicsnickel pyrophosphate nanocrystals synthesised in silica nanoreactors," Microporous and Mesoporous Materials, vol. 306, p. 110435, 2020.

[16] R. Mahajan and R. Prakash, "A review report on structural and optical characterization of rare earth/transition metal doped pyrophosphate phosphors," Journal of Materials Science: Materials in Electronics, vol. 33, no. 34, pp. 25491–25517, 2022.

[17] Y. Jin, Y. Shen, and T. Hibino, "Proton conduction in metal pyrophosphates (MP_2O_7) at intermediate temperatures," Journal of Materials Chemistry, vol. 20, no. 30, pp. 6214–6217, 2010.

[18] M. Nagao, A. Takeuchi, P. Heo, T. Hibino, M. Sano, and A. Tomita, "A proton-conducting In3+-doped SnP_2O_7 electrolyte for intermediate-temperature fuel cells," Electrochemical and Solid-State Letters, vol. 9, no. 3, p. A105, 2006.

[19] S. S. Patil and P. S. Patil, "Transition metal pyrophosphate ($M_xP_2O_7$): A new arrival in hybrid supercapacitors," Chemical Engineering Journal, vol. 455, p. 140639, 2023.

[20] Z. Khan, B. Senthilkumar, S. Lim, R. Shanker, Y. Kim, and H. Ko, "Redox-additive-enhanced high capacitance supercapacitors based on $Co_2P_2O_7$ nanosheets," Advanced Materials Interfaces, vol. 4, no. 12, p. 1700059, 2017.

[21] C. Wei, S. Yang, W. Liu, X. Hou, Y. Sun, J. Zhao, W. Xiong, C. Cheng, and D. Zhang, "Hierarchically porous bowknot-like sodium doped $Ni_2P_2O_7$-$Co_2P_2O_7$ with improved supercapacitor performances," Applied Surface Science, vol. 465, pp. 763–771, 2019.

[22] H. Pang, Y.-Z. Zhang, Z. Run, W.-Y. Lai, and W. Huang, "Amorphous nickel pyrophosphate microstructures for high-performance flexible solid-state electrochemical energy storage devices," Nano Energy, vol. 17, pp. 339–347, 2015.

[23] P. Barpanda, S.-i. Nishimura, and A. Yamada, "High-voltage pyrophosphate cathodes," Advanced Energy Materials, vol. 2, no. 7, pp. 841–859, 2012.

[24] S.-i. Nishimura, M. Nakamura, R. Natsui, and A. Yamada, "New lithium iron pyrophosphate as 3.5 v class cathode material for lithium ion battery," Journal of the American Chemical Society, vol. 132, no. 39, pp. 13596–13597, 2010.

[25] L. Adam, A. Guesdon, and B. Raveau, "A new lithium manganese phosphate with an original tunnel structure in the $A_2MP_2O_7$ family," Journal of Solid State Chemistry, vol. 181, no. 11, pp. 3110–3115, 2008.

[26] N. Kosova, A. Tsapina, A. Slobodyuk, and S. Petrov, "Structure and electrochemical properties of mixed transition-metal pyrophosphates $Li_2Fe_{1-y}Mn_yP_2O_7$ (0 y 1)," Electrochimica Acta, vol. 174, pp. 1278–1289, 2015.

[27] G. Mestl, D. Lesser, and T. Turek, "Optimum performance of vanadyl pyrophosphate catalysts," Topics in Catalysis, vol. 59, pp. 1533–1544, 2016.

[28] T. Kasuga, "Bioactive calcium pyrophosphate glasses and glass-ceramics," Acta Biomaterialia, vol. 1, no. 1, pp. 55–64, 2005.

[29] S. R. Vasant and M. Joshi, "A review on calcium pyrophosphate and other related phosphate nano bio-materials and their applications.," Reviews on Advanced Materials Science, vol. 49, no. 1, 2017.

[30] J. E. Kostka, G. W. Luther III, and K. H. Nealson, "Chemical and biological reduction of Mn (iii)-pyrophosphate complexes: potential importance of dissolved Mn (iii) as an environmental oxidant," Geochimica et Cosmochimica Acta, vol. 59, no. 5, pp. 885–894, 1995.

[31] A. E. Hoffman, M. DeStefano, C. Shoen, K. Gopinath, D. F. Warner, M. Cynamon, and R. P. Doyle, "Co (ii) and Cu (ii) pyrophosphate complexes have selectivity and potency against mycobacteria including mycobacterium tuberculosis," European Journal of Medicinal Chemistry, vol. 70, pp. 589–593, 2013.

[32] O. F. Ikotun, E. M. Higbee, W. Ouellette, and R. P. Doyle, "Pyrophosphate-bridged complexes with picomolar toxicity," Journal of Inorganic Biochemistry, vol. 103, no. 9, pp. 1254–1264, 2009.

[33] S. Sabiah, B. Varghese, and N. N. Murthy, "First hexanuclear copper (ii) pyrophosphate through hydrolysis of phosphodiester with a dicopper complex," Chemical Communications, no. 37, pp. 5636–5638, 2009.

[34] J. Mathew, "Studies on the properties of certain nanocrystalline metal phosphates," Thesis submitted to the Mahatma Gandhi University, pp. 1–202, 2005.

[35] O. E. Schupp III, P. E. Sturrock, and J. I. Watters, "A study of the stability and basicity of the copper (ii) pyrophosphate complexes using the dropping amalgam electrode," Inorganic Chemistry, vol. 2, no. 1, pp. 106–112, 1963.

[36] S.-N. Le, A. Navrotsky, and V. Pralong, "Energetics of copper diphosphates–$Cu_2P_2O_7$ and $Cu_3(P_2O_6OH)_2$," Solid State Sciences, vol. 10, no. 6, pp. 761–767, 2008.

[37] K. L. Meganathan, R. BoopathiRaja, M. Parthibavarman, V. Sharmila, M. Shkir, S. A. Gaikwad, and M. Praveenkumar, "Design and fabrication of $Cu_2P_2O_7$@Ppy electrode for extraordinary capacitance and long-term stability for ideal asymmetric supercapacitor application," Journal of Materials Science: Materials in Electronics, vol. 32, pp. 24736–24747, Oct 2021.

[38] A. Agarwal and B. R. Sankapal, "Ultrathin $Cu_2P_2O_7$ nanoflakes on stainless steel substrate for flexible symmetric all-solid-state supercapacitors," Chemical Engineering Journal, vol. 422, p. 130131, 2021.

[39] A. Agarwal, S. Majumder, and B. R. Sankapal, "Multi-walled carbon nanotubes supported copper phosphate microflowers for flexible solid-state supercapacitor," International Journal of Energy Research, vol. 46, no. 5, pp. 6177–6196, 2022.

[40] O. In-noi, P. Daorattanachai, C. Rungnim, K. Prasitnok, B. Rungtaweevoranit, K. Faungnawakij, and P. Khemthong, "Insight into fructose dehydration over lewis acid α-$Cu_2P_2O_7$ catalyst," ChemNanoMat, vol. 7, no. 3, pp. 292–298, 2021.

[41] J. Sang, P. Wei, T. Liu, H. Lv, X. Ni, D. Gao, J. Zhang, H. Li, Y. Zang, F. Yang, Z. Liu, G. Wang, and X. Bao, "A reconstructed $Cu_2P_2O_7$ catalyst for selective CO_2 electroreduction to multicarbon products," Angewandte Chemie International Edition, vol. 61, no. 5, p. e202114238, 2022.

[42] T. Akiyama, M. Shimakawa, and S. Takenaka, "Superior performance of copper phosphate -$Cu_2P_2O_7$ catalysts for partial oxidation of methane into formaldehyde," Chemistry Letters, vol. 51, no. 5, pp. 511–514, 2022.

[43] R. P. Sartoris, O. R. Nascimento, R. C. Santana, M. Perec, R. F. Baggio, and R. Calvo, "Structure and magnetism of a binuclear cu ii pyrophosphate: transition to a 3d magnetic behaviour studied by single crystal epr," Dalton Transactions, vol. 44, no. 10, pp. 4732–4743, 2015.

[44] B. E. Robertson and C. Calvo, "The crystal structure and phase transformation of α-$Cu_2P_2O_7$," Acta Crystallographica, vol. 22, no. 5, pp. 665–672, 1967.

[45] B. Robertson and C. Calvo, "Crystal structure of β-$Cu_2P_2O_7$," Canadian Journal of Chemistry, vol. 46, no. 4, pp. 605–612, 1968.

[46] K. Pogorzelec-Glaser, A. Pietraszko, B. Hilczer, and M. Połomska, "Structure and phase transitions in $Cu_2P_2O_7$," Phase Transitions, vol. 79, no. 6-7, p. 535, 2006.

[47] J. Stiles and C. Stager, "Magnetic structure of manganese pyrophosphate and copper pyrophosphate," Canadian Journal of Physics, vol. 50, no. 24, pp. 3079–3084, 1972.

[48] J. Stiles and C. Stager, "Nuclear magnetic resonance in antiferromagnetic $Cu_2P_2O_7$," Canadian Journal of Physics, vol. 51, no. 1, pp. 87–94, 1973.

[49] O. Janson, A. A. Tsirlin, J. Sichelschmidt, Y. Skourski, F. Weickert, and H. Rosner, "Long-range superexchange in $Cu_2A_2O_7$ (A= P, As, V) as a key element of the microscopic magnetic model," Physical Review B, vol. 83, p. 094435, Mar 2011.

[50] S. Pastukh, M. Laskowska, M. Dulski, T. Krzykawski, K. Parlinski, and P. Piekarz, "Ab initio studies for characterization and identification of nanocrystalline copper pyrophosphate confined in mesoporous silica," Nanotechnology, vol. 32, no. 41, p. 415701, 2021.

[51] N. Shi, A. Sanson, Q. Gao, Q. Sun, Y. Ren, Q. Huang, D. O. de Souza, X. Xing, and J. Chen, "Strong negative thermal expansion in a low-cost and facile oxide of $Cu_2P_2O_7$," Journal of the American Chemical Society, vol. 142, no. 6, pp. 3088–3093, 2020.

[52] X. Liu, Y. Xu, R. Jin, P. Yin, L. Sun, T. Liang, and S. Gao, "Facile synthesis of hierarchical $Fe_4(P_2O_7)_3$ for removal of U (VI)," Journal of Molecular Liquids, vol. 200, pp. 311–318, 2014.

[53] Q. Ma, Y. Sun, C. Zhang, Y. Xue, Y. Chen, W. Teng, and J. Fan, "Iron pyrophosphate doped carbon nanocomposite for tetracycline degradation by activation of peroxymonosulfate," New Journal of Chemistry, vol. 46, no. 37, pp. 17985–17994, 2022.

[54] A. Gupta, N. B. Amin, A. Besarab, S. E. Vogel, G. W. Divine, J. Yee, and J. Anandan, "Dialysate iron therapy: infusion of soluble ferric pyrophosphate via the dialysate during hemodialysis," Kidney International, vol. 55, no. 5, pp. 1891–1898, 1999.

[55] M. C. Fidler, T. Walczyk, L. Davidsson, C. Zeder, N. Sakaguchi, L. R. Juneja, and R. F. Hurrell, "A micronised, dispersible ferric pyrophosphate with high relative bioavailability in man," British Journal of Nutrition, vol. 91, no. 1, pp. 107–112, 2004.

[56] R. Trivedi and K. Barve, "Delivery systems for improving iron uptake in anemia," International Journal of Pharmaceutics, vol. 601, p. 120590, 2021.

[57] G.-H. Lee, Y. S. Kim, and D.-W. Kim, "Redox effect of Fe^{2+}/Fe^{3+} in iron phosphates for enhanced electrocatalytic activity in Li-O_2 batteries," Chemical Engineering Journal, vol. 388, p. 124294, 2020.

[58] Z. W. Xiao, G. R. Hu, Z. D. Peng, K. Du, and X. G. Gao, "Solid state synthesis and characterization of iron (ii) pyrophosphate $Fe_2P_2O_7$," Chinese Chemical Letters, vol. 18, no. 12, pp. 1525–1527, 2007.

[59] L. Zhang and R. K. Brow, "A raman study of ironphosphate crystalline compounds and glasses," Journal of the American Ceramic Society, vol. 94, no. 9, pp. 3123–3130, 2011.

[60] W. M. Reiff and C. C. Torardi, "Synthetic iron iii phosphates: Topotactic transformation of $Fe_2(P_2O_7)(HPO_4)$ to $Fe_4(P_2O_7)_3$, a more condensed magnetic structure," Hyperfine Interactions, vol. 53, pp. 403–408, Jul 1990.

[61] L. Elbouaanani, B. Malaman, R. Gérardin, and M. Ijjaali, "Crystal structure refinement and magnetic properties of $Fe_4(P_2O_7)_3$ studied by neutron diffraction and mössbauer techniques," Journal of Solid State Chemistry, vol. 163, no. 2, pp. 412–420, 2002.

[62] M. Born and R. Oppenheimer, "On the quantum theory of molecules," in Quantum Chemistry: Classic Scientific Papers, pp. 1–24, World Scientific, 2000.

[63] P. Hohenberg and W. Kohn, "Density functional theory (dft)," Physical Review, vol. 136, p. B864, 1964.

[64] W. Kohn and L. J. Sham, "Self-consistent equations including exchange and correlation effects," Physical Review, vol. 140, no. 4A, p. A1133, 1965.

[65] D. M. Ceperley and B. J. Alder, "Ground state of the electron gas by a stochastic method," Physical Review Letters, vol. 45, no. 7, p. 566, 1980.

[66] J. P. Perdew and A. Zunger, "Self-interaction correction to density-functional approximations for many-electron systems," Physical Review B, vol. 23, no. 10, p. 5048, 1981.

[67] S. H. Vosko, L. Wilk, and M. Nusair, "Accurate spin-dependent electron liquid correlation energies for local spin density calculations: a critical analysis," Canadian Journal of Physics, vol. 58, no. 8, pp. 1200–1211, 1980.

[68] D. C. Langreth and M. Mehl, "Beyond the local-density approximation in calculations of ground-state electronic properties," Physical Review B, vol. 28, no. 4, p. 1809, 1983.

[69] J. P. Perdew and W. Yue, "Accurate and simple density functional for the electronic exchange energy: Generalized gradient approximation," Physical Review B, vol. 33, no. 12, p. 8800, 1986.

[70] A. D. Becke, "Density-functional exchange-energy approximation with correct asymptotic behavior," Physical Review A, vol. 38, no. 6, p. 3098, 1988.

[71] J. P. Perdew and Y. Wang, "Accurate and simple analytic representation of the electron-gas correlation energy," Physical Review B, vol. 45, no. 23, p. 13244, 1992.

[72] J. P. Perdew, J. A. Chevary, S. H. Vosko, K. A. Jackson, M. R. Pederson, D. J. Singh, and C. Fiolhais, "Atoms, molecules, solids, and surfaces: Applications of

the generalized gradient approximation for exchange and correlation," Physical Review B, vol. 46, no. 11, p. 6671, 1992.

[73] D. Vanderbilt, "Optimally smooth norm-conserving pseudopotentials," Physical Review B, vol. 32, no. 12, p. 8412, 1985.

[74] D. Vanderbilt, "Soft self-consistent pseudopotentials in a generalized eigenvalue formalism," Physical Review B, vol. 41, no. 11, p. 7892, 1990.

[75] S. Goedecker, M. Teter, and J. Hutter, "Separable dual-space gaussian pseudopotentials," Physical Review B, vol. 54, no. 3, p. 1703, 1996.

[76] P. E. Blöchl, "Projector augmented-wave method," Physical Review B, vol. 50, no. 24, p. 17953, 1994.

[77] H. J. Monkhorst and J. D. Pack, "Special points for brillouin-zone integrations," Physical Review B, vol. 13, no. 12, p. 5188, 1976.

[78] A. Jain, S. P. Ong, G. Hautier, W. Chen, W. D. Richards, S. Dacek, S. Cholia, D. Gunter, D. Skinner, G. Ceder, et al., "Commentary: The materials project: A materials genome approach to accelerating materials innovation," APL Materials, vol. 1, no. 1, p. 011002, 2013.

[79] G. Kresse and J. Furthmüller, "Efficient iterative schemes for ab initio total-energy calculations using a plane-wave basis set," Physical Review B, vol. 54, no. 16, p. 11169, 1996.

[80] G. Kresse and J. Furthmüller, "Efficiency of ab-initio total energy calculations for metals and semiconductors using a plane-wave basis set," Computational Materials Science, vol. 6, no. 1, pp. 15–50, 1996.

[81] P. Giannozzi, S. Baroni, N. Bonini, M. Calandra, R. Car, C. Cavazzoni, D. Ceresoli, G. L. Chiarotti, M. Cococcioni, I. Dabo, et al., "Quantum espresso: a modular and open-source software project for quantum simulations of materials," Journal of Physics: Condensed Matter, vol. 21, no. 39, p. 395502, 2009.

[82] F. D. Murnaghan, "The compressibility of media under extreme pressures," Proceedings of the National Academy of Sciences, vol. 30, no. 9, pp. 244–247, 1944.

[83] J. Hubbard, "Electron correlations in narrow energy bands," Proceedings of the Royal Society of London. Series A. Mathematical and Physical Sciences, vol. 276, no. 1365, pp. 238–257, 1963.

[84] V. I. Anisimov, J. Zaanen, and O. K. Andersen, "Band theory and mott insulators: Hubbard U instead of stoner I," Physical Review B, vol. 44, no. 3, p. 943, 1991.

[85] A. Liechtenstein, V. I. Anisimov, and J. Zaanen, "Density-functional theory and strong interactions: Orbital ordering in mott-hubbard insulators," Physical Review B, vol. 52, no. 8, p. R5467, 1995.

[86] V. I. Anisimov, F. Aryasetiawan, and A. Lichtenstein, "First-principles calculations of the electronic structure and spectra of strongly correlated systems: the LDA+U method," Journal of Physics: Condensed Matter, vol. 9, no. 4, p. 767, 1997.

[87] M. Cococcioni and S. de Gironcoli, "Linear response approach to the calculation of the effective interaction parameters in the LDA + U method," Physical Review B, vol. 71, p. 035105, Jan 2005.

[88] S. Grimme, "Accurate description of van der waals complexes by density functional theory including empirical corrections," Journal of Computational Chemistry, vol. 25, no. 12, pp. 1463–1473, 2004.

[89] S. Grimme, "Semiempirical gga-type density functional constructed with a long-range dispersion correction," Journal of Computational Chemistry, vol. 27, no. 15, p. 1787, 2006.

[90] S. Grimme, J. Antony, S. Ehrlich, and H. Krieg, "A consistent and accurate ab initio parametrization of density functional dispersion correction (DFT-D) for the 94 elements H-Pu," The Journal of Chemical Physics, vol. 132, no. 15, p. 154104, 2010.

[91] A. Tkatchenko, R. A. DiStasio Jr, R. Car, and M. Scheffler, "Accurate and efficient method for many-body van der waals interactions," Physical Review Letters, vol. 108, no. 23, p. 236402, 2012.

[92] K. Parlinski, Z. Q. Li, and Y. Kawazoe, "First-principles determination of the soft mode in cubic ZrO_2," Physical Review Letters, no. 78, p. 463, 1997.

[93] S. Baroni, S. De Gironcoli, A. Dal Corso, and P. Giannozzi, "Phonons and related crystal properties from density-functional perturbation theory," Reviews of Modern Physics, vol. 73, no. 2, p. 515, 2001.

[94] O. Hellman, P. Steneteg, I. A. Abrikosov, and S. I. Simak, "Temperature dependent effective potential method for accurate free energy calculations of solids," Physical Review B, vol. 87, no. 10, p. 104111, 2013.

[95] H. Hellmann et al., "Einfuhrung in die quantenchemie," 1937.

[96] R. P. Feynman, "Forces in molecules," Physical Review, vol. 56, no. 4, p. 340, 1939.

[97] K. Kunc and R. M. Martin, "Ab initio force constants of GaAs: A new approach to calculation of phonons and dielectric properties," Physical Review Letters, vol. 48, no. 6, p. 406, 1982.

[98] W. Frank, C. Elsässer, and M. Fähnle, "Ab initio force-constant method for phonon dispersions in alkali metals," Physical Review Letters, vol. 74, no. 10, p. 1791, 1995.

[99] G. Kresse, J. Furthmüller, and J. Hafner, "Ab initio force constant approach to phonon dispersion relations of diamond and graphite," Europhysics Letters, vol. 32, no. 9, p. 729, 1995.

[100] W. Zhong, R. King-Smith, and D. Vanderbilt, "Giant LO-TO splittings in perovskite ferroelectrics," Physical Review Letters, vol. 72, no. 22, p. 3618, 1994.

[101] R. M. Pick, M. H. Cohen, and R. M. Martin, "Microscopic theory of force constants in the adiabatic approximation," Physical Review B, vol. 1, pp. 910–920, Jan 1970.

[102] P. Umari, A. Pasquarello, and A. Dal Corso, "Raman scattering intensities in α-quartz: A first-principles investigation," Physical Review B, vol. 63, p. 094305, Feb 2001.

[103] A. Maradudin and A. Fein, "Scattering of neutrons by an anharmonic crystal," Physical Review, vol. 128, no. 6, p. 2589, 1962.

[104] S. Biernacki and M. Scheffler, "Negative thermal expansion of diamond and zinc-blende semiconductors," Physical Review Letters, vol. 63, no. 3, p. 290, 1989.

[105] D. Hooton, "The use of a model in anharmonic lattice dynamics," Philosophical Magazine, vol. 3, no. 25, pp. 49–54, 1958.

[106] N. R. Werthamer, "Self-consistent phonon formulation of anharmonic lattice dynamics," Physical Review B, vol. 1, pp. 572–581, Jan 1970.

[107] K. Parlinski, "Ab initio determination of anharmonic phonon peaks," Physical Review B, vol. 98, no. 5, p. 054305, 2018.

[108] J. Kang and L.-W. Wang, "First-principles green-kubo method for thermal conductivity calculations," Physical Review B, vol. 96, no. 2, p. 020302, 2017.

[109] A. A. Quong and A. Y. Liu, "First-principles calculations of the thermal expansion of metals," Physical Review B, vol. 56, no. 13, p. 7767, 1997.

[110] J. Xie, S. de Gironcoli, S. Baroni, and M. Scheffler, "First-principles calculation of the thermal properties of silver," Physical Review B, vol. 59, no. 2, p. 965, 1999.

[111] P. Piekarz, P. Jochym, K. Parlinski, and J. Łażewski, "High-pressure and thermal properties of γ-Mg_2SiO_4 from first-principles calculations," The Journal of Chemical Physics, vol. 117, no. 7, pp. 3340–3344, 2002.

[112] N. Christensen, D. Boers, J. van Velsen, and D. Novikov, "Negative thermal expansion coefficient and isostructural transition in fcc cesium," Physical Review B, vol. 61, no. 6, p. R3764, 2000.

[113] U. D. Wdowik, K. Parlinski, T. Chatterji, S. Rols, and H. Schober, "Lattice dynamics of rhenium trioxide from the quasiharmonic approximation," Physical Review B, vol. 82, no. 10, p. 104301, 2010.

[114] D. S. Kim, O. Hellman, J. Herriman, H. Smith, J. Lin, N. Shulumba, J. Niedziela, C. Li, D. Abernathy, and B. Fultz, "Nuclear quantum effect with pure anharmonicity and the anomalous thermal expansion of silicon," Proceedings of the National Academy of Sciences, vol. 115, no. 9, pp. 1992–1997, 2018.

[115] P. T. Jochym, R. K. Kremer, J. Łażewski, A. Ptok, P. Piekarz, E. Brücher, and A. M. Oleś, "Influence of anharmonicity on the negative thermal expansion of α-Sn," Physical Review Materials, vol. 6, no. 11, p. 113601, 2022.

[116] M. Sternik and K. Parlinski, "Ab initio calculations of the stability and lattice dynamics of the $MgSiO_3$ post-perovskite," Journal of Physics and Chemistry of Solids, vol. 67, no. 4, pp. 796–800, 2006.

[117] U. D. Wdowik, "Structural stability and thermal properties of BeO from the quasiharmonic approximation," Journal of Physics: Condensed Matter, vol. 22, no. 4, p. 045404, 2010.

[118] C. Malica and A. D. Corso, "Quasi-harmonic thermoelasticity of palladium, platinum, copper, and gold from first principles," Journal of Physics: Condensed Matter, vol. 33, p. 475901, sep 2021.

[119] O. Hellman, I. Abrikosov, and S. Simak, "Lattice dynamics of anharmonic solids from first principles," Physical Review B, vol. 84, no. 18, p. 180301, 2011.

[120] O. Hellman and I. A. Abrikosov, "Temperature-dependent effective third-order interatomic force constants from first principles," Physical Review B, vol. 88, no. 14, p. 144301, 2013.

[121] T. Tadano, Y. Gohda, and S. Tsuneyuki, "Anharmonic force constants extracted from first-principles molecular dynamics: applications to heat transfer simulations," Journal of Physics: Condensed Matter, vol. 26, no. 22, p. 225402, 2014.

[122] "https://ollehellman.github.io/,"

[123] Y. Oba, T. Tadano, R. Akashi, and S. Tsuneyuki, "First-principles study of phonon anharmonicity and negative thermal expansion in ScF_3," Physical Review Materials, vol. 3, no. 3, p. 033601, 2019.

[124] T. Tadano and S. Tsuneyuki, "Self-consistent phonon calculations of lattice dynamical properties in cubic $SrTiO_3$ with first-principles anharmonic force constants," Physical Review B, vol. 92, no. 5, p. 054301, 2015.

[125] T. Tadano and S. Tsuneyuki, "First-principles lattice dynamics method for strongly anharmonic crystals," Journal of the Physical Society of Japan, vol. 87, no. 4, p. 041015, 2018.

[126] P. Jochym and J. Łażewski, "High efficiency configuration space sampling–probing the distribution of available states," SciPost Physics, vol. 10, no. 6, p. 129, 2021.

[127] C. W. Li, O. Hellman, J. Ma, A. F. May, H. B. Cao, X. Chen, A. D. Christianson, G. Ehlers, D. J. Singh, B. C. Sales, and O. Delaire, "Phonon self-energy and origin of anomalous neutron scattering spectra in SnTe and PbTe thermoelectrics," Physical Review Letters, vol. 112, p. 175501, Apr 2014.

[128] N. Metropolis, A. W. Rosenbluth, M. N. Rosenbluth, A. H. Teller, and E. Teller, "Equation of State Calculations by Fast Computing Machines," The Journal of Chemical Physics, vol. 21, pp. 1087–1092, 12 2004.

[129] W. K. Hastings, "Monte carlo sampling methods using markov chains and their applications," Biometrika, vol. 57, no. 1, pp. 97–109, 1970.

[130] A. Ptok, A. Kobiałka, M. Sternik, J. Łażewski, P. T. Jochym, A. M. Oleś, S. Stankov, and P. Piekarz, "Chiral phonons in the honeycomb sublattice of layered CoSn-like compounds," Physical Review B, vol. 104, p. 054305, Aug 2021.

[131] A. Ptok, K. J. Kapcia, P. T. Jochym, J. Łażewski, A. M. Oleś, and P. Piekarz, "Electronic and dynamical properties of $CeRh_2As_2$: Role of Rh_2As_2 layers and expected orbital order," Physical Review B, vol. 104, p. L041109, Jul 2021.

[132] A. Ptok, A. Kobiałka, M. Sternik, J. Łażewski, P. T. Jochym, A. M. Oleś, and P. Piekarz, "Dynamical study of the origin of the charge density wave in AV_3Sb_5 ($A =$ K, Rb, Cs) compounds," Physical Review B, vol. 105, p. 235134, Jun 2022.

[133] J. P. Perdew, K. Burke, and M. Ernzerhof, "Generalized gradient approximation made simple," Physical Review Letters, vol. 77, no. 18, p. 3865, 1996.

[134] V. I. Anisimov, J. Zaanen, and O. K. Andersen, "Band theory and mott insulators: Hubbard U instead of stoner I," Physical Review B, vol. 44, p. 943, Jul 1991.

[135] A. Tkatchenko and M. Scheffler, "Accurate molecular van der waals interactions from ground-state electron density and free-atom reference data," Physical Review Letters, vol. 102, p. 073005, Feb 2009.

[136] T. Bučko, J. Hafner, S. Lebègue, and J. G. Ángyán, "Improved description of the structure of molecular and layered crystals: Ab initio dft calculations with van der waals corrections," The Journal of Chemical Physics A, vol. 114, p. 11814, 2010.

[137] T. Bučko, S. Lebègue, J. Hafner, and J. G. Ángyán, "Tkatchenko-scheffler van der waals correction method with and without self-consistent screening applied to solids," Physical Review B, vol. 87, p. 064110, Feb 2013.

[138] T. Bučko, S. Lebègue, J. G. Ángyán, and J. Hafner, "Extending the applicability of the tkatchenko-scheffler dispersion correction via iterative hirshfeld partitioning," The Journal of Chemical Physics, vol. 141, no. 3, p. 034114, 2014.

[139] K. Parlinski, Software PHONON 7.10, 2019.

[140] M. Gajdoš, K. Hummer, G. Kresse, J. Furthmüller, and F. Bechstedt, "Linear optical properties in the projector-augmented wave methodology," Physical Review B, vol. 73, p. 045112, Jan 2006.

[141] P. Umari, A. Pasquarello, and A. Dal Corso, "Raman scattering intensities in α-quartz: A first-principles investigation," Physical Review B, vol. 63, p. 094305, Feb 2001.

[142] K. Momma and F. Izumi, "Vesta 3 for three-dimensional visualization of crystal, volumetric and morphology data," Journal of Applied Crystallography, vol. 44, no. 6, p. 1272, 2011.

[143] X. Yang, P. Zhang, and P. Korzhavyi, "Hybrid-density functional calculations of structural, electronic, magnetic, and thermodynamic properties of α-$Cu_2P_2O_7$," Applied Sciences, vol. 13, no. 1, 2023.

[144] A. Majtyka-Piłat, M. Wojtyniak, Ł. Laskowski, and D. Chrobak, "Structure and properties of copper pyrophosphate by first-principle calculations," Materials, vol. 15, no. 3, p. 842, 2022.

[145] A. Karaphun, P. Chirawatkul, S. Maensiri, and E. Swatsitang, "Influence of calcination temperature on the structural, morphological, optical, magnetic and electrochemical properties of $Cu_2P_2O_7$ nanocrystals," Journal of Sol-Gel Science and Technology, vol. 88, pp. 407–421, Nov 2018.

[146] M. S. Hybertsen, M. Schlüter, and N. E. Christensen, "Calculation of coulomb-interaction parameters for La_2CuO_4 using a constrained-density-functional approach," Physical Review B, vol. 39, pp. 9028–9041, May 1989.

[147] D. Griscom, "The electronic structure of SiO_2: a review of recent spectroscopic and theoretical advances," Journal of Non-Crystalline Solids, vol. 24, no. 2, pp. 155–234, 1977.

[148] R. Devine and J. Arndt, "Correlated defect creation and dose-dependent radiation sensitivity in amorphous SiO_2," Physical Review B, vol. 39, no. 8, p. 5132, 1989.

[149] L. Skuja, "Optically active oxygen-deficiency-related centers in amorphous silicon dioxide," Journal of NON-crystalline Solids, vol. 239, no. 1-3, pp. 16–48, 1998.

[150] Y. Borodko, J. W. Ager, G. E. Marti, H. Song, K. Niesz, and G. A. Somorjai, "Structure sensitivity of vibrational spectra of mesoporous silica SBA-15 and Pt/SBA-15," The Journal of Physical Chemistry B, vol. 109, no. 37, pp. 17386–17390, 2005.

[151] R. Baitahe, N. Vittayakorn, and S. Maensiri, "Correlation between the chromaticity, dielectric properties and structure of the binary metal pyrophosphates, $Cu_{(2-x)}Zn_xP_2O_7$," RSC Advances, vol. 5, no. 108, pp. 88890–88899, 2015.

[152] T. A. Bird, M. G. Wilkinson, D. A. Keen, R. I. Smith, N. C. Bristowe, M. T. Dove, A. E. Phillips, and M. S. Senn, "Soft-mode anisotropy in the negative thermal expansion material ReO_3," Physical Review B, vol. 104, no. 21, p. 214102, 2021.

[153] G. Ernst, C. Broholm, G. Kowach, and A. Ramirez, "Phonon density of states and negative thermal expansion in ZrW_2O_8," Nature, vol. 396, no. 6707, pp. 147–149, 1998.

[154] C. W. Li, X. Tang, J. A. Munoz, J. B. Keith, S. J. Tracy, D. L. Abernathy, and B. Fultz, "Structural relationship between negative thermal expansion and quartic anharmonicity of cubic ScF_3," Physical Review Letters, vol. 107, no. 19, p. 195504, 2011.

[155] S. Pastukh, P. T. Jochym, O. Pastukh, J. Łażewski, D. Legut, and P. Piekarz, "Anharmonicity and structural phase transition in the Mott insulator $Cu_2P_2O_7$," Physical Review B, vol. 108, no. 10, p. 104104, 2023.

[156] W. Cochran, "Crystal stability and the theory of ferroelectricity," Physical Review Letters, vol. 3, no. 9, p. 412, 1959.

[157] Ł. Laskowski, A. Majtyka-Piłat, K. Cpałka, M. Zubko, and M. Laskowska, "Synthesis in silica nanoreactor: Copper pyrophosphate quantum dots and silver oxide nanocrystallites inside silica mezochannels," Materials, vol. 13, no. 9, p. 2009, 2020.